Atmos. Meas. Tech., 7, 3509–3527, 2014
www.atmos-meas-tech.net/7/3509/2014/
doi:10.5194/amt-7-3509-2014

Atmospheric Measurement Techniques
Open Access

A simple and versatile cloud-screening method for MAX-DOAS retrievals

C. Gielen[1], M. Van Roozendael[1], F. Hendrick[1], G. Pinardi[1], T. Vlemmix[2], V. De Bock[3], H. De Backer[3], C. Fayt[1], C. Hermans[1], D. Gillotay[1], and P. Wang[4]

[1]Belgian Institute for Space Aeronomy (BIRA-IASB), Brussels, Belgium
[2]Department of Geosciences and Remote Sensing, Delft University of Technology, the Netherlands
[3]Royal Meteorological Institute of Belgium, Brussels, Belgium
[4]Institute of Atmospheric Physics, Chinese Academy of Sciences, Beijing, China

Correspondence to: C. Gielen (clio.gielen@aeronomie.be)

Received: 25 April 2014 – Published in Atmos. Meas. Tech. Discuss.: 12 June 2014
Revised: 29 August 2014 – Accepted: 10 September 2014 – Published: 13 October 2014

Abstract. We present a cloud-screening method based on differential optical absorption spectroscopy (DOAS) measurements, more specifically using intensity measurements and O_4 differential slant-column densities (DSCDs). Using the colour index (CI), i.e. the ratio of the radiance at two wavelengths, we define different sky conditions including clear, thin clouds/polluted, fully-cloudy, and heavily polluted. We also flag the presence of broken and scattered clouds. The O_4 absorption is a good tracer for cloud-induced light-path changes and is used to detect clouds and discriminate between instances of high aerosol optical depth (AOD) and high cloud optical depth (COD).

We apply our cloud screening to MAX-DOAS (multi-axis DOAS) retrievals at three different sites with different typical meteorological conditions, more specifically suburban Beijing (39.75° N, 116.96° E), Brussels (50.78° N, 4.35° E) and Jungfraujoch (46.55° N, 7.98° E). We find that our cloud screening performs well characterizing the different sky conditions. The flags based on the colour index are able to detect changes in visibility due to aerosols and/or (scattered) clouds. The O_4-based multiple-scattering flag is able to detect optically thick clouds, and is needed to correctly identify clouds for sites with extreme aerosol pollution. Removing data taken under cloudy conditions results in a better agreement, in both correlation and slope, between the MAX-DOAS AOD retrievals and measurements from other co-located instruments.

1 Introduction

In recent years, ground-based multi-axis differential absorption spectroscopy (MAX-DOAS) has been demonstrated to be ideally suited for the retrieval of tropospheric trace gases and deriving information on aerosol properties (e.g. Hönninger et al., 2004; Wagner et al., 2004; Frieß et al., 2006; Clémer et al., 2010; Hendrick et al., 2014). These measurements are invaluable to our understanding of the physics and chemistry of the atmospheric system, and the impact on the Earth's climate.

MAX-DOAS retrievals of trace-gas columns and aerosol optical depths typically assume clear-sky conditions in the forward model. However, MAX-DOAS measurements are often strongly affected by clouds, leading to significant data quality degradation and larger uncertainties on the retrievals. This, in turn, strongly impairs the use of ground-based retrievals in the context of satellite validation.

In this paper we present a cloud-screening method, based on (MAX-)DOAS measurements, which aims at providing a general qualification of the sky and cloud conditions during the measurements. The data set consists of multi-year observations made at three sites with very different typical meteorological conditions, Xianghe (suburban Beijing, 39.75° N, 116.96° E), Brussels (50.78° N, 4.35° E) and the alpine station of Jungfraujoch (46.55° N, 7.98° E). We focus on 90° elevation observations for the colour index as our simulations show these are the most sensitive to the sky conditions (see Sect. 3). Moreover, they are independent of the azimuth angle, and are very sensitive to the temporal variability of

clouds above the instrument site. The use of the zenith measurements means that the cloud-screening method is not only limited to MAX-DOAS but can also be applied to similar instruments working in the zenith mode only. For the O_4 measurements we also use the 30–90° elevation measurements, but the method can also be applied if only zenith measurements are available (see Sect. 4.3).

The recent paper of Wagner et al. (2013) described in detail the effect of clouds on the different quantities derived from MAX-DOAS observations, such as the radiance, colour index, O_4 absorption and the Ring effect (the filling-in of Fraunhofer lines due to inelastic scattering on atmospheric molecules). They developed a cloud-screening method based on these effects and on the comparison with clear-sky reference simulations. The method was applied to observations made during the CINDI campaign (Piters et al., 2012), where a good agreement with sky images taken from the ground was found. However, the total data set used contained data of only a limited time span (12 June 2009–15 July 2009).

Our cloud-screening method is similar to the method described in Wagner et al. (2013) but uses a simpler approach. Both methods use colour-index (CI) simulations and the temporal variability of the CI and O_4 absorption, but our method is not based on radiance or O_4 simulations and does not use information from the full MAX-DOAS elevation scan but focuses on the zenith elevation (and in lesser degree the 30° elevation). Our approach is furthermore based on a general simulation model of the colour index, which is used for all different measurement sites, thereby strongly reducing the computational cost and enhancing the general applicability of the method.

This paper shows that a simple cloud-screening method can be successfully applied to large data sets measured under a wide variety of meteorological conditions, from the extreme polluted atmosphere above Xianghe, the cloud-dominated Brussels data set, to the pristine alpine skies in Jungfraujoch.

In Sect. 2 the different MAX-DOAS instruments and the DOAS data analysis are described. In Sect. 3 the concept of the colour index and its relationship with sky and cloud conditions are presented. A description of our cloud-screening method and the definition of the cloud-screening flags can be found in Sect. 4. In Sect. 5 the results from the cloud screening at Brussels with co-located thermal infrared cloud-cover measurements are compared. Next, we apply our cloud-screening to aerosol model retrievals. A description of the radiative transfer model and co-located aerosol measurements and the resulting effect of the cloud screening on the agreement between model and measurements can be found in Sect. 6. We end with the conclusions in Sect. 7.

2 MAX-DOAS measurements

The MAX-DOAS instrument is a passive DOAS instrument that performs quasi-simultaneous measurements of scattered sunlight for a range of different elevations, from the horizon to the zenith (Hönninger et al., 2004; Platt and Stutz, 2008). This results in an enhanced sensitivity to absorbing species in the lower troposphere compared to zenith observing techniques.

2.1 Instrument and site description

This study focuses on MAX-DOAS measurements at three different sites with very different typical meteorological conditions, namely Brussels, Jungfraujoch and Xianghe (suburban Beijing). Xianghe is characterized by a polluted atmosphere, with episodes of extreme aerosol conditions which lead to a very low visibility. The sky over Brussels on the other hand only suffers from mild pollution, but is strongly affected by the presence of clouds. The alpine station of Jungfraujoch experiences almost no aerosol pollution but can suffer from cloudy and snowy conditions.

The instrument in Xianghe (39.75° N, 116.96° E) is located about 60 km east of Beijing and points towards the north azimuthal direction, with a 0.8° field of view. For Xianghe a full MAX-DOAS scan is comprised of nine different elevations angles (2, 4, 6, 8, 10, 12, 15, 30, and 90°) and takes about 15 minutes of measurement time. This instrument has been discussed in detail in Clémer et al. (2010); Hendrick et al. (2014). It is a dual-channel instrument composed of two grating spectrometers, covering the UV (300–390 nm) and visible (400–720 nm) wavelength regions. The Xianghe MAX-DOAS instrument has been designed and assembled at the Belgian Institute for Space Aeronomy (BIRA-IASB) in Brussels, and has been continuously running since 2010.

The mini-MAX-DOAS instrument in Brussels (50.78° N, 4.35° E), has a shorter wavelength range, limited to 290–435 nm, again pointing north, with a 0.6° field of view. A full scan goes over 11 elevation angles (2, 3, 4, 5, 6, 8, 10, 12, 15, 30, and 90°) and requires approximately 15 minutes. It is a commercial system from Hoffmann Messtechnik GmbH and has been continuously running since 2011. A more detailed description of the instrument can be found in Ma et al. (2013).

The alpine station of Jungfraujoch (46.55° N, 7.98° E) is located in the Swiss Alps, with a pointing azimuth of 145 °, at an altitude of 3570 m. A dual-channel UV (300–390 nm) and VIS (400–560 nm) MAX-DOAS instrument has been installed by BIRA-IASB and operational there since 2010. The configuration of the instrument is similar to the one in Xianghe, but it can also reach negative elevation angles pointing down in the valley (−10, −8, −6, −4, −2, and 0°). However, we do not use these negative elevation angles in this work.

2.2 DOAS data analysis

The first step of the retrieval consists of analysing the MAX-DOAS spectra by making use of the DOAS method (Platt and Stutz, 2008). This method is developed to separate narrow-band differential absorption patterns (which can be related to specific molecules in the atmosphere) from broad-band extinction caused by Rayleigh and Mie scattering due to scattering on molecules and particles. The direct products of this technique are differential slant column densities (DSCDs), i.e. the integrated concentration of absorbing molecular species along the effective light path relative to the integrated concentration along the average light path of a reference spectrum. To analyse the MAX-DOAS spectra the spectral-fitting software package QDOAS is used (http://uv-vis.aeronomie.be/software/QDOAS/).

Information on aerosol characteristics, i.e. AOD and extinction profile, is obtained using O_4 DSCDs (see Sect. 6.1). This is possible since the vertical distribution of O_4 is well known and nearly constant, as it varies with the square of the O_2 monomer. Deviations of the O_4 DSCD from values representative for a clear sky are often caused by aerosols or clouds. Measurements of the O_4 DSCD can therefore be used for the retrieval of aerosols (Hönninger et al., 2004; Wagner et al., 2004; Frieß et al., 2006). These DSCDs are retrieved in the UV (338–370 nm) for Brussels, Jungfraujoch and Xianghe, and in the VIS for Xianghe and Jungfraujoch (425–490 nm), using the O_4 cross-sections from Hermans et al. (2003). These wavelength ranges are the most sensitive to O_4 absorption (Roscoe et al., 2010), and have minimal interference from other absorbing species. Other trace gases used for the fitting include NO_2, O_3, H_2O, HCHO and BrO, along with a Ring spectrum. For the observed broad-band extinction a fifth-order polynomial is used. A detailed description of the QDOAS setting for aerosol retrievals can be found in Clémer et al. (2010).

3 The colour index

To characterize the sky conditions at the different measurement sites we develop a cloud-screening method based on two different measured quantities: the colour index (CI) of the sky and the O_4 DSCDs. The CI is defined as the ratio of the intensity of a measured spectrum at two wavelengths, and gives information on the observed colour of the sky. Since, during the daytime, the sky colour changes from blue during clear skies to white/gray when clouds or aerosols are present, we can use the CI to qualify the sky condition. This becomes increasingly difficult for high SZA values, as the sky colour varies, even for clear skies.

The CI for Xianghe, Brussels, and Jungfraujoch are defined as I_{405}/I_{670}, I_{347}/I_{420} , and I_{405}/I_{550} respectively, with I_x the median intensity over the $[x-5\,\text{nm}, x+5\,\text{nm}]$ wavelength range, to reduce the effect of spectral noise on the derived intensity values. The wavelength regions were chosen to obtain the largest spectral contrast, i.e. they span the largest wavelength range possible for the respective instrument, and avoid the influence of strong atmospheric spectral features.

As can be seen for Xianghe in Fig. 1, the CI shows a clear pattern depending on the observed meteorological conditions. For clear skies the CI values are high, due to the wavelength dependence of Rayleigh scattering, and they decrease with increasing aerosol load (Fig. 1:day 35) since scattering on aerosol and cloud particles is less wavelength dependent. We also see a clear separation between the different elevation angles of the observations. The highest CI values can be found for spectra with the highest elevation angles, whereas low elevation angles show lower values and spread. In the case of an extreme aerosol load or full cloud cover, the CI values are all clustered around a constant value (Fig. 1: days 114–115). In the case of broken or scattered clouds, the CI shows a very variable temporal behaviour (Fig. 1: day 256).

Simulations of the CI corroborate the observed decrease of the CI in the presence of clouds and aerosols, as can be seen in Fig. 2. These simulations were made with the DAK (doubling-adding KNMI code) radiative transfer model (Stammes et al., 1989; Stammes, 2001, http://www.knmi.nl/~stammes/DAK/Manual_DAKver312.pdf) under varying aerosol and cloud optical depths, and varying parameters such as wavelength, elevation, SZA and azimuth angle. For the aerosols a homogeneous layer up to 1 km with a single scattering albedo of 0.9 and asymmetry parameter of 0.7 was used, for the clouds these values are respectively 1.0 and 0.85. The cloud base height was set at 1 km, with a total thickness of 1 km, a surface albedo of 0.05 was used, and atmospheric Rayleigh scattering and ozone absorption were included. We also tested the effect of varying the cloud base height, ranging from 1 km to 8 km, but found very little influence on the derived CI values, especially for higher elevation angles.

These simulations show that it is very difficult to distinguish between aerosols and clouds using only CI information. For this reason also information from the observed O_4 DSCDs will be used, which will be discussed in a later section (Sect. 4.3).

Fig. 3, which presents simulations of the CI for the three different wavelength ratios used for the different measurement sites, shows that the CI derived from spectra with low elevation angles have a much narrower spread regarding different aerosol settings, making it difficult to distinguish between the different parameters. These simulations furthermore show that the same problem of overlapping simulations occurs for observations taken at SZA$> 85°$. For this reason we exclude these data from our study. The simulations at 90° elevation show a narrower spread for lower SZA values ($\lesssim 40°$), compared to the 15° and 30° elevation angle. However, at larger SZA ($\gtrsim 55°$) the situation is reversed.

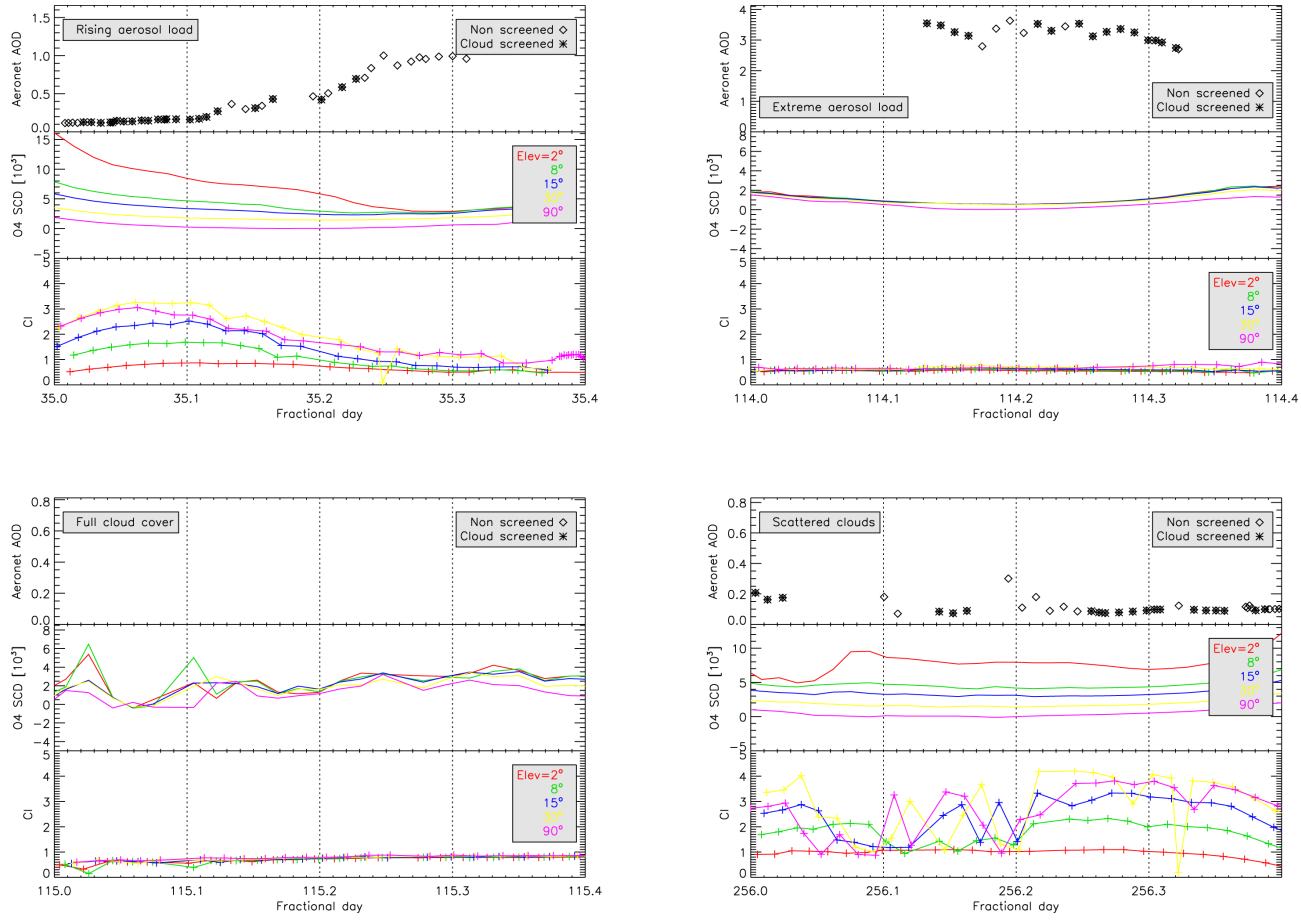

Figure 1. Comparison of 4 days at Xianghe with distinct meteorological conditions. The top box shows the measured AERONET AOD at 477 nm, both the non-screened (level 10) and cloud-screened (level 15) data, the middle box the measured MAX-DOAS O_4 DSCDS (in units of 10^{40} molec^2 cm^{-5}) and the bottom box the calculated colour index. Different colours represent the different MAX-DOAS elevation angles. Fractional day is always given in UT time.

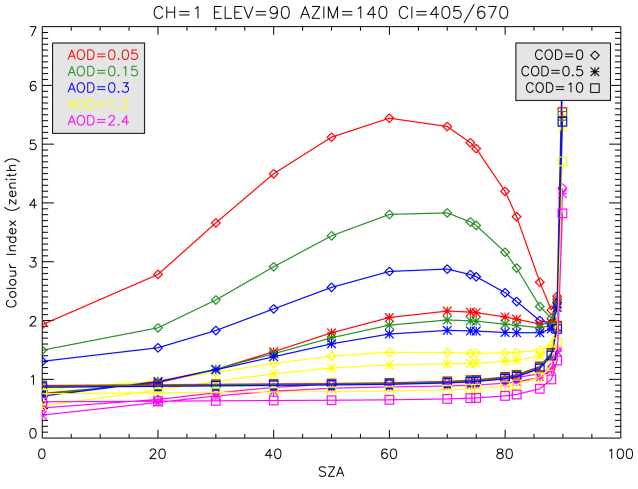

Figure 2. Simulations of the colour index (I_{405}/I_{670}) under varying aerosol optical depth (AOD) and cloud optical depth (COD). The simulations were performed with the DAK plan-parallel radiative transfer model (Stammes, 2001), using a cloud-layer height of 1 km.

The same result is found for simulations made under different cloud optical depth settings.

As we only have little observations made at low SZA (< 40°), we therefore choose the 90° as the best elevation for our further study. In principle, the method can be extended in a similar way to include CI (and O_4 DSCD) information from multiple elevation angles, with the realization that the higher elevation angles will give the best constraints. This is discussed briefly in Sect. 6.1. We restrict ourselves to only one elevation angle for the sake of simplicity and to show that the method already works well with this restriction. The zenith elevation further has the advantage of not depending on the viewing azimuth of the instrument, which simplifies the computational effort for the CI simulations if data sets from instrument with different pointing direction are used.

The resulting calculated zenith CI values for the full Xianghe, Brussels and Jungfraujoch data sets can be found in Fig. 4. All sites show a frequency distribution with a clear peak at the lowest CI values, corresponding to observations taken under non-clear-sky conditions. For Jungfraujoch we

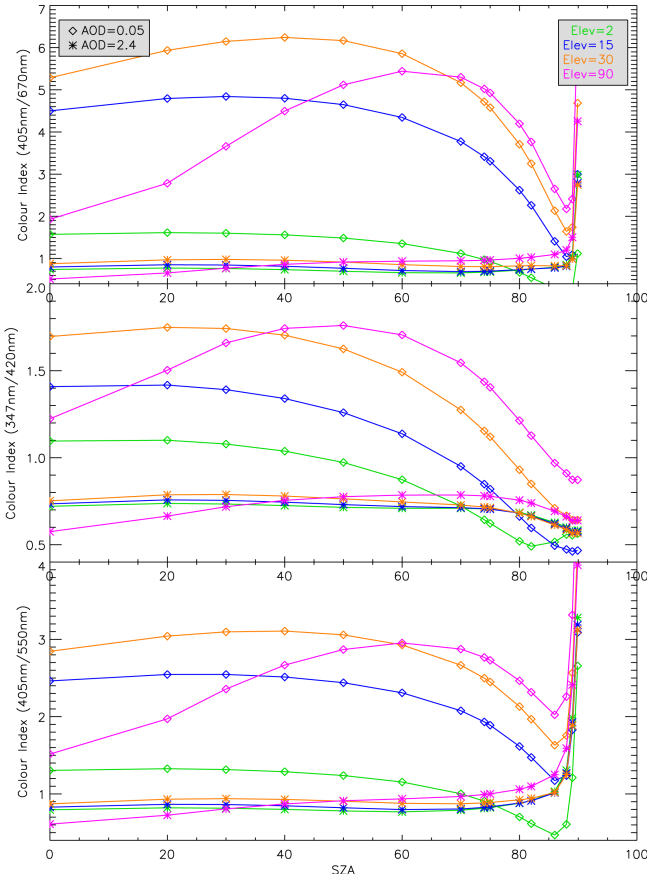

Figure 3. Simulations of the colour index under varying AOD and using the wavelengths corresponding to the three different measurement sites, respectively Xianghe, Brussels and Jungfraujoch from top to bottom. The simulations were performed with the DAK plan-parallel radiative transfer model (Stammes, 2001), using a cloud-layer height of 1 km and a cloud optical depth of 0.

see a more bimodal distribution, where the small peak at higher CI values corresponds to a larger frequency of clear days, compared to the other sites. The differences in the observed CI values between the different sites are due to the different wavelength ranges used for the CI calculation and the differences in instrumental response.

It is important to investigate the behaviour of the CI over time to spot variations in the CI which are due to instrumental issues, such as a shift in instrumental response after technical difficulties, changes in set-up, or instrument degradation. If clear CI variations are spotted that can be linked to instrumental issues, it is important to correct for this.

An example of this can be seen in Fig. 5: an instrumental failure at Brussels on the 20th of May resulted in a strong downward shift of the CI values. We corrected for this by shifting the CI values after the failure in such a way that the peak values of the histograms of CI values before and after the incident coincide. It is clear that sufficient data need to be present to make an accurate correction.

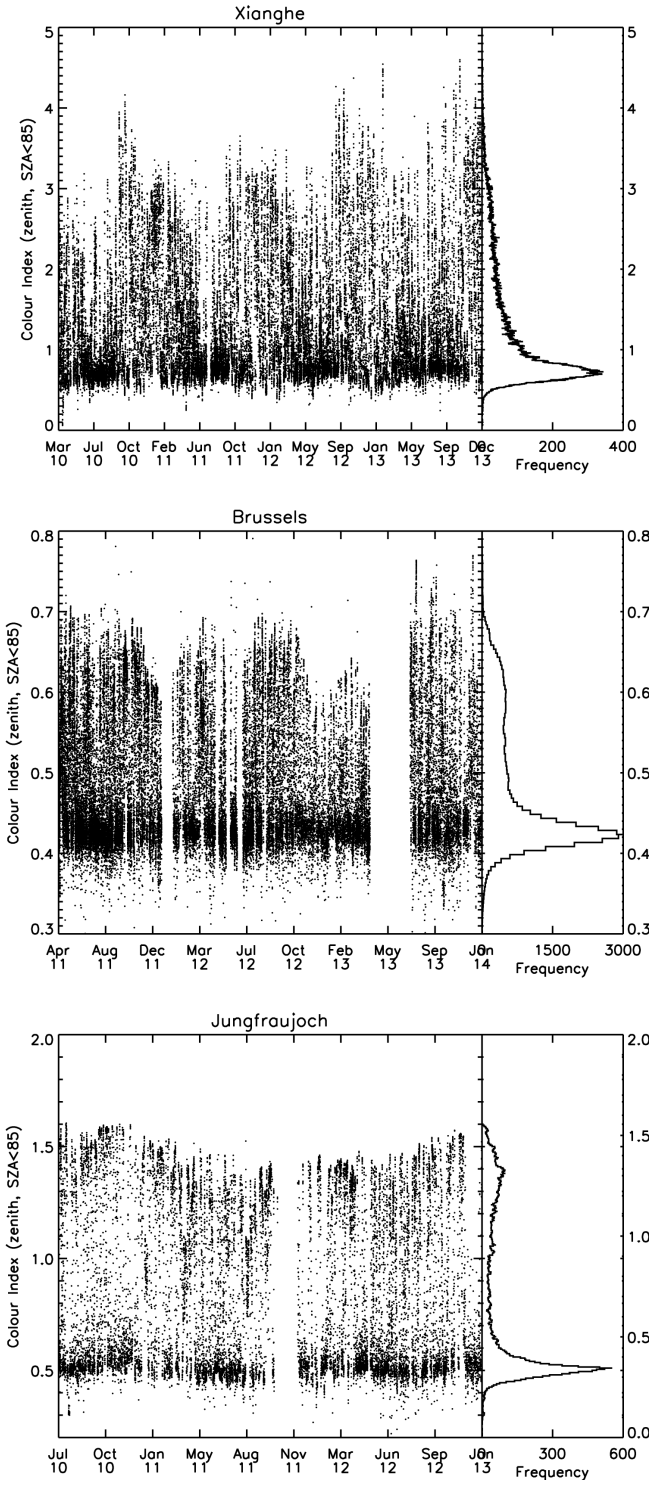

Figure 4. The calculated zenith CI values and frequency distribution for the full Xianghe, Brussels, and Jungfraujoch data sets.

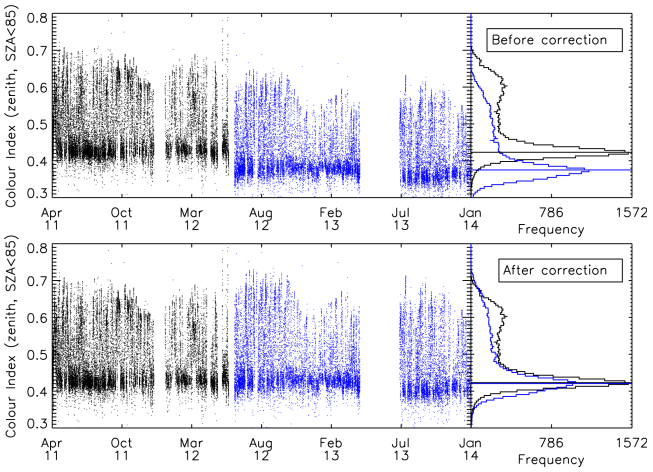

Figure 5. Illustration of the CI correction for Brussels due to an instrumental failure on May 20th 2012. The top panel shows the CI values and histograms before and after the incident in black and blue respectively. The bottom panel shows the corrected CI values. This was done by shifting the blue points in such a way that both histograms have the same peak value.

4 The cloud-screening method

To characterize the sky conditions we define three different flags: the sky flag, the broken-cloud flag, and the multiple-scattering flag. The sky flag defines the general sky conditions in terms of visibility – i.e. clear, mediocre, and bad. This flag does not distinguish between a visibility reduction due to clouds or aerosols. The broken-cloud flag denotes the presence of broken or scattered clouds. The third flag, which is based on the O_4 DSCDs and not the CI, marks the presence of enhanced multiple scattering in the line-of-sight, which we attribute to the presence of thick clouds.

4.1 The sky flag

For the sky flag we define three regions of CI values which are linked to general sky conditions in terms of visibility – i.e. clear, mediocre, and bad. To do this the calculated CI values are normalized between 0 and 1, to remove as much as possible of the wavelength and instrumental effects on the CI between the different measurement sites. This can only be done if enough data are available to have observations during both very clear and low-visibility sky conditions, which allows the determination of the minimum and maximum CI values.

To constrain the three regions, the full set of normalized CI values is compared with a grid of pre-calculated CI simulations, which we scale to give the best match with the observed spread in CI. For this the plane-parallel DAK simulations described in Sect. 3 are used, which are calculated for a range of different wavelengths, corresponding to the ones used for the CI calculation at the different sites. We do not fine-tune other model parameters such as surface albedo to the different site characteristics to minimize the computational effort. The simulations are scaled in such a way that the peak of the normalized CI frequency distribution corresponds to the clustering of simulations with high aerosol and/or cloud optical depth (AOD/COD), and so that the simulation with the lowest simulated aerosol optical depth (AOD = 0.05) follows the top of the normalized measured CI values. Additional AOD information from co-located instruments, such as a Cimel sun photometer (Holben et al., 2001), Brewer spectrophotometer (Cheymol and de Backer, 2003; De Bock et al., 2010) or solar irradiance instruments (Nyeki et al., 2012), is used to validate the procedure and make small adjustments in the scaling. As can be seen in Fig. 6, the distribution of scaled CI simulations corresponds well to the observed CI values and measured AOD values.

We then take the scaled simulation made with AOD = 0.15 and COD = 0.0 (green-diamond line in Fig. 6) as the limit to separate the "good" and "mediocre" region, as the simulation predicts that data above this curve were taken under cloud-free conditions with an extremely low aerosol load. This is further corroborated by comparison with co-located AOD measurements, as explained above. CI values above this curve are therefore flagged as made under "good" visibility conditions.

To separate between the "mediocre" and "bad" regions we define a horizontal line in such a way that the peak of the frequency distribution falls in the "bad" region. More specifically, we place the line at a distance of FWHM (full width at half maximum) from the peak position of the histogram. If x and y respectively denote the CI values and the frequency distribution, then the x position of the limit is $x_{\mathrm{bad}} = x(y_{\max}) + \mathrm{FWHM}(y)$. Note that this is of course only valid if the peak of measured CI values is associated with cloudy conditions. For sites with very clear skies and only little cloudy measurements a reverse approach could be taken. In this case a similar definition using the peak distribution could be used to define the "good" regime and the "bad" regime by comparing with simulations.

The resulting "good", "mediocre", and "bad" regions can be seen as, respectively, the green, orange and red regions in Fig. 7.

These regions correspond to different visibility conditions. Data flagged as "good" are taken under relatively clear conditions, i.e. very low aerosol and cloud optical depth. "Mediocre" data represents data under sky conditions with slightly decreased visibility, i.e. thin clouds and/or moderate aerosol pollution. Data with a "bad" flag points to the presence of thick clouds and/or extreme aerosol conditions.

4.2 The broken-cloud flag

To determine the presence of broken (semi-continuous cloud cover) or scattered clouds (predominantly clear sky) in the line-of-sight of measurement, the temporal variability of the

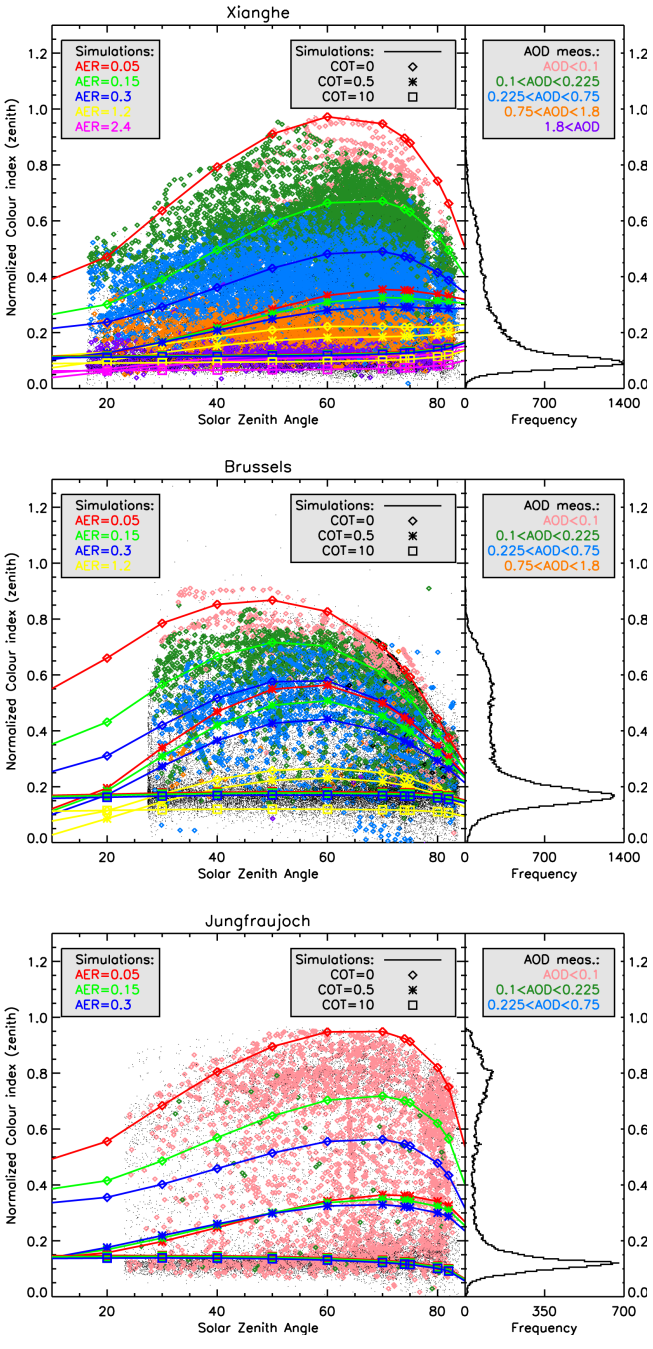

Figure 6. The normalized CI values (points) versus solar zenith angle, together with the scaled CI simulations (coloured lines) made under different aerosol and cloud optical depth values (left/middle legend). We colour-marked the observed CI values with additional AOD data if available (right legend).

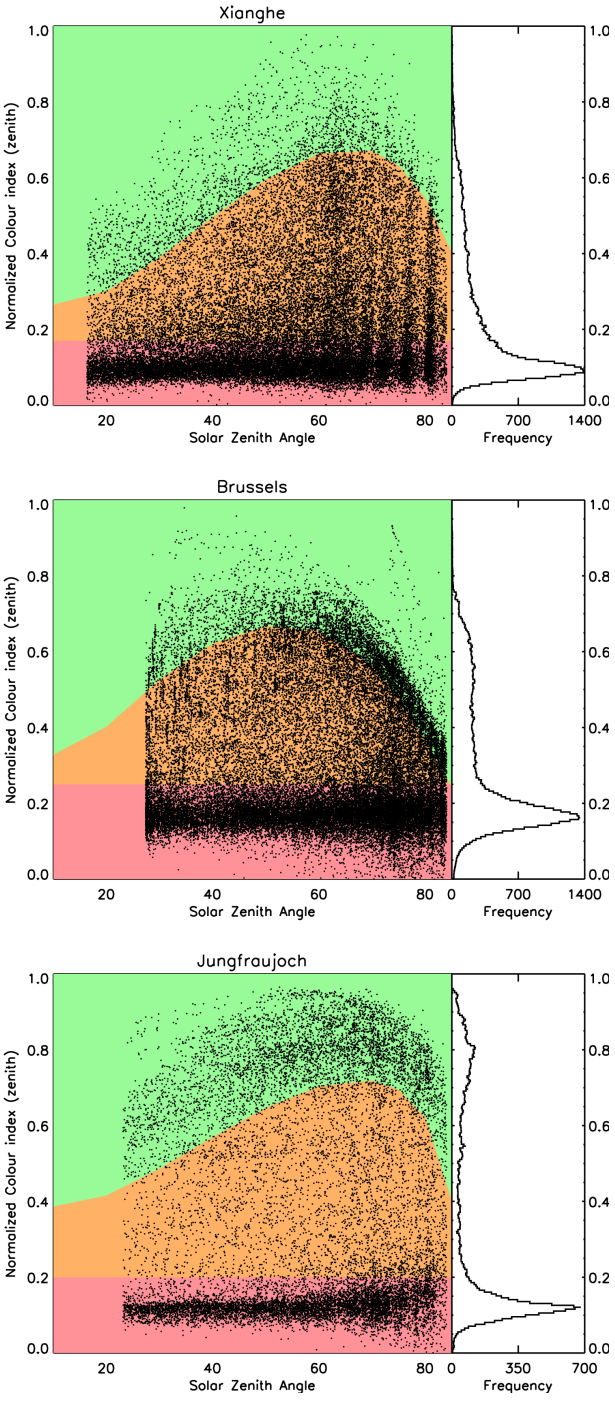

Figure 7. The normalized CI values (points) versus solar zenith angle. The green, orange and red regions correspond to the "good", "mediocre" and "bad" regions as defined by the sky flag.

CI is studied. As could already be seen in Fig. 1, the CI remains very stable for clear skies, skies with aerosol pollution, and skies with a full cloud cover, but in the presence of scattered clouds, the CI shows large drops in value when a cloud passes over.

To quantify this we model the observed CI values over time t for each day with a double-sine function of the form $f(t) = A + B\sin(Ct - D) + E\sin(Ft - G)$. Outliers are then identified as those data points with $|(CI(t) - f(t))/f(t)| > 0.1$. This value was derived by investigating those days with

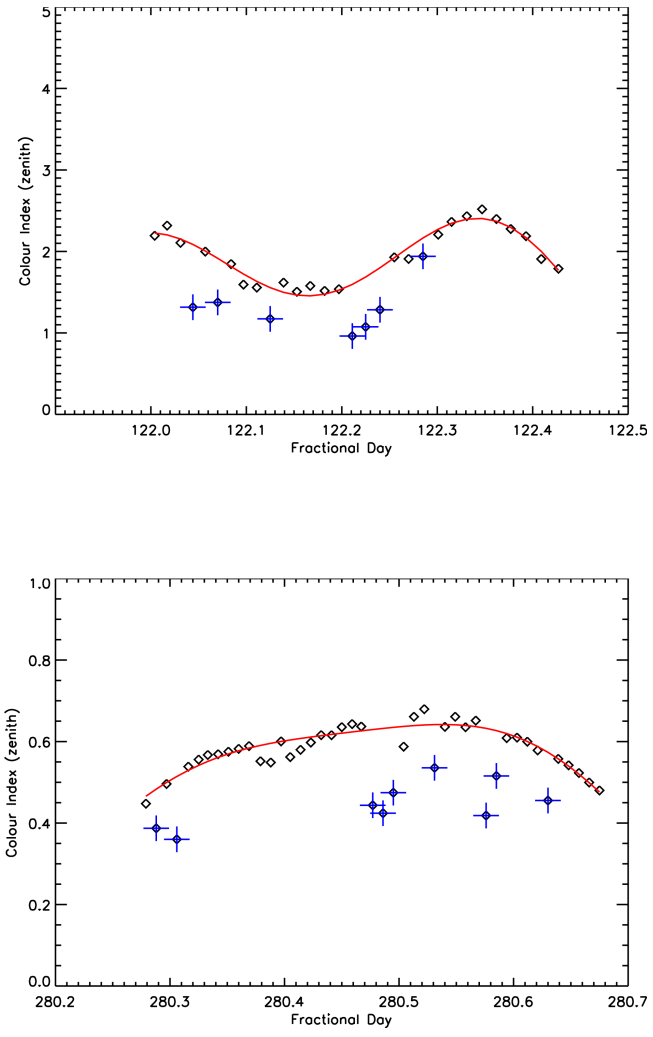

Figure 8. Results of the CI modelling (red line) to the measured CI values (black diamonds) and outlier detection (blue crosses) for the broken-cloud flagging, for example days in Xianghe and Brussels.

rapid temporal variability in the CI. For these days it was found that the observed jumps in CI predominantly fall above this cut-off value. These outliers are flagged as observations made under scattered/broken-cloud conditions. Examples of this modelling and outlier determination can be found in Fig. 8.

Note that this broken-cloud (BC) flag does not give any information about the presence of a full cloud cover, since this will not give rise to strong temporal variation in the CI values. The influence of aerosol variability on the temporal variation of the CI typically gives rise to a smoother increase or decrease, and will not give rise to the strong temporal jumps seen for cloud contamination.

4.3 The multiple-scattering flag

As discussed in the previous sections, the CI alone is not enough to distinguish between the presence of visibility reduction due to clouds or to aerosols. To partly resolve this problem we also define an additional constraint based on the measured O_4 DSCDs, which provide information on the effective light path of scattered photons. Clouds can have an increasing or decreasing effect on the O_4 DSCD value, with respect to clear-sky conditions. The first typically occurs for optically thick clouds, due to enhanced multiple scattering in the cloud layer. Optically thin clouds at high altitudes can also lead to an increase, but only for measurements under low elevation angles. Thin clouds at low altitudes tend to decrease the O_4 DSCDs at all elevation angles (Wagner et al., 2011). An increase in aerosol load will also affect the O_4 DSCDs, and will lead to a decrease in observed spread for the different elevation angles, as can clearly be seen in Fig. 1a.

Since both clouds and aerosols can thus have a very complex effect on the O_4 absorption, which can only be investigated in detail by comparing with radiative transfer models (as done in Wagner et al., 2013), we opt to only study the temporal variation of the measured O_4 DSCDs. Strong temporal variability due to enhanced multiple scattering commonly occurs in optically thick clouds, and is seen less for high aerosol optical depth, as illustrated by Fig. 1.

To study the temporal variability a similar procedure as for the detection of broken clouds is applied. Since we are not interested in slow and smooth changes in O_4 absorption, such as the observed diurnal trend, the DSCD measured at zenith is subtracted from the DSCDs at lower elevation angles α. This technique is commonly used in MAX-DOAS retrieval studies (e.g. Clémer et al., 2010; Hendrick et al., 2014), as it effectively removes the (negligible) stratospheric contribution to the O_4 absorption (Hönninger et al., 2004). Here, it has the advantage of removing the very strong diurnal trend, which hinders our modelling and outlier detection.

We then again model the resulting $O_4(\alpha\ -90°)$ DSCDs with a double-sine function $f(t)$ (see Fig. 9), and define an outlier as points with $|(O_4(t) - f(t))/f(t)| > 0.2$. We then make the assumption that these outliers are affected by multiple scattering due to clouds. This multiple-scattering (MS) flag can be defined for measurements at each elevation angle, but here we will focus further only on the 30–90° elevation scan, as the 30° elevation is closest to zenith and thus will encounter the lowest temporal cloud variation. In the case of zenith-pointing DOAS instruments, one could use only the zenith O_4 data, but then a model curve suited to fit the strong diurnal variation needs to be chosen.

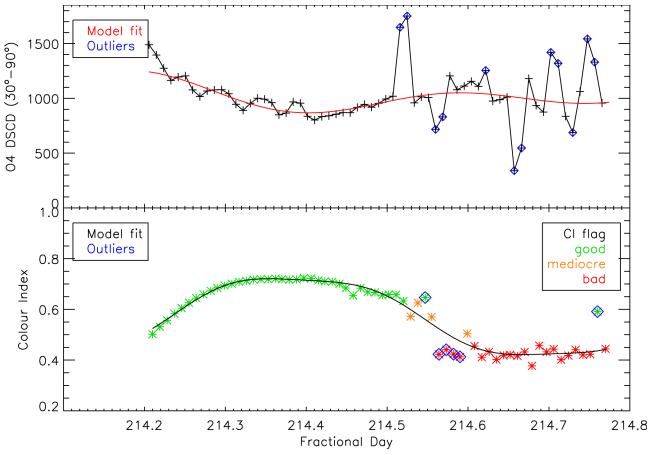

Figure 9. Top panel: results of the O_4 DSCD modelling (green line) to the measured O_4 values (black crosses) and outlier detection (blue diamonds) for the multiple-scattering flagging, for an example day in Brussels. For comparison we also show the results of the CI flagging (bottom panel). The CI values (asterisks) are coloured according to their CI flag. Outliers from the broken-cloud flagging are marked with a blue diamond.

4.4 Flag comparison

A good agreement is found between the O_4-based flag and information derived from the CI-based flags. Both types of flags can be used to mark cloudy data, i.e. data with enhanced multiple scattering on the one hand and data with a "bad" sky flag or broken-cloud flag on the other. Ideally, the same data points should be flagged as cloudy by both flag types. However, the multiple-scattering flag will be most sensitive to clouds with a high optical depth, whereas the colour index is also sensitive to clouds with a lower cloud optical depth, as even such clouds quickly change the observed sky colour.

For Brussels this indeed seems to be the case and a good agreement of 85 % is found; for Jungfraujoch, however, only about 60 % of points get marked as cloudy by both flag types.

The Xianghe data set shows the limitations of cloud screening using only the CI flags: when using the CI flags 20 % more data are marked as cloudy in comparison to the multiple-scattering O_4 flag. This is due to the fact that events of very high aerosol optical depth (AOD$>$ 2) are wrongly flagged as cloudy. For sites where such events occur regularly, the multiple-scattering flag seems to be a better choice to detect thick clouds. However, since the multiple-scattering flag requires a much larger computational effort compared to the CI flags and it adds little additional information for low or mild aerosol pollution, we opt not to use it for sites with low or moderate aerosol pollution. A comparison between the effect of the different flags on the measurements can be found in Sect. 6.

As MAX-DOAS measurements have the benefit of multiple viewing angles, one could extend the zenith-viewing method proposed here to other elevation angles. From our simulations it is clear that the highest elevation angles are best suited for this. Different viewing angles will mainly be sensitive to broken or scattered clouds, as the flagging in the case of clear or overcast days will give the same results for each elevation angle. Sites which experience a lot of broken clouds including CI flags from for example the 30° elevation angle will therefore be more likely to correctly identify the presence of clouds. We briefly discuss the effect on this on our retrievals in Sect. 6.

5 Comparison with infrared cloud-cover measurements

In order to validate the previously defined flags, the cloud-screening results for Brussels are compared with thermal infrared cloud-cover measurements. The Brussels site has access to an infrared pyrometer, which determines the total cloud-cover fraction based on temperature data over a field of view of 6° (Gillotay et al., 2001). The method works well to describe most cloudy conditions, with the exception of cirrus clouds with variable emissivity. The total cloud-cover fraction is defined as the ratio between the observed cloudy solid angle elements and clear-sky elements.

In Fig. 10 the total cloud-cover fraction values for an example day can be seen, where we colour-marked our different CI flagging results. High cloud-cover fractions are systematically flagged with a "bad" sky flag, whereas low cloud-cover data correspond to "good/mediocre" sky flags. These results are summarized in Fig. 11 where the distribution of cloud-cover values for the full Brussels data set ($\sim$ 2.5 years) is given, together with the distribution of points with corresponding sky flags. In the bottom plot the fraction of our sky flag results over the cloud-cover values are shown. Data with high cloud-cover fractions ($>$ 60 %) are generally flagged as "bad" by our cloud screening, whereas $\gtrsim$ 80 % points with a cloud-cover fraction $<$ 20 % are flagged as "good/mediocre with no broken clouds".

The same exercise was performed for the multiple-scattering flag, and we again find that data with high cloud-cover fractions are typically flagged as having a multiple scattering. This can again be seen in Fig. 11, where the blue line denotes the distribution of the MS flag over the cloud-cover percentages. We find that compared to the flags derived from the CI, more data with low cloud-cover values are flagged as having multiple scattering, i.e. being cloudy.

This shows that there is a good agreement between our cloud screening and the cloud-cover determination. One has to take into account that the field-of-view of the thermal infrared instrument is significantly larger than that of the MAX-DOAS, and thus that different areas of the sky are measured. Also, the value of our sky flag does not only depend on the presence of clouds, but also on the aerosol content. This means that cloud-free measurements can still be flagged as "mediocre" (or even "bad") if aerosols are present.

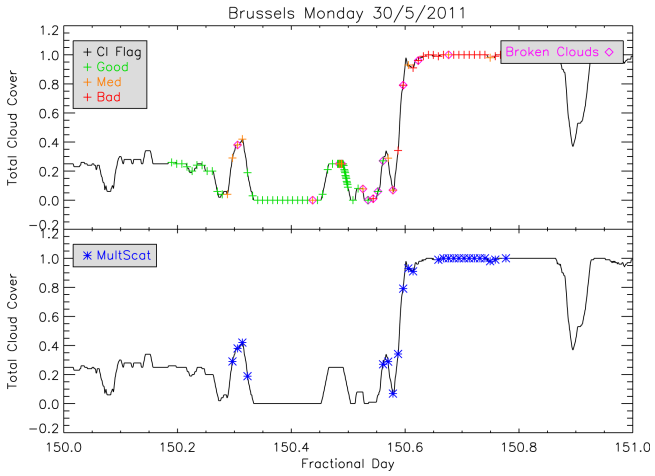

Figure 10. Total cloud-cover values from thermal infrared measurements are given in black points. Top: overplotted in coloured crosses are the respective CI-flag values as derived from our cloud-screening method (green/orange/red = good/med/bad). Data with a broken-cloud flag are marked with a magenta diamond. Bottom: in blue asterisks we plot data points with a multiple-scattering flag.

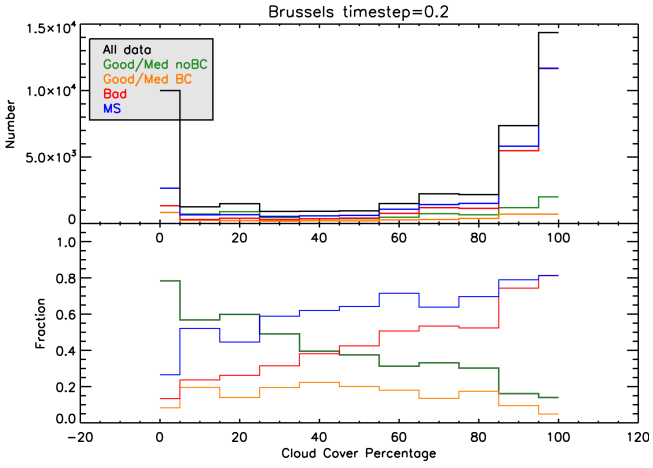

Figure 11. Top: distribution of the cloud-cover percentages for the full Brussels data set in black, with the division of data points with different sky flags. In red we plot data with a "bad" sky flag, in orange data with a "good/med" sky flag and a broken-cloud flag, and green denotes points with a "good/med" sky flag but no broken-cloud flag. In blue we mark data with a multiple-scattering flag. Bottom: fraction of total cloud-cover values as distributed over our different flag values.

6 Application to aerosol model retrievals

With the flags defined in the previous section we proceed to define a cloud-screening procedure for our MAX-DOAS retrievals. For this particular study we are interested in the aerosol load of the atmosphere, which means data too strongly affected by clouds need to be removed, but measurements made under polluted conditions should be retained.

For this reason we investigate data with a sky flag of either "good" or "mediocre", since a sky flag of "bad" is most commonly found for fully cloudy conditions. To remove data which are affected by scattered or broken clouds, we only keep data which are not flagged in the broken-cloud screening. This effectively removes all the cloud-contaminated data from our data sets. However, it also removes data under extreme aerosol conditions, as often found in Xianghe, as those measurements will also be flagged as "bad" in the sky-flag determination. To resolve this issue, we use the multiple-scattering flag to differentiate between measurements made under conditions with either high AOD or high COD.

6.1 AOD model retrievals and measurements

To study the effect of our cloud-screening method, AOD values retrieved by MAX-DOAS are compared to co-located AOD measurements. For Xianghe and Brussels we use AERONET Level 1.0 (unscreened) (and 1.5, cloud-screened) data, and for the Brussels site we extend the comparison with co-located Brewer spectrophotometer measurements at 320 nm (Brewer instruments #16 and #178). A detailed description of the co-located instruments and measurements can be found in Cheymol and de Backer (2003), De Bock et al. (2010) and Holben et al. (2001). At Jungfraujoch no AERONET instrument is available, so we used AOD values as measured by the Precision Filter Radiometer Network (Nyeki et al., 2012) in the context of the Global Atmosphere Watch – World Data Center for Aerosol (GAW-WDCA) programme of the World Meteorological Organization (WMO) (ebas.nilu.no).

For the MAX-DOAS aerosol retrievals the bePRO radiative transfer code (Clémer et al., 2010) is used, which is an inversion algorithm based on the optimal estimation method (Rodgers, 2000, OEM). The model uses the observed MAX-DOAS O_4 DSCDs to derive the vertical profiles of the aerosol extinction at different wavelengths. For Xianghe and Jungfraujoch, we focus on the 360 and 477 nm wavelengths, whereas for Brussels we only have access to the 360 nm wavelength due to the shorter instrumental range. A detailed description of the bePRO algorithm and parameters can be found in Clémer et al. (2010). It is found that the model is most sensitive to aerosols close to the surface, below 1 km, and typically contains about 1–2 pieces of independent information (DFS, degrees of freedom for signal). As discussed in Clémer et al. (2010) a correction factor of 0.8 was applied to the measured O_4 DSCDs for the Xianghe data set. This correction factor is needed to account for the observed offset between the simulated O_4 DSCDs and the measured values. For both the Brussels and Jungfraujoch data sets we did not find an improvement using the 0.8 correction factor, so we did not apply it here. At this point it is unclear what the origin is of this observed discrepancy between the measured and modelled O_4 DSCDs.

Only those results where the retrieved O_4 DSCDs have a percentage root mean square difference (RMSD) $< 50\,\%$ from the measured DSCDs are kept for the further study, since high RMSD values typically point to a failure of the model during the retrieval process. We define the RMSD as $\sqrt{\frac{\sum(\text{meas}-\text{retr})^2}{\sum \text{meas}^2}}$. For Jungfraujoch we use a more strict cut-off value of RMSD $< 30\,\%$ since we found that our modelling was less successful and stable for this data set.

6.2 Impact on aerosol retrievals

We perform the cloud screening by defining data as cloudy if: the sky flag is "bad" or it has a broken-cloud flag when using the CI-based flags, or it has a multiple-scattering flag when using the O_4-based flag. These constraints generally correctly flag the presence of thick clouds, but are less reliable when thin clouds are present, as the discrimination between thin clouds and low/mild aerosol pollution is not straightforward.

The results of our AOD retrievals and cloud screening can be found in Fig. 12 and the online supplementary material. In these figures the cloud-screened and co-located AOD measurements (black) and the cloud-screened bePRO retrievals are shown, colour-coded with the different flag values. A removal of data with evidence for the presence of clouds, be it either based on the sky and broken-cloud flag or the multiple-scattering flag, results in a much better agreement with the AOD measurements and retrievals. From Fig. 12 it is clear that "bad" data on average have higher AOD values. This is due to the fact that our bePRO model tries to model the observed optical depth increase caused by the clouds with aerosol optical depth, as clouds are not present in the model.

For the Xianghe data set it is also clear that a cloud screening based on the colour index alone, i.e. the sky and broken-cloud flag, often removes data under extreme aerosol conditions. When using the CI flags, about 60 % of data are removed, whereas the O_4-based flag only removes about 35 % of the data. Additional information from the O_4 DSCDs, i.e. the multiple-scattering flag, is needed to make sure we can differentiate between high AOD and high COD. This problem does not arise for Brussels and Jungfraujoch where a similar amount of data is flagged as cloudy by both methods, since here the AOD typically does not reach values above 1.5. It is also clear from Fig. 12 that a correct broken-cloud identification is much more important at the Brussels site, where clouds contaminate almost 70 % of the data. The Jungfraujoch data set clearly shows the low aerosol levels of the alpine site (AOD < 0.2), with significantly less cloudy conditions ($\sim 45\,\%$) compared to Brussels. An overview of the statistics of data removal by the cloud-screening method can be found in Table 1.

We also compared the distribution of AOD measurements and retrievals, as presented in Fig. 13. It can be seen that the cloud screening does not drastically change the observed shape and peak in the frequency distribution. For Xianghe we find a significant difference in shape between the 360 and 477 nm retrievals, with the former giving bePRO retrievals peaking at AOD $= 0.05$, whereas the latter peak around 0.2. The difference between our bePRO retrievals and co-located AERONET measurements is about 0.1, with a shift of the retrievals to the left for 360 nm, but to the right for the 477 nm data. This difference in AOD for different wavelengths was already found for a similar study of MAX-DOAS aerosol bePRO retrievals (Clémer et al., 2010) and could possibly be due to fitting difficulties during the DOAS retrievals, or uncertainties on the aerosol phase function used in the bePRO model. For Jungfraujoch we find very low AOD values, with a more double-peaked shape in the bePRO retrievals. For both wavelengths the retrievals peak at AOD $= 0.01$–0.02, but with a much narrower distribution at 477 nm. The co-located AOD measurements peak at AOD $= 0.005$ and 0.03 respectively for 360 and 477 nm. For the Brussels data set we again find that the cloud screening mostly removes data at higher AOD values, changing the observed right shoulder of the distribution. The bePRO retrievals and co-located measurements show a similar peak position, but the latter show a slightly broader distribution. A more detailed description of the bePRO modelling and retrieved aerosol properties for the different sites will be presented in an upcoming paper.

6.2.1 Correlation with co-located measurements

Correlation plots between our retrievals and co-located AOD measurements (AERONET/Brewer/solar irradiance spectra) can be found in Fig. 14. For the correlation study we averaged our retrievals in time steps of 0.2 h for Xianghe and Brussels. For Jungfraujoch the co-located measurements are hourly averages so we used the same 1 h time step. Averages were given a "bad" sky flag if $\geq 20\,\%$ of individual points had a "bad" sky flag, and a broken-cloud flag if $\geq 10\,\%$ of points had a broken-cloud flag. For the multiple-scattering flag we flagged the averages if more than one data point was flagged.

It should be noted that the AOD measurements (AERONET, Brewer, Cimel) themselves typically only operate when direct-sun observations can be made, which effectively removes a large part of data to use in the correlation study. For our correlation study we use non-cloud-screened co-located AOD measurements, a description of which can be found in Smirnov et al. (2000), Cheymol and de Backer (2003), De Bock et al. (2010) and Nyeki et al. (2012).

For Xianghe, about 46 % of points with coincident co-located measurements for the correlation study remain. For Brussels and Jungfraujoch this is around 20 %. This large removal of data is not only due to direct-sun restrictions but also long-time inoperativeness of the AERONET/Brewer instruments. Another note of caution is that the MAX-DOAS and other AOD-measuring instruments have different

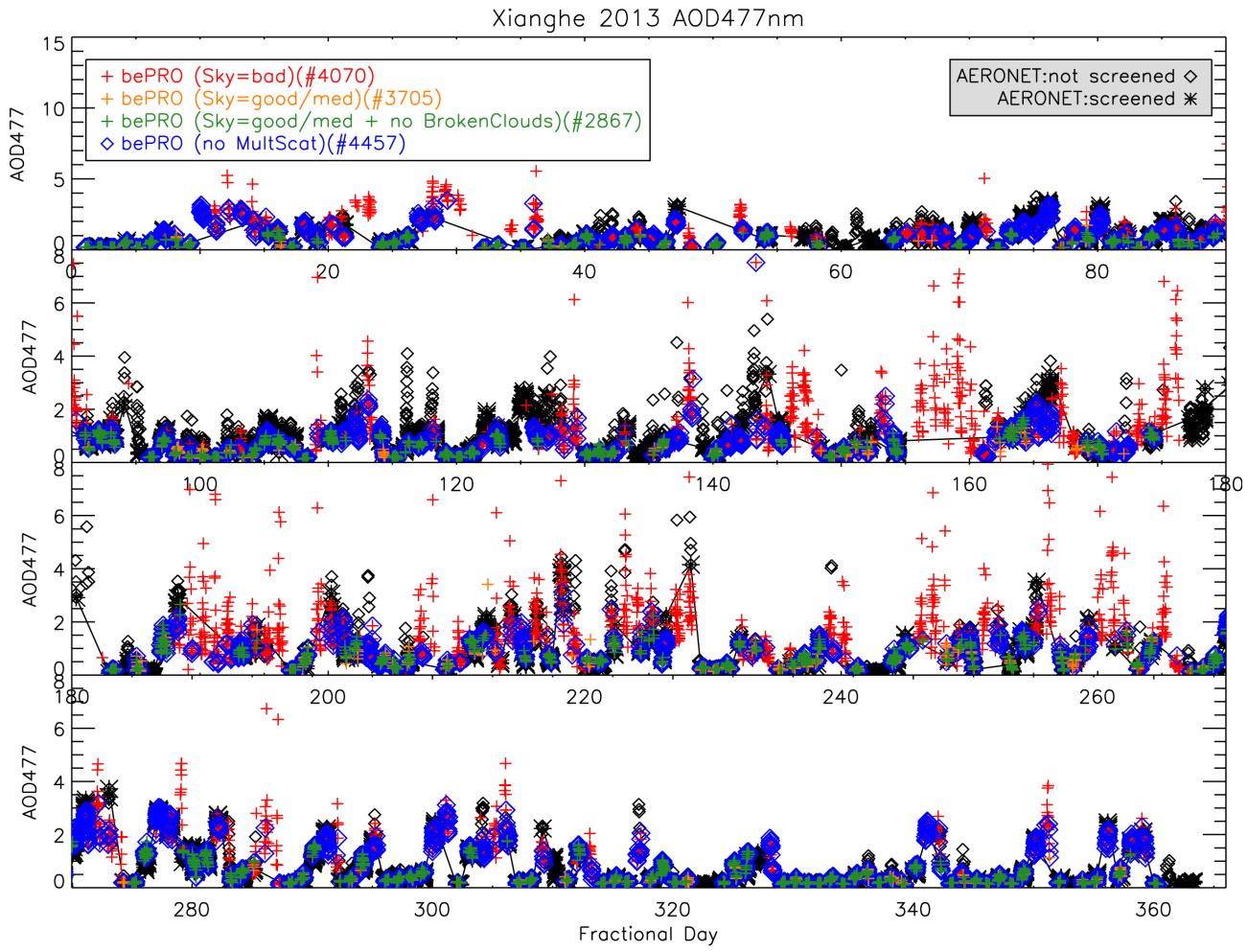

Figure 12. Example results of our bePRO AOD retrievals (crosses) compared to co-located AOD measurements (black diamonds/asterisks for non-screened/screened respectively). The different colours used for the retrievals denote the different cloud-screening results. Data with a "bad" sky flag are in red, data with a "good" or "mediocre" sky flag are in orange, data with a "good" or "mediocre" sky flag plus no broken-cloud flag are in green, and data with no multiple-scattering flag are in blue. More results can be found in the online supplementary material.

viewing directions, and might thus trace regions with slightly different cloud and aerosol characteristics.

We find a good agreement between our cloud flagging and the absence of AERONET/Brewer data. For Brussels $\sim 75\,\%$ of data without coincident measurements are flagged as cloudy, for Xianghe this number goes up to 80 % and for Jungfraujoch around 65 % of data with no co-located measurements are flagged as cloudy. A large percentage of the remaining data without co-located measurement but no cloud flag from our method can be attributed to instrumental inoperability.

The correlation plots in Fig. 14 show the linear regression results using only the CI information (green/orange crosses) and the results using only the O_4 DSCD multiple-scattering information (blue diamonds). As already mentioned above, without the multiple-scattering flag from O_4 absorption we remove non-cloudy data under extreme aerosol conditions, which is especially important for the Xianghe data set.

For the Xianghe data set we find high correlation coefficients R for the non-cloud-screened data.This is due to the fact that this site has only little influence from clouds, especially in comparison to Brussels, as can be seen in Figure 12. For both 360 and 477 nm we have a correlation value of $\sim R = 0.86$, and also the linear regression slopes S are very close to $S = 1$. For both wavelengths the cloud screening based on the CI (green crosses) slightly increases the correlation, with correlation values changing from $R = 0.86$ to $R = 0.89$. We see a difference between the two wavelengths: at 360 nm our model seems to overestimate the AOD in comparison to AERONET, whereas the opposite occurs at 477 nm. Applying the cloud screening improves the slope at 477 nm (from $S = 1.21$ tot $S = 0.91$), but worsens the slope at 360 nm (from 0.95 to $S = 0.78$).

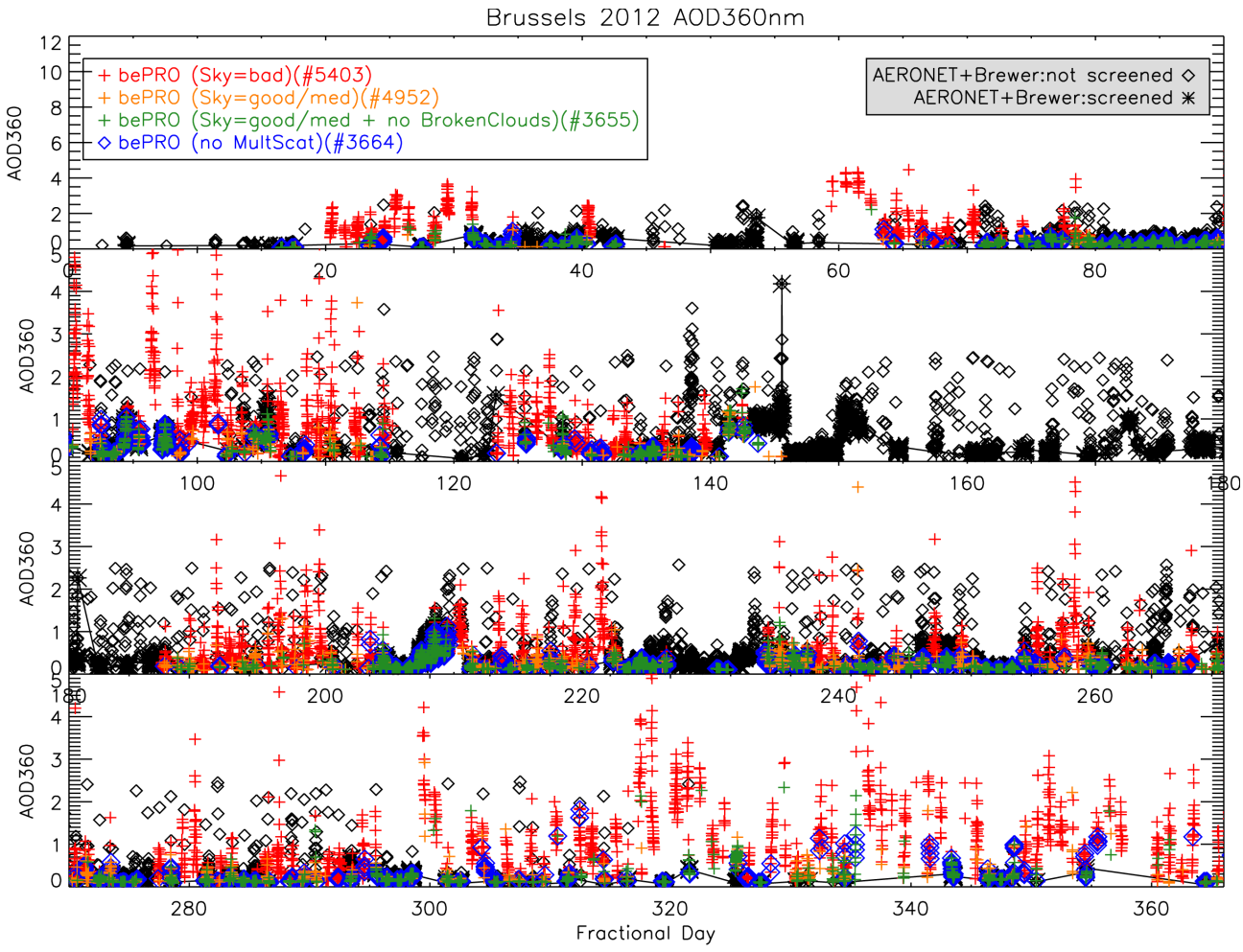

Figure 12. Continued.

For both wavelengths it can be seen that a cloud screening using the multiple-scattering flag improves the observed correlation slightly with ~ 0.01. It is clear that this method includes an area of high AOD values which were not covered using only the CI-based cloud screening, and that for sites that experience high AOD levels the CI (alone) is not enough for a correct cloud detection. Overall, the effect of our cloud screening on the Xianghe data is only minimal, which is mainly due to the fact that the site is not highly affected by clouds.

For Brussels we find much lower correlation values between our results and AERONET data. Without cloud screening, the correlation coefficient has a value of $R = 0.37$. When we remove data with a "bad" sky flag, the correlation coefficient increases to $R = 0.56$, and it increases even more when we also remove data contaminated by broken clouds, reaching a value of $R = 0.62$. Applying the cloud screening also changes the observed slope from $S = 0.60$ to $S = 0.83$ for the 0.2 h averaged time step. However, we find that even though the O_4-based cloud screening improves the correlation compared to the non-cloud-screened data, it does not give as good R values as the CI-based cloud screening.

When comparing the retrievals with the co-located Brewer measurements we do not expect to find an exact one-to-one correlation as the AOD values are determined at different wavelengths, respectively 320 nm and 360 nm for the Brewer and MAX-DOAS measurements. However, as we expect the AOD to have similar temporal behaviour at both wavelengths we can still study the observed correlation. We find a strong improvement in the observed correlation after applying our cloud screening, resulting in an increase from $R = 0.53$ to 0.7.

The extremely low AOD values for Jungfraujoch make it difficult to comment on the agreement between the modelled AOD values and co-located GAW-WDCA measurements, as most of the points are clustered around AOD = 0.02. Our bePRO retrievals in some cases strongly overestimate the AOD, which skews the observed correlation and slope to extreme values of $R = 0.0$–0.08 and $S = 0$. Applying the CI-based cloud screening only minimally improves the retrieved

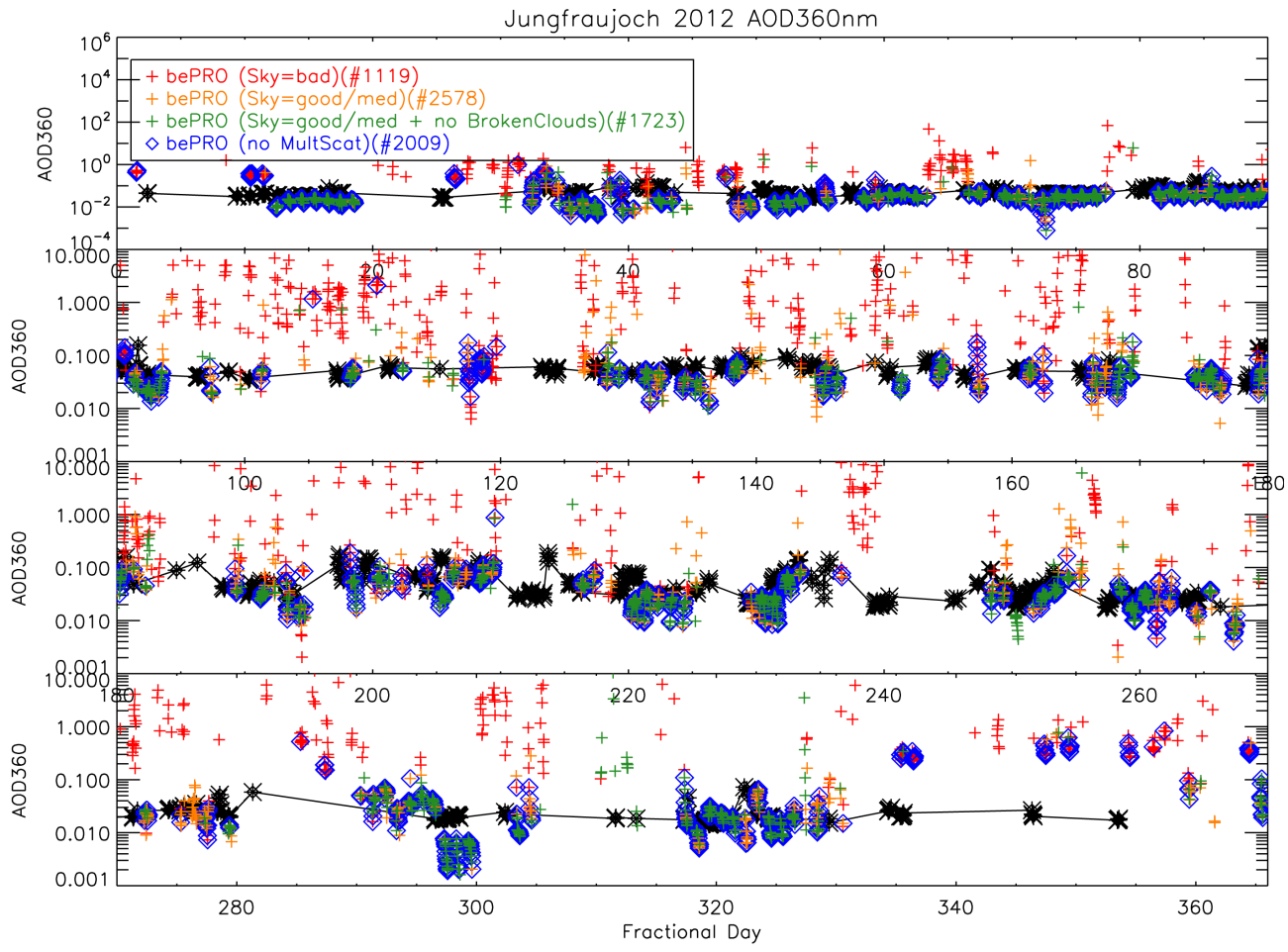

Figure 12. Continued.

Table 1. Overview of the number of retrieval points removed by the cloud-screening procedure. We give both the statistics for CI cloud screening based only on the zenith elevation angle (top) and cloud screening based on both the 30 and 90° elevation angles (bottom). The first column shows the respective site and wavelength, the second column gives the total number of points before cloud screening, the third column provides the percentage of data remaining after removing data with a "bad" CI flag, the fourth after removing data with a "bad" CI flag and a broken-cloud flag. The last column gives the percentage of data remaining after removal of data with a multiple-scattering flag.

Place + wavelength	Total number of data points	CI-flag = good/med	CI-flag = good/med + No broken clouds	No multiple scattering
90°				
Xianghe 360 nm	29740	46 %	36 %	63 %
Xianghe 477 nm	30780	46 %	37 %	63 %
Brussels 360 nm	29003	43 %	32 %	35 %
Jungfraujoch 360 nm	7693	72 %	51 %	55 %
Jungfraujoch 477 nm	7952	77 %	54 %	58 %
30 and 90°				
Xianghe 360 nm	29740	39 %	26 %	63 %
Xianghe 477 nm	30780	39 %	26 %	63 %
Brussels 360 nm	29003	28 %	21 %	34 %
Jungfraujoch 360 nm	7693	61 %	34 %	55 %
Jungfraujoch 477 nm	7952	66 %	37 %	58 %

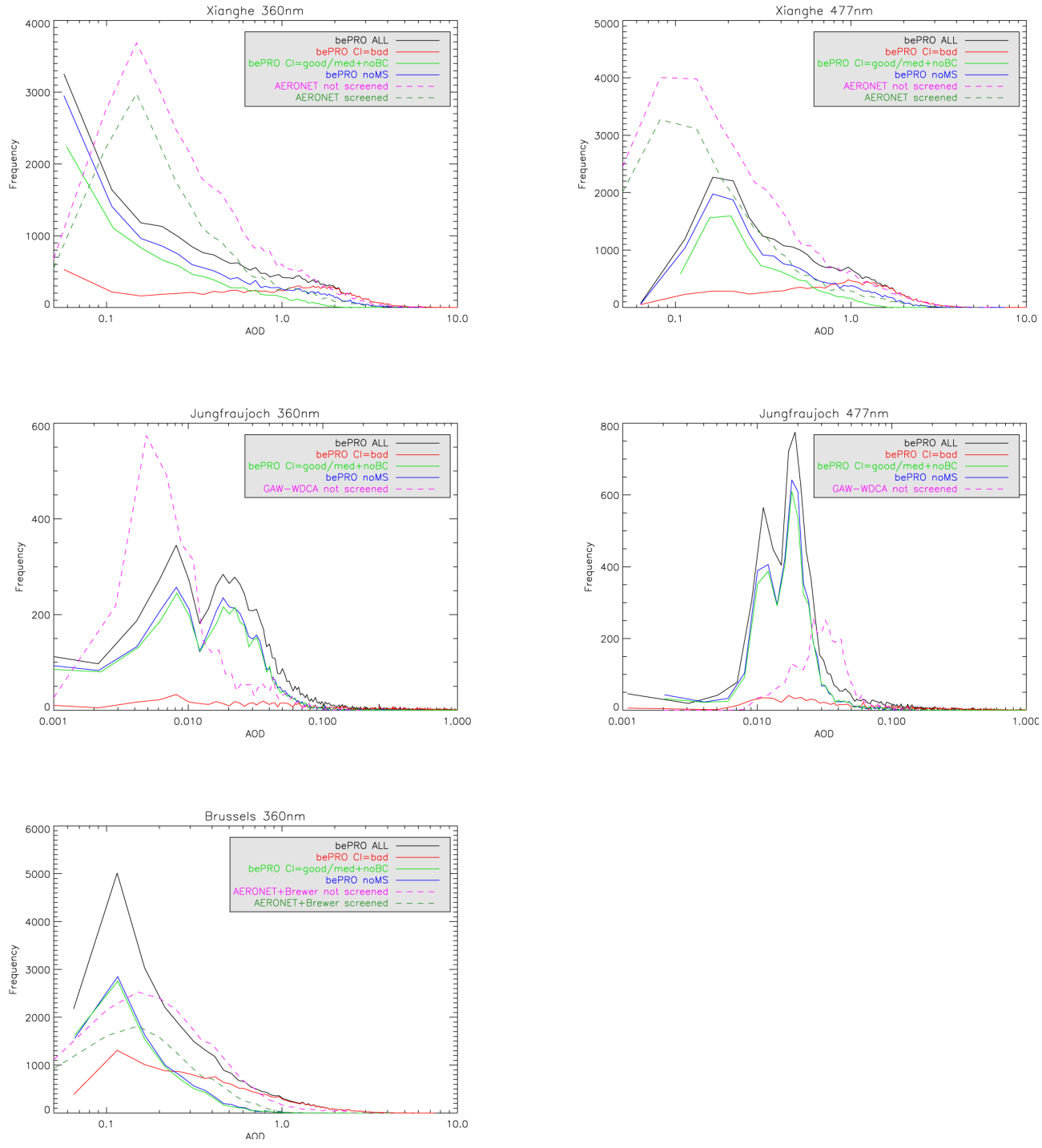

Figure 13. Histograms of our bePRO AOD retrievals and co-located AOD measurements for the three data sets. The bePRO retrievals are plotted in full lines, with black, red, green and blue respectively the unscreened data, data with "bad" CI flag, "good" CI flag and no broken-cloud flag, and no multiple-scattering flag. The co-located measurements are plotted in dashed lines, with magenta being the unscreened data and dark green the cloud-screened data.

correlation to $R = 0.15$. We find that the O_4-based cloud screening removes a similar amount of data points but does not drastically improves the correlation or slope. However, it is clear that the intrinsic uncertainties of the bePRO retrievals are too big in the case of very low AOD values to make strong conclusions on the observed correlations.

In the supplementary material we also show the correlation between our AOD retrievals and co-located measurements,

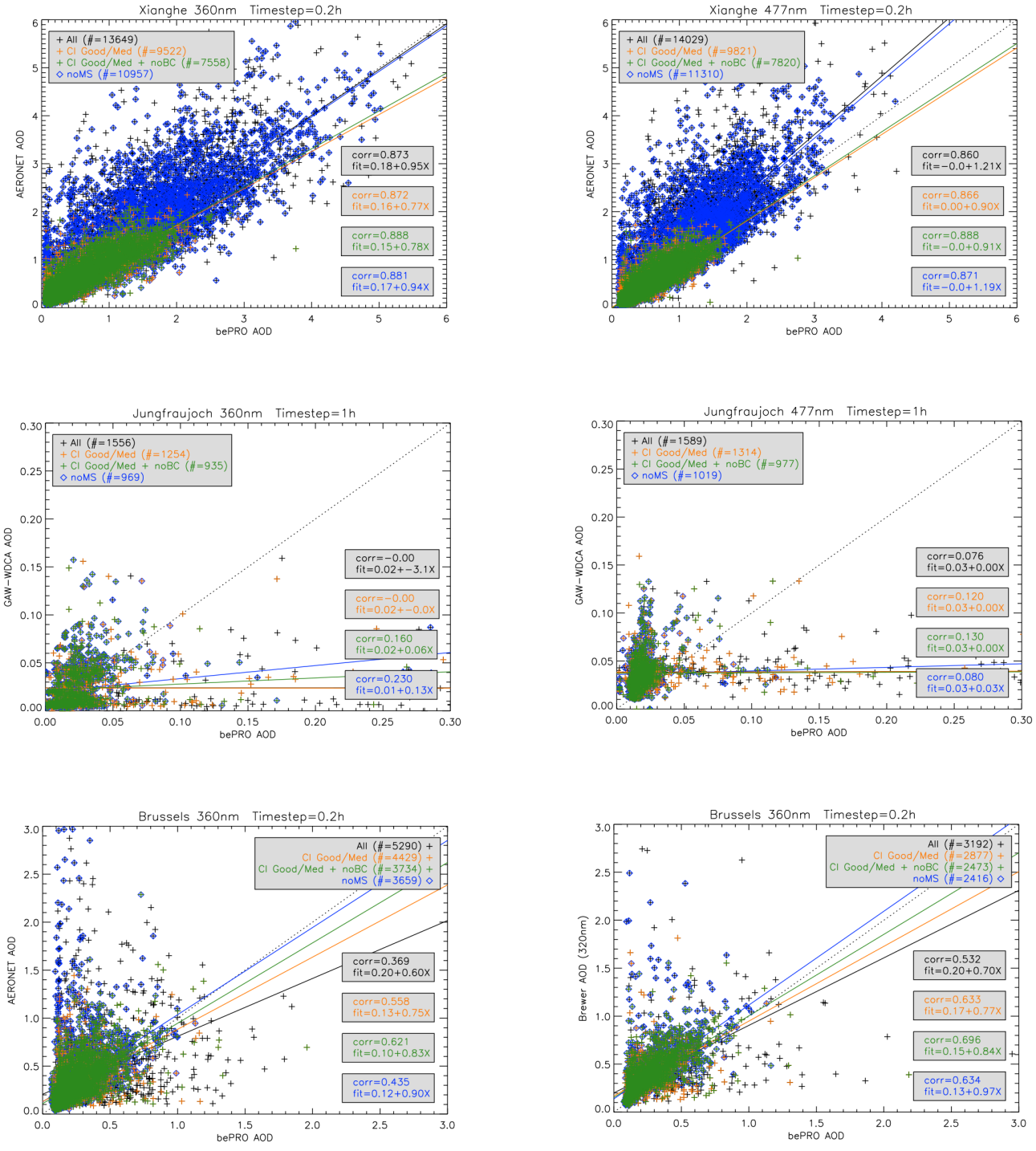

Figure 14. Correlation plots of our bePRO MAX-DOAS AOD retrievals and measured AOD values for the Xianghe and Jungfraujoch data set at 360 and 477 nm and for the Brussels at 360 nm, in time steps of 0.2 h. for Xianghe and Brussels and 1 h for Xianghe. The full non-cloud-screening data is given by black crosses. Cloud-screened data (based on the CI) with a "good/mediocre" sky flag are marked in orange, data with "good/mediocre" sky flag and no broken-cloud flag are marked in green crosses. Data with no multiple-scattering flag (based on the O_4 DSCDs) are marked with blue diamonds. For each sample set we also give the linear regression lines and correlation information.

but now using cloud-screened AERONET level-15 and Brewer data. For Jungfraujoch no such cloud-screened data are available. We find that the AERONET cloud-screening procedure (Smirnov et al., 2000), based on the stability of a measured AOD triplet over a 30 sec interval and temporal AOD hourly and diurnal variability, removes more data compared to our cloud screening, leaving around 28 % for Xianghe and 10 % for Brussels. This results in better correlation and slope values for both Xianghe and Brussels, compared to the correlation with the non-screened level-10 data, with improvement on average of the order of 0.05–0.1 for both R and S. As the AERONET cloud screening is based only on temporal variability of the AOD, stable uniform clouds and aerosol plumes can be misidentified. This could account for differences between our cloud-screening method and the AERONET screening, as for example seen in the first plot of Fig. 1. For this day with a strong rise in aerosol load, the second half of the day is flagged as mainly cloudy by AERONET, but not by us.

We also tested the effect of extending the zenith-based cloud flagging to extend CI flagging with information from the 30° elevation angle. Statistics on this procedure can be found in Table 1. On average we find that using both elevation angles results in a removal of ~ 10 % more data points. When we then retain only those measurements which are flagged as cloud-free by both the 30° and zenith CI flags, we find only a minor improvement in the observed correlation with co-located measurements. The improvement is highest for Brussels, as one would expect, since the 30° viewing angle will mainly provide additional information in the case of broken clouds. For Brussels we find an increase in the observed correlation of 0.06 to $R = 0.68$. For Jungfraujoch and Xianghe, the increase is 0.04 and 0.015 to $R = 0.2$ and $R = 0.9$ respectively. We do not see a change in the observed correlation slopes.

We conclude that our cloud screening has the largest influence on the Brussels data set, as expected due to it being the most cloudy site. For the Brussels and Jungfraujoch sites, it is sufficient to base the cloud screening on information from the colour index alone, whereas for Xianghe, additional information from O_4 DSCDs is invaluable for a correct cloud identification, as the colour index alone will result in a removal of non-cloudy data with high aerosol load.

7 Conclusions

We present a cloud-screening method for MAX-DOAS measurements to qualify the sky and cloud conditions. The method is based on the colour index (CI) and O_4 DSCD retrievals. We focus on colour-index observations made at zenith elevation, whereas for the O_4 DSCDs we use both the zenith and 30° data, but the method can be adapted to work only with zenith measurements. This means that the method is not only limited to MAX-DOAS instruments, but can also be applied to traditional zenith-sky DOAS measurements The cloud screening based on the CI has the advantage that it only needs two relative intensities, which can be measured by different types of non-DOAS instruments. The method based on the O_4 DSCDs has the advantage of giving better results for sites experiencing extreme aerosol concentrations and does not rely on simulations.

We use the calculated CI values combined with CI simulations to characterize the general sky conditions, in the form of the sky flag, and define three distinct regions corresponding to clear sky, slightly decreased visibility (thin clouds/aerosols), and strongly decreased visibility (thick clouds/extreme aerosols). At this point no distinction is made between a visibility decrease due to clouds and/or aerosols. The temporal variation of the CI is used to identify the presence of broken or scattered clouds, and is given by the broken-cloud flag. The third flag, the multiple-scattering flag, is based on the O_4 DSCDs and it detects (optically thick) clouds by tracing enhanced multiple scattering.

The values of the CI not only depend on the sky conditions, but also on the instrument characteristics and wavelength settings, and it is thus impossible to define a standardized method that is valid for all different measurement sites. For this reason we scale the calculated observed CI values to CI simulations. The drawback to this approach is that a substantial amount of data, which span observations under both good and bad sky conditions, is needed to verify the applied scaling. Additional data, such as from Cimel or Brewer instruments, can help resolve this issue. Ideally, all MAX-DOAS instruments should have well-defined and frequent calibration procedures, to eliminate the instrumental effects and allow for a direct comparison of the CI.

We applied our cloud-screening method to three large multi-year data sets of MAX-DOAS measurements in suburban and rural regions, namely Xianghe, Brussels and Jungfraujoch. All sites are characterized by different typical sky conditions: Xianghe is generally strongly polluted, with days of extreme aerosol loads. Brussels on the other hand shows only mild aerosol pollution but suffers from year-round cloudy conditions. The alpine station of Jungfraujoch shows very low aerosol pollution levels and average cloud pollution.

We find that our method works very well to identify observations made under cloudy conditions using only the colour index. In the case of Xianghe the method is even capable of discriminating between high AOD and high COD by using additional information from the O_4 DSCDs. For extremely cloud-prone sites like Brussels, our method removes up to 65 % of data after cloud screening. When we apply the cloud filter to our aerosol retrievals we find an improvement in the agreement with other co-located measurements, such as from Cimel and Brewer instruments, both in correlation and slope, which increases strongly for sites with the high cloud rates.

The Supplement related to this article is available online at doi:10.5194/amt-7-3509-2014-supplement.

Acknowledgements. This research was financially supported at IASB-BIRA by the Belgian Federal Science Policy Office, Brussels (AGACC-II project SD/CS/07A), the EU 7th Framework Programme projects NORS (contract 284421), and the ESA CEOS Intercalibration project (ESA/ESRIN contract 22202/09/I-EC). P. Stammes (KNMI) is acknowledged for providing us the DAK code.

Edited by: S. Beirle

References

Cheymol, A. and de Backer, H.: Retrieval of the aerosol optical depth in the UV-B at Uccle from Brewer ozone measurements over a long time period 1984–2002, J. Geophys. Res.-Atmos., 108, 4800, doi:10.1029/2003JD003758, 2003.

Clémer, K., Van Roozendael, M., Fayt, C., Hendrick, F., Hermans, C., Pinardi, G., Spurr, R., Wang, P., and De Mazière, M.: Multiple wavelength retrieval of tropospheric aerosol optical properties from MAXDOAS measurements in Beijing, Atmos. Meas. Tech., 3, 863–878, doi:10.5194/amt-3-863-2010, 2010.

De Bock, V., De Backer, H., Mangold, A., and Delcloo, A.: Aerosol Optical Depth measurements at 340 nm with a Brewer spectrophotometer and comparison with Cimel sunphotometer observations at Uccle, Belgium, Atmos. Meas. Tech., 3, 1577–1588, doi:10.5194/amt-3-1577-2010, 2010.

Frieß, U., Monks, P. S., Remedios, J. J., Rozanov, A., Sinreich, R., Wagner, T., and Platt, U.: MAX-DOAS O_4 measurements: a new technique to derive information on atmospheric aerosols: 2. Modeling studies, J. Geophys. Res.-Atmos., 111, D14203, doi:10.1029/2005JD006618, 2006.

Gillotay, D., Besnard, T., and Zanghi, F.: A systematic approach of the cloud cover by thermic infrared measurements, Proceedings of 18th Conference on Weather Analysis and Forecasting, Fort Lauderdale, Fl, USA, 30 July–2 August 2001, 292–295, 2001.

Hendrick, F., Müller, J.-F., Clémer, K., Wang, P., De Mazière, M., Fayt, C., Gielen, C., Hermans, C., Ma, J. Z., Pinardi, G., Stavrakou, T., Vlemmix, T., and Van Roozendael, M.: Four years of ground-based MAX-DOAS observations of HONO and NO_2 in the Beijing area, Atmos. Chem. Phys., 14, 765–781, doi:10.5194/acp-14-765-2014, 2014.

Hermans, C., Vandaele, A., Fally, S., Carleer, M., Colin, R., Coquart, B., Jenouvrier, A., and Merienne, M.-F.: Absorption cross-section of the collision-induced bands of oxygen from the UV to the NIR, vol. 27 of NATO Science Series, Springer, the Netherlands, doi:10.1007/978-94-010-0025-3_16, 2003.

Holben, B. N., Tanré, D., Smirnov, A., Eck, T. F., Slutsker, I., Abuhassan, N., Newcomb, W. W., Schafer, J. S., Chatenet, B., Lavenu, F., Kaufman, Y. J., Castle, J. V., Setzer, A., Markham, B., Clark, D., Frouin, R., Halthore, R., Karneli, A., O'Neill, N. T., Pietras, C., Pinker, R. T., Voss, K., and Zibordi, G.: An emerging ground-based aerosol climatology: aerosol optical depth from AERONET, J. Geophys. Res.-Atmos., 106, 12067, doi:10.1029/2001JD900014, 2001.

Hönninger, G., von Friedeburg, C., and Platt, U.: Multi axis differential optical absorption spectroscopy (MAX-DOAS), Atmos. Chem. Phys., 4, 231–254, doi:10.5194/acp-4-231-2004, 2004.

Ma, J. Z., Beirle, S., Jin, J. L., Shaiganfar, R., Yan, P., and Wagner, T.: Tropospheric NO_2 vertical column densities over Beijing: results of the first three years of ground-based MAX-DOAS measurements (2008–2011) and satellite validation, Atmos. Chem. Phys., 13, 1547–1567, doi:10.5194/acp-13-1547-2013, 2013.

Nyeki, S., Halios, C. H., Baum, W., Eleftheriadis, K., Flentje, H., Gröbner, J., Vuilleumier, L., and Wehrli, C.: Ground-based aerosol optical depth trends at three high-altitude sites in Switzerland and southern Germany from 1995 to 2010, J. Geophys. Res.-Atmos., 117, D18202, doi:10.1029/2012JD017493, 2012.

Piters, A. J. M., Boersma, K. F., Kroon, M., Hains, J. C., Van Roozendael, M., Wittrock, F., Abuhassan, N., Adams, C., Akrami, M., Allaart, M. A. F., Apituley, A., Beirle, S., Bergwerff, J. B., Berkhout, A. J. C., Brunner, D., Cede, A., Chong, J., Clémer, K., Fayt, C., Frieß, U., Gast, L. F. L., Gil-Ojeda, M., Goutail, F., Graves, R., Griesfeller, A., Großmann, K., Hemerijckx, G., Hendrick, F., Henzing, B., Herman, J., Hermans, C., Hoexum, M., van der Hoff, G. R., Irie, H., Johnston, P. V., Kanaya, Y., Kim, Y. J., Klein Baltink, H., Kreher, K., de Leeuw, G., Leigh, R., Merlaud, A., Moerman, M. M., Monks, P. S., Mount, G. H., Navarro-Comas, M., Oetjen, H., Pazmino, A., Perez-Camacho, M., Peters, E., du Piesanie, A., Pinardi, G., Puentedura, O., Richter, A., Roscoe, H. K., Schönhardt, A., Schwarzenbach, B., Shaiganfar, R., Sluis, W., Spinei, E., Stolk, A. P., Strong, K., Swart, D. P. J., Takashima, H., Vlemmix, T., Vrekoussis, M., Wagner, T., Whyte, C., Wilson, K. M., Yela, M., Yilmaz, S., Zieger, P., and Zhou, Y.: The Cabauw Intercomparison campaign for Nitrogen Dioxide measuring Instruments (CINDI): design, execution, and early results, Atmos. Meas. Tech., 5, 457–485, doi:10.5194/amt-5-457-2012, 2012.

Platt, U. and Stutz, J.: Differential Optical Absorption Spectroscopy, Springer-Verlag, Berlin, 2008.

Rodgers, C. D.: Inverse Methods for Atmospheric Sounding – Theory and Practice, Series: Series on Atmospheric Oceanic and Planetary Physics, edited by: Rodgers C. D., World Scientific Publishing Co. Pte. Ltd., vol. 2, 2, Singapore, 2000.

Roscoe, H. K., Van Roozendael, M., Fayt, C., du Piesanie, A., Abuhassan, N., Adams, C., Akrami, M., Cede, A., Chong, J., Clémer, K., Friess, U., Gil Ojeda, M., Goutail, F., Graves, R., Griesfeller, A., Grossmann, K., Hemerijckx, G., Hendrick, F., Herman, J., Hermans, C., Irie, H., Johnston, P. V., Kanaya, Y., Kreher, K., Leigh, R., Merlaud, A., Mount, G. H., Navarro, M., Oetjen, H., Pazmino, A., Perez-Camacho, M., Peters, E., Pinardi, G., Puentedura, O., Richter, A., Schönhardt, A., Shaiganfar, R., Spinei, E., Strong, K., Takashima, H., Vlemmix, T., Vrekoussis, M., Wagner, T., Wittrock, F., Yela, M., Yilmaz, S., Boersma, F., Hains, J., Kroon, M., Piters, A., and Kim, Y. J.: Intercomparison of slant column measurements of NO_2 and O_4 by MAX-DOAS and zenith-sky UV and visible spectrometers, Atmos. Meas. Tech., 3, 1629–1646, doi:10.5194/amt-3-1629-2010, 2010.

Smirnov, A., Holben, B., Eck, T., Dubovik, O., and Slutsker, I.: Cloud-Screening and Quality Control Algorithms for the

AERONET Database, Remote Sens. Environ., 73, 337–349, doi:10.1016/S0034-4257(00)00109-7, 2000.

Stammes, P.: Spectral radiance modelling in the UV-visible range, Proceedings IRS-2000: Current Problems in Atmospheric Radiation, edited by: Smith, W. L. and Timofeyev, Y. M., A. Deepak Publ., Hampton, 181–184, 2001.

Stammes, P., de Haan, J. F., and Hovenier, J. W.: The polarized internal radiation field of a planetary atmosphere, Astron. Astrophys., 225, 239–259, 1989.

Wagner, T., Dix, B., Friedeburg, C. v., Frieß, U., Sanghavi, S., Sinreich, R., and Platt, U.: MAX-DOAS O4 measurements: a new technique to derive information on atmospheric aerosols, principles and information content, J. Geophys. Res., 109, D22205, doi:10.1029/2004JD004904, 2004.

Wagner, T., Beirle, S., Brauers, T., Deutschmann, T., Frieß, U., Hak, C., Halla, J. D., Heue, K. P., Junkermann, W., Li, X., Platt, U., and Pundt-Gruber, I.: Inversion of tropospheric profiles of aerosol extinction and HCHO and NO_2 mixing ratios from MAX-DOAS observations in Milano during the summer of 2003 and comparison with independent data sets, Atmos. Meas. Tech., 4, 2685–2715, doi:10.5194/amt-4-2685-2011, 2011.

Wagner, T., Apituley, A., Beirle, S., Dörner, S., Friess, U., Remmers, J., and Shaiganfar, R.: Cloud detection and classification based on MAX-DOAS observations, Atmos. Meas. Tech., 7, 1289–1320, doi:10.5194/amt-7-1289-2014, 2014.

Atmos. Chem. Phys., 12, 8851–8864, 2012
www.atmos-chem-phys.net/12/8851/2012/
doi:10.5194/acp-12-8851-2012

Atmospheric Chemistry and Physics

Analysis of stratospheric NO_2 trends above Jungfraujoch using ground-based UV-visible, FTIR, and satellite nadir observations

F. Hendrick[1], E. Mahieu[2], G. E. Bodeker[3], K. F. Boersma[4,5], M. P. Chipperfield[6], M. De Mazière[1], I. De Smedt[1], P. Demoulin[2], C. Fayt[1], C. Hermans[1], K. Kreher[7], B. Lejeune[2], G. Pinardi[1], C. Servais[2], R. Stübi[8], R. van der A[4], J.-P. Vernier[9,10], and M. Van Roozendael[1]

[1]Belgian Institute for Space Aeronomy (BIRA-IASB), Brussels, Belgium
[2]Institute of Astrophysics and Geophysics of the University of Liège, Liège, Belgium
[3]Bodeker Scientific, Alexandra, New Zealand
[4]Royal Netherlands Meteorological Institute (KNMI), De Bilt, The Netherlands
[5]Eindhoven University of Technology, Eindhoven, The Netherlands
[6]School of Earth and Environment, University of Leeds, Leeds, UK
[7]National Institute of Water and Atmospheric Research, Omakau, Central Otago, New Zealand
[8]MeteoSwiss, Payerne, Switzerland
[9]Science Systems and Applications, Inc., Hampton, Virginia, USA
[10]NASA Langley Research Center, Hampton, Virginia, USA

Correspondence to: F. Hendrick (franch@oma.be)

Received: 15 March 2012 – Published in Atmos. Chem. Phys. Discuss.: 15 May 2012
Revised: 29 August 2012 – Accepted: 11 September 2012 – Published: 28 September 2012

Abstract. The trend in stratospheric NO_2 column at the NDACC (Network for the Detection of Atmospheric Composition Change) station of Jungfraujoch (46.5° N, 8.0° E) is assessed using ground-based FTIR and zenith-scattered visible sunlight SAOZ measurements over the period 1990 to 2009 as well as a composite satellite nadir data set constructed from ERS-2/GOME, ENVISAT/SCIAMACHY, and METOP-A/GOME-2 observations over the 1996–2009 period. To calculate the trends, a linear least squares regression model including explanatory variables for a linear trend, the mean annual cycle, the quasi-biennial oscillation (QBO), solar activity, and stratospheric aerosol loading is used. For the 1990–2009 period, statistically indistinguishable trends of $-3.7 \pm 1.1\,\%\,\mathrm{decade}^{-1}$ and $-3.6 \pm 0.9\,\%\,\mathrm{decade}^{-1}$ are derived for the SAOZ and FTIR NO_2 column time series, respectively. SAOZ, FTIR, and satellite nadir data sets show a similar decrease over the 1996–2009 period, with trends of $-2.4 \pm 1.1\,\%\,\mathrm{decade}^{-1}$, $-4.3 \pm 1.4\,\%\,\mathrm{decade}^{-1}$, and $-3.6 \pm 2.2\,\%\,\mathrm{decade}^{-1}$, respectively. The fact that these declines are opposite in sign to the globally observed $+2.5\,\%\,\mathrm{decade}^{-1}$ trend in N_2O, suggests that factors other than N_2O are driving the evolution of stratospheric NO_2 at northern mid-latitudes. Possible causes of the decrease in stratospheric NO_2 columns have been investigated. The most likely cause is a change in the NO_2/NO partitioning in favor of NO, due to a possible stratospheric cooling and a decrease in stratospheric chlorine content, the latter being further confirmed by the negative trend in the $ClONO_2$ column derived from FTIR observations at Jungfraujoch. Decreasing ClO concentrations slows the $NO + ClO \rightarrow NO_2 + Cl$ reaction and a stratospheric cooling slows the $NO + O_3 \rightarrow NO_2 + O_2$ reaction, leaving more NO_x in the form of NO. The slightly positive trends in ozone estimated from ground- and satellite-based data sets are also consistent with the decrease of NO_2 through the $NO_2 + O_3 \rightarrow NO_3 + O_2$ reaction. Finally, we cannot rule out the possibility that a strengthening of the Dobson-Brewer circulation, which reduces the time available for N_2O photolysis in the stratosphere, could also contribute to the observed decline in stratospheric NO_2 above Jungfraujoch.

Published by Copernicus Publications on behalf of the European Geosciences Union.

1 Introduction

Nitrogen dioxide (NO_2) plays an important role in controlling ozone abundances in the stratosphere (Solomon, 1999), either by destroying ozone through the NO_x ($NO + NO_2$) catalytic destruction cycles, or by mitigating ozone destruction by converting active chlorine, hydrogen, and bromine into their reservoir forms ($ClONO_2$, HNO_3, and $BrONO_2$, respectively). The primary source of NO_x is the oxidation of nitrous oxide (N_2O) in the middle stratosphere. N_2O is an important greenhouse gas and its emissions in the troposphere are known to be increasing by 2.5–3 % per decade (Liley et al., 2000), mainly due to agricultural activity. Monitoring long-term changes in stratospheric NO_2 is essential for attributing observed changes in stratospheric ozone. However, few studies of the long-term evolution of stratospheric NO_2 have been published to date. Liley et al. (2000) reported an increase in stratospheric NO_2 of about 5 % decade^{-1} from ground-based zenith-scattered visible sunlight measurements at Lauder, New Zealand (45° S, 170° E) between 1981 and 1999. Recently, Dirksen et al. (2011) further confirmed an increase of NO_2 of 5 % decade^{-1} over this station for the 1981–2010 period also from ground-based UV-visible data. Using 3-D-Chemical Transport Model calculations, McLinden et al. (2001) suggested that the 5 % decade^{-1} NO_2 trend from 1981 to 1999 results from a 2.5 % decade^{-1} increase due to rising N_2O emissions and further 2.5 % decade^{-1} increase resulting from a decrease in stratospheric ozone. The abundance of NO_2 in the stratosphere can be affected by ozone through the following reaction (Fish et al., 2000):

$$NO_2 + O_3 \rightarrow NO_3 + O_2 \quad \text{(R1)}$$

Gruzdev (2009) investigated the latitudinal structure of the stratospheric NO_2 trend using ground-based zenith-sky UV-visible and FTIR observations from a selection of 23 sites within the Network for the Detection of Atmospheric Composition Change (NDACC). This study, performed over different time periods between 1983 and 2007, showed that the NO_2 trend is predominantly positive at mid-latitudes in the Southern Hemisphere while negative trends are observed at most Northern Hemisphere mid-latitude sites. Cook and Roscoe (2009) inferred trends in stratospheric NO_2 from measurements obtained during the 1990–2007 period from a zenith-sky UV-visible spectrometer in the Antarctic. The NO_2 trend strongly depends on the period, with a positive trend of $\sim$10 % decade^{-1} from 1990 to 2000, a negative trend of $\sim$20 % decade^{-1} from 2000 to 2007, and no overall trend for the full time period. These studies show that the trend in stratospheric NO_2 has a complicated structure which does not always follow the evolution of its main source (N_2O) and displays a strong dependence on the location and time period considered for the trend analysis.

Trends in stratospheric NO_2 at the Jungfraujoch NDACC station in the Swiss Alps (46.5° N, 8.0° E) are quantified and interpreted below. Ground-based UV-visible SAOZ (Système d'Analyse par Observation Zénithale) and Fourier Transform Infra-Red (FTIR) spectrometers have been operating continuously at this station since 1990 and 1985, respectively, providing more than two decades of measurements. A combination of stratospheric NO_2 columns retrieved from the ERS-2/GOME (1996–2003), ENVISAT/SCIAMACHY (2003–2009), and METOP-A/ GOME-2 (2007–2009) satellite nadir instruments is also included in this study, permitting, for the first time, a thorough analysis of the long-term evolution of stratospheric NO_2 from three (two ground-based and one satellite) independent measurement techniques at this site. The paper is divided into 4 sections. Section 2 provides a description of the ground-based and satellite data sets. The consistency between the different data sets is investigated in Sect. 3 through comparisons between (1) ground-based FTIR and UV-visible NO_2 column time series, and (2) satellite and ground-based UV-visible observations. In Sect. 4, the linear least squares regression model used for the trend study is described and the results of the trend analyses are presented and discussed. Conclusions are given in Sect. 5.

2 Data sets

2.1 SAOZ observations

The SAOZ instrument is a broad-band (300–600 nm), medium resolution ($\sim$1 nm) diode-array spectrometer that measures zenith scattered sunlight (Pommereau and Goutail, 1988). Between 1990 and 2009 two different versions of the SAOZ instrument were used. The first (NMOS) described in Van Roozendael et al. (1994) is based on a Jobin-Yvon spectrometer (model CP200) coupled to a 512 diode Hamamatsu NMOS detector. In December 1998, the system was upgraded to a 1024 diode Hamamatsu detector. This second version (SAM) provides low sun spectra with a better resolution and a higher signal to noise ratio than the NMOS version.

Zenith radiance spectra are analyzed using the DOAS (Differential Optical Absorption Spectroscopy) technique (Platt and Stutz, 2008). NO_2 is retrieved in the 425–490 nm wavelength range, taking into account the spectral signatures of NO_2, O_3, H_2O, O_4, and the filling-in of the solar Fraunhofer bands by the Ring effect (Grainger and Ring, 1962). The NO_2 absorption cross-sections at 220 K are from Vandaele et al. (1998). A third-order polynomial is used to fit the low frequency spectral structure due to molecular and Mie scattering.

NO_2 vertical column densities are derived from vertical profiles retrieved by applying a profiling technique to sunrise and sunset NO_2 differential slant column densities (DSCDs) which are the direct product of the DOAS analysis. The profiling algorithm is based on the Optimal Estimation Method (OEM; Rodgers, 2000) and is described in Hendrick

et al. (2004). In brief, a profile $\widehat{\mathbf{x}}$ is retrieved given an a priori profile $\mathbf{x}_a$, the measurements $\mathbf{y}$ (here, twilight NO_2 DSCDs as a function of solar zenith angle (SZA)), their respective uncertainty covariance matrices ($\mathbf{S}_a$ and $\mathbf{S}_\varepsilon$), and the matrix $\mathbf{K}$ of the weighting functions. Since NO_2 is an optically thin absorber, the OEM for the linear case can be considered:

$$\widehat{\mathbf{x}} = \mathbf{x}_a + \mathbf{S}_a\mathbf{K}^T(\mathbf{K}\mathbf{S}_a\mathbf{K}^T + \mathbf{S}_\varepsilon)^{-1}(\mathbf{y} - \mathbf{K}\,\mathbf{x}_a) \quad (1)$$

with $\mathbf{K} = \frac{\partial \mathbf{y}}{\partial \mathbf{x}}$ and $\mathbf{K}^T$ is the transpose of $\mathbf{K}$.

The weighting functions indicate the sensitivity of the measurements to a change in the vertical profile. The matrix $\mathbf{K}$ is determined by consecutively perturbing each layer of the a priori profile and recalculating the set of measurements using the so-called forward model which describes the physics of the measurements. Here, the forward model consists of the stacked photochemical box model PSCBOX coupled to the radiative transfer model (RTM) UVSPEC/DISORT (see Hendrick et al., 2004, 2006 for further details about both models). The photochemical model, initialized daily with chemical and meteorological fields from the SLIMCAT 3-D-CTM (Chipperfield et al., 2006), is able to simulate the rapid variation of NO_2 at twilight. The model also provides a priori profiles to the profiling algorithm and is used to photochemically convert the retrieved profiles, which are representative of twilight conditions, to the mean SZA corresponding to the FTIR and satellite nadir observations. The DSCDs are analyzed using daily reference spectra and the effective residual amounts of NO_2 in the reference spectra are directly fitted by the profiling algorithm. Combining this with an a priori tropospheric NO_2 content close to zero leads to retrieved vertical profiles and corresponding vertical columns mainly representative of the stratosphere (Hendrick et al., 2004, 2008). Performing the DOAS analysis with daily reference spectra also minimizes the potential impact of any long-term degradation of the instrument on the NO_2 vertical column time series, which is important for calculating robust trends. NO_2 profile retrievals are quality-checked based on the retrieval fit residual (RMS of the difference between measured SCDs and those calculated using the retrieved profiles; see Hendrick et al., 2004). In practice, all retrievals with a residual larger than 3.5×10^{15} molec cm^{-2} are rejected. This method of selection excludes measurements contaminated by tropospheric NO_2 which usually display short-term variability inconsistent with the expected smooth variation of the stratospheric slant column during twilight. A detailed error budget can be found in Hendrick et al. (2004). Taking into account the smoothing error, the retrieval noise, and the forward model parameter error, the total relative uncertainty on the retrieved stratospheric NO_2 columns is about 8 % on average. High aerosol loading can also perturb UV-visible measurements by modifying the scattering geometry. During the period considered in this study (1990–2009), the Mount Pinatubo eruption in June 1991 injected large amounts of aerosols into the stratosphere. In the years immediately following this event (1991–1994), an extinction profile corresponding to a volcanic aerosol loading was selected from the aerosol model of Shettle (1989) and included in the UVSPEC/DISORT RTM for the calculation of the weighting functions needed for the OEM-based profile retrieval. Before and after the 1991–1994 period, a background aerosol extinction profile was used. Sensitivity tests have shown that the use of an aerosol extinction profile corresponding to volcanic conditions has an impact of up to 10 % on the retrieved stratospheric NO_2 columns. Aerosol loading changes due to the Mount Pinatubo eruption are also implemented in the SLIMCAT model through the use of monthly zonal mean time series of surface sulfate area density created from different satellite data sets (more details are available at http://homepages.see.leeds.ac.uk/~lecmc/sparc/Forcings/SPARC_Forcings_WMO2011.html).

We have also estimated the impact on the SAOZ columns of using the NO_2 cross-sections at 220 K only instead of taking into account the variation of the NO_2 cross-sections with the stratospheric temperature. Sensitivity tests in the 425–490 nm range using the Vandaele et al. (1998) NO_2 cross-sections at 220 and 294 K show an increase of the NO_2 slant column density of 20 % from 220 to 294 K, i.e. an increase of 0.3 %/ K assuming a linear temperature dependence. The NO_2 effective temperature, defined as the mean temperature of the stratosphere weighted by the NO_2 concentration profile (Gil et al., 2008), is calculated using the temperature and NO_2 vertical profiles from the SLIMCAT/PSCBOX model. At Jungfraujoch, it ranges on average from 212 K in winter to 232 K in summer. This means that the correction for the difference between 220 K and the NO_2 effective temperature to be applied to the SAOZ NO_2 columns is of -2.4 % in winter and +3.6 % in summer. On average over the year, we can therefore expect slightly larger SAOZ NO_2 columns when applying a correction for the variation of the stratospheric temperature. Consequently, the temperature dependence of the NO_2 cross-sections cannot explain the negative trends inferred from this data set (see Sect. 4.2).

2.2 Ground-based FTIR observations

In the early 1950s, M. Migeotte performed pioneering atmospheric infrared observations at the Jungfraujoch. Since then, the University of Liège has operated state-of-the-art instruments at that site to record high-resolution spectra allowing production of atlases of the solar spectrum and monitoring of the state of the Earth's atmosphere (Zander et al., 2008 and references therein). This long-term commitment has allowed the collection of a unique observational data base in terms of quality, time extension and measurement density. FTIR high-resolution solar absorption spectra have been recorded regularly under clear-sky conditions since 1985 with a homemade instrument, backed-up in the early 1990s by a commercial

Bruker IFS-120HR. Over the time period of interest here, spectra were obtained on average on 115 days per year.

For this study, all available observations since 1990 have been fitted with the V3.91 of the SFIT-2 algorithm, using pressure and temperature information provided by the National Centers for Environmental Prediction (NCEP, see http://www.ncep.noaa.gov) and assuming the HITRAN 2004 spectroscopic line parameter compilation, including the August 2006 updates (Rothmann et al., 2004, see also http://www.cfa.harvard.edu/hitran). The SFIT-2 code also implements the OEM (Rodgers, 2000), enabling the derivation of the vertical distributions of most of the FTIR target gases (e.g., Pougatchev and Rinsland, 1995; Rinsland et al., 2003a). In the present case, two microwindows ranging from 2914.6 to 2914.7 cm^{-1} and from 2915 to 2915.11 cm^{-1} have been fitted; a priori vertical profiles for fitted (H_2O, CH_4 and O_3 scaled during the retrieval process) and simulated interferences (e.g. H_2CO) were based on predictions obtained with the version 5 of the WACCM model (Whole-Atmosphere Community Climate Model, see Chang et al., 2008). For NO_2, we used 12 monthly profiles based on the same PSCBOX/SLIMCAT modeled a priori profile data set as for the SAOZ profile retrieval (see Sect. 2.1). The forward model was characterized by a diagonal covariance of 40 % per km and, with extra-diagonal elements based on a Gaussian half-width for interlayer correlation of 4 km. Regarding the error budget, estimates reported in Table 2 of Rinsland et al. (2003a) remain valid (total random and systematic errors of 11 % and 36 %, respectively), although they can be considered as conservative.

2.3 Satellite nadir observations

GOME, SCIAMACHY, and GOME-2 stratospheric NO_2 columns are retrieved using the KNMI/BIRA TEMIS NO_2 algorithm (Boersma et al., 2004, 2007; Dirksen et al., 2011). For this study, we use versions TM4NO2A v1.04 for GOME and TM4NO2A v1.10 for SCIAMACHY and GOME-2, and the periods covered by the different instruments are 1995–2003, 2002–2009, and 2007–2009, respectively. The TEMIS algorithm is based on a two-step process including (1) the retrieval of NO_2 slant columns with the DOAS method, and (2) the estimation of the stratospheric component of the NO_2 slant columns through data assimilation in the TM4 chemistry transport model. The purpose of the assimilation is to regularly update the TM4 simulation with available measurements such that the model simulation of the stratospheric NO_2 column is closely constrained by the satellite measurements. In step 1, the DOAS analysis is performed in the following wavelength ranges: 425–450 nm for GOME and GOME-2 and 426.5–451.5 nm for SCIAMACHY. Absorption by NO_2, ozone, water vapor, the Ring effect, and a third-order polynomial that describes the residual broadband features due to Rayleigh and Mie scattering are taken into account. The NO_2 cross-sections set at 220 K from Vandaele et al. (1998) is used. A correction for the difference between 220 K and the effective temperature of NO_2 along the light path is applied to the NO_2 absorption cross-sections. The stratospheric NO_2 vertical columns are calculated by dividing the assimilated stratospheric slant columns by a simple geometrical airmass factor depending only on the SZA and viewing angle (Boersma et al., 2004). The estimated error on TEMIS stratospheric NO_2 columns is about 0.2–0.3×10^{15} molec cm^{-2} (Boersma et al., 2004; Dirksen et al., 2011).

For this study, all pixels falling within a radius of 300 km around Jungfraujoch were selected and no filtering based on the cloud fraction was applied.

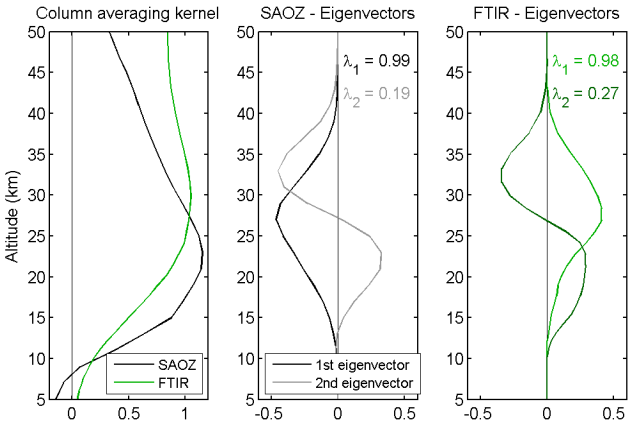

Fig. 1. Typical FTIR and SAOZ column averaging kernels (left plot) and leading eigenvectors and corresponding eigenvalues (middle plot: SAOZ; right plot: FTIR). The sum of the latter gives the DOFS.

3 Evaluation of data consistency

3.1 FTIR and SAOZ data sets comparison

First, we have compared the information content associated with both FTIR and SAOZ profile retrievals. As can be seen in Fig. 1, column averaging kernels are very similar for both techniques with no sensitivity to NO_2 in the troposphere and a maximum sensitivity between 20 and 35 km altitude where the NO_2 concentration in the stratosphere is the largest. Figure 1 also presents the eigenvector expansion of the averaging kernel matrix **A** corresponding to the two largest eigenvalues. The first eigenvalue, close to unity, implies an almost 100 % contribution of the measurements in this pattern (Hendrick et al., 2004). This pattern also indicates that the altitude range with high sensitivity to the NO_2 vertical distribution is $\sim$ 13–40 km for both retrievals. The number of independent pieces of information, also called the degree of freedom for signal (DOFS), given by the trace of the matrix **A** (Rodgers, 2000), is about 1.2 in both cases. From this information content assessment, it can be concluded that both

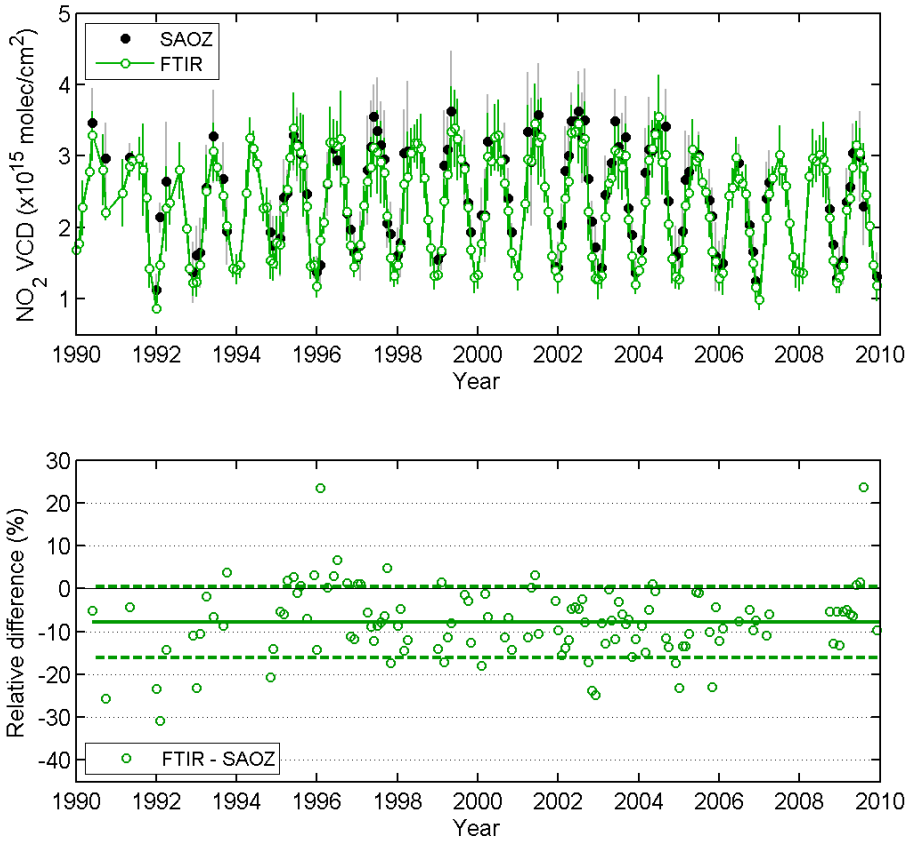

Fig. 2. Comparison between FTIR and SAOZ monthly mean stratospheric NO_2 columns at Jungfraujoch (46.5° N, 8° E) for the 1990–2009 period. The error bars correspond to the 1-sigma standard deviation (natural variability). The relative differences appear on the lower plot with solid and dashed green lines corresponding to the mean FTIR – SAOZ difference and its 1-sigma standard deviation, respectively, which is -7.8 ± 8.2 %.

FTIR and SAOZ retrievals have similar vertical resolution and sensitivity to the vertical distribution of NO_2 and therefore retrieved NO_2 columns can be directly compared.

The consistency between ground-based FTIR and SAOZ data sets is evaluated by comparing the monthly mean stratospheric NO_2 columns for the 1990–2009 period (see Fig. 2). To ensure photochemical matching, i.e. comparison in the same photochemical conditions, the SAOZ profiles and corresponding columns, representative of twilight conditions, are converted on a daily basis to the mean FTIR measurement SZA using the PSCBOX photochemical model of the SAOZ profiling algorithm forward model (see Sect. 2.1). FTIR and SAOZ data sets are in good agreement, with FTIR measurements lower than SAOZ by 7.8 ± 8.2 % on average.

Combining the facts that both retrievals used similar a priori profiles and have similar sensitivity to the vertical distribution of NO_2, the remaining differences between FTIR and SAOZ NO_2 columns are consistent with the uncertainties affecting the respective spectroscopic parameters.

3.2 SAOZ and satellite nadir data sets comparison

SAOZ and satellite nadir (GOME, SCIAMACHY, and GOME-2) monthly mean stratospheric NO_2 columns are compared in Fig. 3. The retrieved SAOZ columns are photochemically converted to the satellite overpass SZA in order to perform comparisons under the same photochemical conditions. A good agreement is obtained with mean satellite minus SAOZ relative differences of $+0.9 \pm 8.8$ % (GOME), $+1.9 \pm 11.5$ % (SCIAMACHY), and $+2.3 \pm 11.6$ % (GOME-2), i.e. not significant at the 1-sigma uncertainty level. Based on these results, the composite satellite data set of monthly mean NO_2 columns used for trend analysis is constructed as follows: GOME data for the March 1996–June 2003 period, SCIAMACHY data for the July 2003–March 2007 period, and a merging of the SCIAMACHY and GOME-2 data for the April 2007–December 2009 period, given the fact that the biases between both satellite data sets and SAOZ observations are similar.

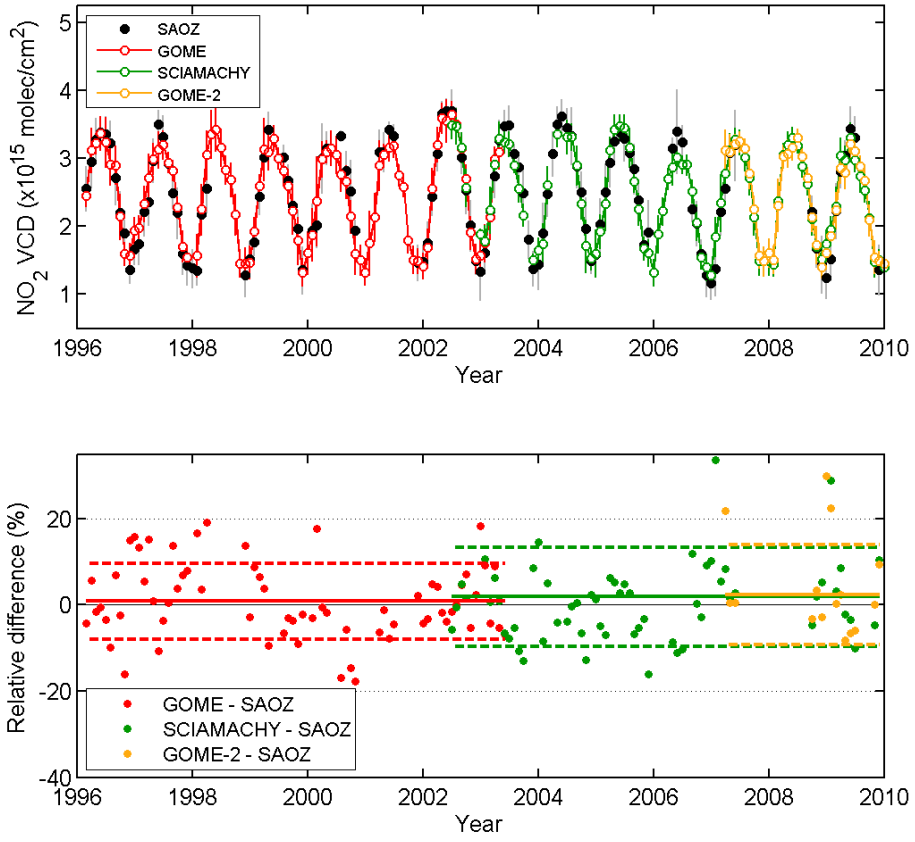

Fig. 3. Comparison between SAOZ and satellite nadir (GOME, SCIAMACHY, and GOME-2) monthly mean stratospheric NO_2 columns at Jungfraujoch (46.5° N, 8° E) for the 1996–2009 period. The error bars correspond to the 1-sigma standard deviation (natural variability). The relative differences appear on the lower plot with solid and dashed colored lines corresponding to the mean satellite – SAOZ differences and their one-sigma standard deviation, respectively, which are $+0.9 \pm 8.8$ % (GOME), $+1.9 \pm 11.5$ % (SCIAMACHY), and $+2.3 \pm 11.6$ % (GOME-2).

4 Trend analysis

4.1 Statistical model description

To extract the linear trend in the stratospheric NO_2 vertical column time series, a linear least squares regression model is fitted to the data to account for any extraneous variability that might affect the trend or its uncertainty. A modified version of the regression model developed by Bodeker et al. (1998) is used. It includes terms for offset, linear trend, quasi-biennial oscillation (QBO), solar activity, and aerosols effect, i.e.:

$$\begin{aligned} &m(t) = A(\mathrm{N}_A = 2) + \\ &B(\mathrm{N}_B = 2) \times t + \\ &C(\mathrm{N}_C = 2) \times \mathrm{QBO}(t) + \\ &D(\mathrm{N}_D = 0) \times \mathrm{Solar}(t) + \\ &E(\mathrm{N}_E = 1) \times \mathrm{Aerosols}(t) + \\ &U\delta \end{aligned} \tag{2}$$

where $m(t)$ is the statistically modeled monthly NO_2 vertical column at decimal year t and A–E are the model coefficients expanded as (for example):

$$A = A_0 + \sum_{k=1}^{\mathrm{N}_A} \left[A_{2k-1} \sin(2\pi kt) + A_{2k} \cos(2\pi kt) \right] \tag{3}$$

to fit seasonality. The N_A to N_E coefficient values appear in Eq. (2). U accounts for a possible bias between the GOME and SCIAMACHY/GOME-2 columns (δ switches from 1 to 0 in July 2003). A similar approach is applied to the SAOZ data set to account for any bias after April 1998 resulting from the installation of the new version of the SAOZ instrument.

The QBO basis function is based on the 30 and 50 hPa Singapore monthly mean zonal winds (http://www.geo.fu-berlin.de/met/ag/strat/produkte/qbo/index.html). Using these two pressure levels separately allows a covering of the altitude range of the stratospheric NO_2 profile and an automatic fitting of the phase of the QBO. For the solar cycle basis function, the radio-frequency

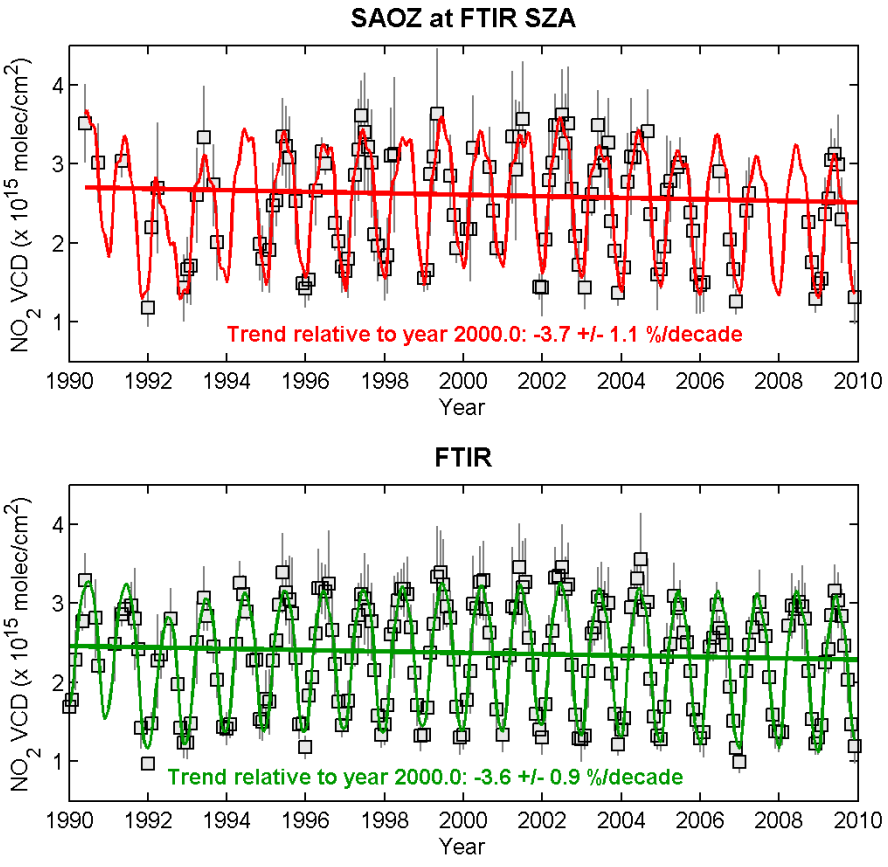

Fig. 4. Results of the trend analysis over the 1990–2009 period using the ground-based UV-visible SAOZ and FTIR monthly mean NO_2 vertical column densities (VCD; grey squares). Twilight SAOZ columns are photochemically converted to the mean SZA of the FTIR measurements. Colored lines correspond to the linear trend (thick line) and to the NO_2 columns recalculated using the multiple linear regression model (thin line). The error bars correspond to the 1-sigma standard deviation.

F10.7 cm solar flux (ftp://ftp.ngdc.noaa.gov/STP/SOLAR_DATA/SOLAR_RADIO/FLUX) is used. The aerosols basis function is based on the stratospheric aerosol optical depth (AOD) climatology of Vernier et al. (2011) created from SAGE II, CALIPSO, and ENVISAT/GOMOS observational data sets. The AOD time series corresponding to the 20° N–50° N latitude band was extracted for this study. This climatology includes the large changes in aerosol loading related to the Mount Pinatubo eruption as well as smaller changes due to a series of moderate volcanic eruptions, primarily at tropical latitudes, causing an increase in the stratospheric aerosol loading since 2002 (Vernier et al., 2011).

The standard deviation σ_B on a trend B can be calculated using the standard deviation σ_N of the fit residuals (differences between modelled and observed NO_2 columns) and their autocorrelation coefficient ϕ (Weatherhead et al., 1998; van der A et al., 2006):

$$\sigma_B = \frac{\sigma_N}{n^{3/2}} \sqrt{\frac{1+\phi}{1-\phi}} \tag{4}$$

where n is the length of the time series.

A test of the significance of the trend B can be computed as the ratio between the trend and its standard deviation:

$$t_B = |B/\sigma_B| \tag{5}$$

A commonly applied decision rule for trend detection is that a trend is real at a 95 % confidence level when $t_B > 2$ (Weatherhead et al., 1998; Santer et al., 2000).

4.2 Results and discussion

Figure 4 shows the regression fits to the SAOZ and FTIR monthly mean time series and the derived trends over the period 1990–2009. The SAOZ-based trend (-3.7 ± 1.1 % decade^{-1}; 1-sigma uncertainty) agrees with the FTIR-based trend (-3.6 ± 0.9 % decade^{-1}). The contributions of the QBO, solar cycle, and aerosols basis functions to the signal are presented in Fig. 5. An examination of the regression fit coefficients and their respective standard deviations indicates that only the aerosols basis function makes a statistically significant contribution to the FTIR and SAOZ signals. The fact that QBO and solar cycle do not contribute

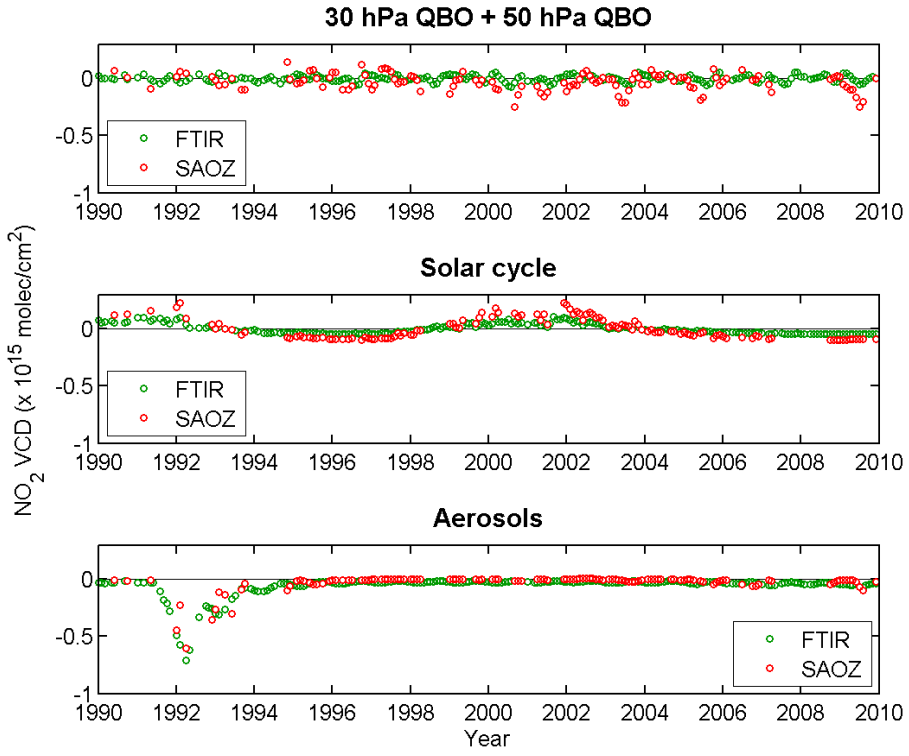

Fig. 5. Contributions of the QBO (upper plot), solar cycle (middle plot), and aerosols (lower plot) basis functions to the FTIR and SAOZ signals.

significantly is consistent with what Dirksen et al. (2011) found using OMI data at 50° N. We find also that the contributions of the QBO and solar cycle basis functions are larger for the SAOZ time series than for the FTIR time series. Sensitivity tests show that this results from the greater number of gaps in the SAOZ data set. The above mentioned trend values are significant at the 95 % confidence level. The uncertainty on the fit coefficients is based on the premise that the fit residuals are normally distributed. Figure 6 shows that this assumption is justified for both FTIR and SAOZ with fit residuals randomly scattered around zero and normally distributed.

A similar trend analysis is performed for the 1996–2009 period using ground-based SAOZ, FTIR, and satellite nadir data sets (see Fig. 7). For SAOZ, the trend is estimated using two data sets corresponding to the twilight NO_2 columns converted daily to the mean SZA of the FTIR and satellite nadir observations, respectively. Declines in NO_2 are seen consistently across all data sets, viz.: -3.6 ± 2.2 % decade^{-1} for satellites, -2.4 ± 1.1 % decade^{-1} for SAOZ at satellite SZA, -4.3 ± 1.4 % decade^{-1} for FTIR, and -2.7 ± 1.2 % decade^{-1} for SAOZ at FTIR SZA. It should be noted that the trend value estimated from the satellite data is not statistically significant at the 95 % confidence level. The uncertainty on the fit coefficients for the QBO, solar cycle, and aerosols basis functions indicates that none of these forcing mechanisms make a statistically significant contribution to the NO_2 time series measured by satellite, SAOZ, and FTIR for the 1996–2009 period.

All trend analysis results are summarized in Table 1. A good agreement is found between SAOZ, FTIR, and satellite nadir observations with a decline in the stratospheric NO_2 column reaching 3 % decade^{-1} for both the 1990–2009 and 1996–2009 periods. This decrease is not consistent with the increase in N_2O of about +2.5 % decade^{-1} reported globally (WMO, 2007) and in particular from FTIR observations at the Jungfraujoch station (Angelbratt et al., 2011). Since in the NO_y chemistry, N_2O is the source of NO_y and then NO_y is subsequently partitioned into family members, opposite NO_2 and N_2O trends suggest a change in the NO_y partitioning. In the second part of this section, we discuss plausible explanations for the observed decline of NO_2 related or not to a NO_y partitioning change.

First, $ClONO_2$ and HNO_3, which are two major NO_y species (Brohede et al., 2008) and important chlorine and hydrogen reservoirs in the stratosphere, can be useful indicators of the abundance of NO_2. They are formed by the following termolecular reactions:

$$ClO + NO_2 + M \rightarrow ClONO_2 + M \quad \text{(R2)}$$

$$OH + NO_2 + M \rightarrow HNO_3 + M \quad \text{(R3)}$$

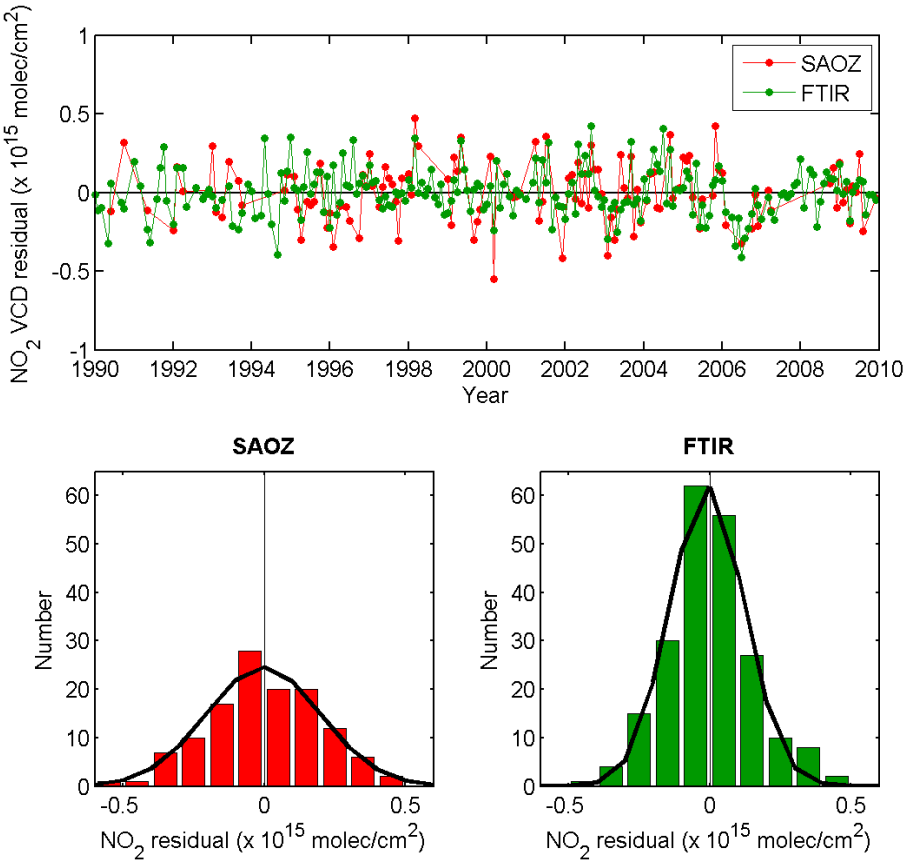

Fig. 6. SAOZ and FTIR fit residuals (upper plot) and their distributions (lower plots). Black lines correspond to Gaussian functions fitted on residuals distribution.

Table 1. Trend values in % decade^{-1} derived from FTIR, SAOZ, and satellite NO_2 column data sets for the 1990–2009 and 1996–2009 periods. t_B values appear between brackets.

	1990–2009 (% decade^{-1})	1996–2009 (% decade^{-1})
FTIR	-3.6 ± 0.9 (4.0)	-4.3 ± 1.4 (3.1)
SAOZ at FTIR SZA	-3.7 ± 1.1 (3.4)	-2.7 ± 1.2 (2.3)
Satellites	–	-3.6 ± 2.2 (1.6)
SAOZ at satellite SZA	–	-2.4 ± 1.1 (2.2)

The main loss reactions for these species are photolysis, which releases NO_2, as well as reactions with OH (for HNO_3) and dissociation on aerosols and ice particles (for $ClONO_2$). HNO_3 and $ClONO_2$ have been measured routinely at the Jungfraujoch station since the early 1980s using the FTIR technique (Rinsland et al., 2003b; Vigouroux et al., 2007; Wolff et al., 2008; Kohlhepp et al., 2011). This permits a trend analysis over the same time periods as was done for NO_2. Trend values are derived by applying the least squares regression model, described in Sect. 4.1, to the FTIR $ClONO_2$ and HNO_3 total column time series. Results are presented in Fig. 8. For $ClONO_2$, negative trends of -5.8 ± 1.0 % decade^{-1} and -8.2 ± 1.4 % decade^{-1} are found for the 1990–2009 and 1996–2009 periods, respectively. The latter value is more negative by about 3 % decade^{-1} with respect to the trend in total tropospheric chlorine of -6.0 ± 0.5 % decade^{-1} observed over the same 1996–2009 period (WMO, 2011a). In the light of Reaction (R2), this larger decline of $ClONO_2$ is consistent with a decrease of stratospheric NO_2 of about 3 % decade^{-1} as observed since 1996 from SAOZ, FTIR, and satellite nadir NO_2 data sets, suggesting that NO_2 could control the trend of $ClONO_2$ together with total chlorine. Moreover, chlorine may also play an important role in the partitioning of NO_x into NO and NO_2 through the following reaction (Crutzen, 1979):

$$ClO + NO \rightarrow Cl + NO_2 \quad \text{(R4)}$$

Given Reaction (R4), if ClO would be decreasing, more NO_x could stay in the NO form.

For HNO_3, positive trends of $+1.0 \pm 0.8$ % decade^{-1} and $+1.9 \pm 1.2$ % decade^{-1} are found for the 1990–2009 and 1996–2009 periods, respectively (see Fig. 8). Even if not statistically significant at the 95 % confidence level, this

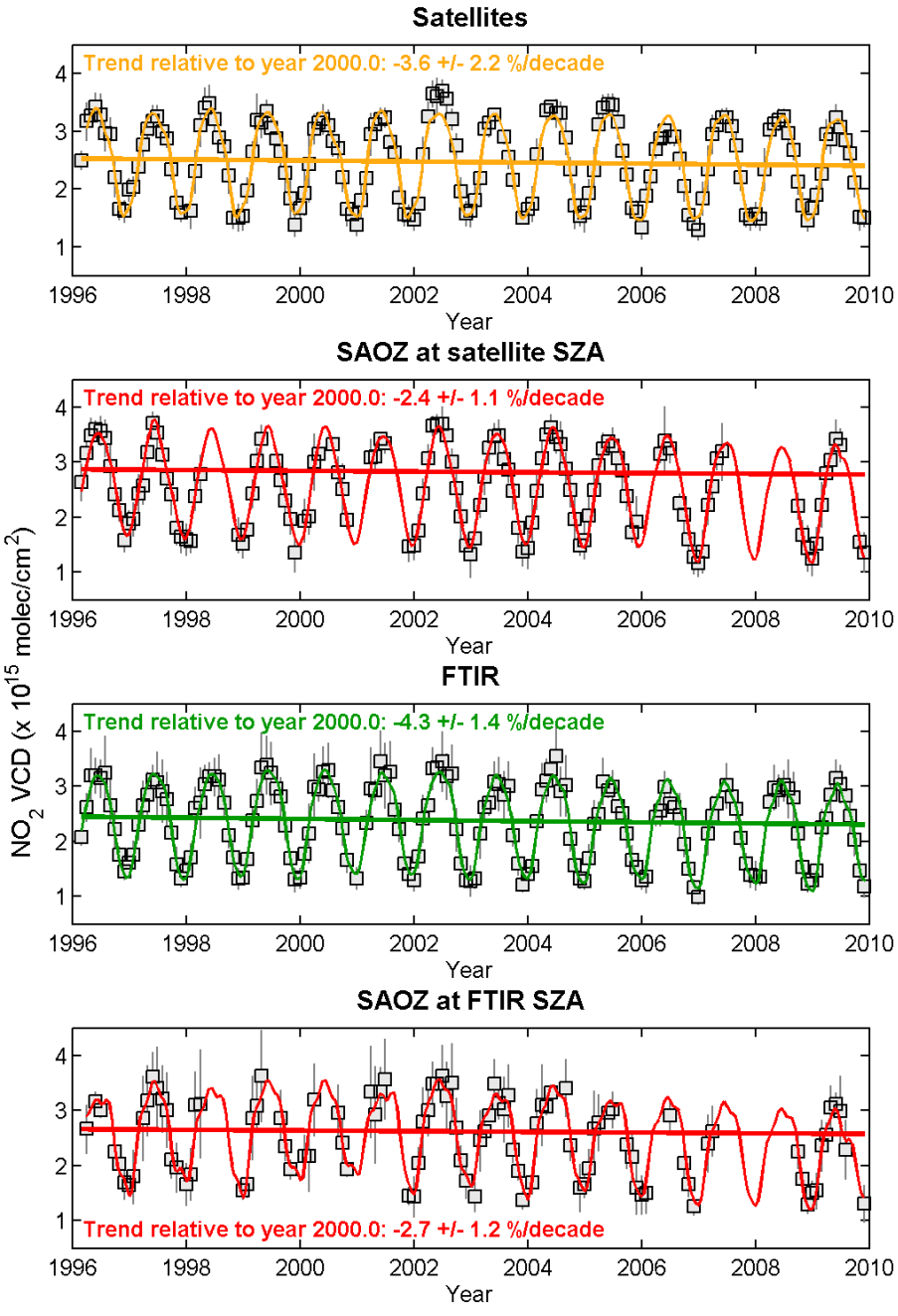

Fig. 7. Results of the trend analysis over the 1996–2009 period using the satellites, SAOZ, and FTIR monthly mean NO_2 vertical column densities (VCD; grey squares). Twilight SAOZ columns are photochemically converted to the mean SZAs of the FTIR and satellite measurements. Colored lines correspond to the linear trend (thick line) and to the NO_2 columns recalculated using the multiple linear regression model (thin line). The error bars correspond to 1-sigma standard deviation.

increase in HNO_3 is not surprising and not necessarily inconsistent with the observed decline of NO_2: HNO_3 being the most abundant NO_y species in terms of column, an increase of N_2O should result in a positive trend in NO_y and therefore in HNO_3.

As discussed in the introduction, ozone can also influence the abundance of NO_2 in the stratosphere: a decrease in ozone leads to an increase in NO_2 and vice versa through Reaction (R1). We have inferred the trend in the ozone column at Jungfraujoch by applying our least squares regression model to two total ozone column data sets. The first one is based on measurements from the Dobson spectrophotometer instrument No. 101 operating at Arosa (46.8° N, 9.7° E), close to the Jungfraujoch station. The second data set

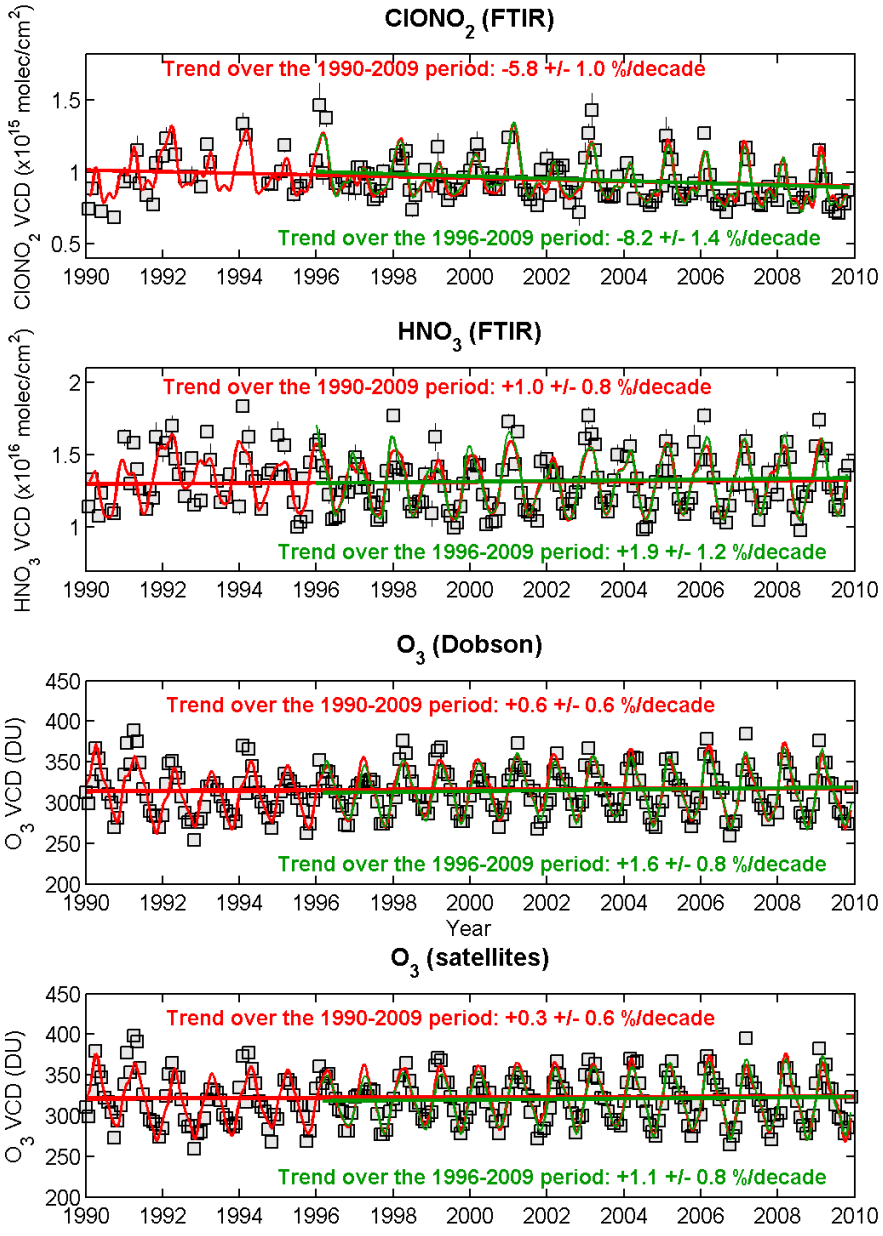

Fig. 8. Results of the trend analysis of the $ClONO_2$, HNO_3, and O_3 total columns measured above Jungfraujoch (above the Arosa station for Dobson measurements). Trend values are relative to year 2000.

combines satellite-based measurements from TOMS (Total Ozone Mapping Spectrometer), SBUV (Solar Backscattered Ultra-Violet), and OMI (Ozone Monitoring Instrument), and GOME instruments (Bodeker et al., 2005). A very good consistency is obtained between Dobson and satellite trend values (see Fig. 8): $+0.6 \pm 0.6\,\%\,\text{decade}^{-1}$ (Dobson) and $+0.3 \pm 0.6\,\%\,\text{decade}^{-1}$ (satellite) for 1990–2009 and $+1.6 \pm 0.8\,\%\,\text{decade}^{-1}$ (Dobson) and $+1.1 \pm 0.8\,\%\,\text{decade}^{-1}$ (satellite) for 1996–2009. It should be noted that the two latter values are also reasonably consistent with the O_3 trend of $+0.6 \pm 0.9\,\%\,\text{decade}^{-1}$ estimated from FTIR observations at Jungfraujoch during the 1996–2009 period (Vigouroux et al., 2008; WMO, 2011b). Given the Reaction (R1), these slight increases in ozone could at least partly contribute to the observed negative trend in NO_2, even if not statistically significant at the 95 % confidence level.

A change in the Dobson–Brewer circulation could also affect the evolution of stratospheric NO_2 (Fish et al., 2000). Cook and Roscoe (2009) recently reported a small, though not significant, increase in the stratospheric circulation of $+1.4 \pm 3.5\,\%\,\text{decade}^{-1}$ derived from SAOZ NO_2

observations in Antarctic summer. A strengthening speed up of the Dobson-Brewer circulation would lead to less time in the stratosphere for the conversion of N_2O to reactive nitrogen, resulting in a downwards trend of the NO_2 vertical column.

Finally, Revell et al. (2012) recently investigated the links between N_2O and NO_x concentrations using chemistry-climate model simulations in order to study the past and future effectiveness of N_2O in depleting stratospheric ozone. Their findings are consistent with our observations at Jungfraujoch: they showed that the NO_2/NO partitioning is currently changing with time to favor NO, due to stratospheric cooling, which slows the $NO + O_3 \rightarrow NO_2 + O_2$ reaction, and decreasing ClO concentrations, which slows the $NO + ClO \rightarrow NO_2 + Cl$ reaction. It should be noted that a stratospheric cooling can also decrease the amount of NO_y in the stratosphere from N_2O (Rosenfield and Douglass, 1998).

5 Summary and conclusions

We have presented consolidated time series of stratospheric NO_2 vertical columns at the NDACC station of Jungfraujoch retrieved from ground-based FTIR and SAOZ observations as well as from GOME, SCIAMACHY, and GOME-2 satellite nadir measurements. The time period covered by the FTIR and SAOZ observations is 1990–2009 while combining the three satellite data sets covers the 1996–2009 period. We have first performed a cross-verification of the different data sets through the comparison of FTIR and SAOZ NO_2 columns on one hand, and the comparison between satellite nadir and SAOZ observations on the other hand. FTIR NO_2 columns agree well with SAOZ columns with a bias of -7.8 ± 8.2 % on average over the 1990–2009 period. A good agreement is also found between satellite nadir and SAOZ data sets with mean relative differences of $+0.9 \pm 8.8$ % (GOME), $+1.9 \pm 11.5$ % (SCIAMACHY), and $+2.3 \pm 11.6$ % (GOME-2). It should be noted that it is the first time that stratospheric NO_2 products from these satellite nadir instruments are validated for such an extended period.

The trend of the stratospheric NO_2 column has been estimated by applying a least squares regression model to the different ground-based and satellite data sets. For the analysis of trends in satellite observations, a composite data set covering the period 1996–2009 was constructed based on the comparison between the satellite and SAOZ measurements. A good consistency is found between the trends based on satellite and SAOZ measurements i.e. -3.6 ± 2.2 % decade^{-1} for satellite and -2.4 ± 1.1 % decade^{-1} for SAOZ. Similar trend values are obtained for the 1990–2009 period using SAOZ and FTIR observations (-3.7 ± 1.1 % decade^{-1} and -3.6 ± 0.9 % decade^{-1}, respectively). This decline of stratospheric NO_2 of about 3 % decade^{-1}, obtained from three independent measurement techniques, provides further evidence that, at least for northern mid-latitudes, the trend in stratospheric NO_2 does not necessarily reflect the evolution of N_2O, considered as the main source of NO_x in the stratosphere. The most reasonable explanation for this feature is a change in the NO_x partitioning in favor of NO, due to possible stratospheric cooling (not investigated here) and the decline of chlorine content in the stratosphere, the latter being further confirmed by the observed decrease in $ClONO_2$ at the Jungfraujoch station. Since previous studies have shown that ozone can affect significantly the trend in NO_2, we have derived the trend of this species at Jungfraujoch using ground- and satellite-based O_3 measurements. The slightly positive trends obtained for the 1990–2009 and 1996–2009 periods are consistent with a decrease of NO_2 through the $NO_2 + O_3 \rightarrow NO_3 + O_2$ reaction. Although not investigated here, possible changes in the strength of the stratospheric circulation could also contribute to the negative trend in stratospheric NO_2. A strengthening of the Brewer-Dobson circulation would allow less time in the stratosphere for the conversion of N_2O into reactive nitrogen, and therefore would lead to a decrease in stratospheric NO_2. We can also not rule out an altitude dependence of the trends, i.e. different trends for NO_2 and N_2O since concentration profiles of both species have their maxima in the stratosphere at different altitudes (around 27–30 km and close to the tropopause, respectively).

Model-based sensitivity studies would certainly augment the interpretation of our findings, as well as similar trend analyses at other locations using FTIR, UV-visible, and satellite observations. However, these are beyond the scope of the present paper. This work also suggests that more effort should be put into consolidating the different ground-based and satellite observational data sets, which is one of the major tasks of the NDACC.

Acknowledgements. This research was financially supported at IASB-BIRA by the Belgian Federal Science Policy Office, Brussels (PRODEX contract A3C) and by the EU 7th Framework Programme projects SHIVA (contract 226224) and NORS (contract 284421). The University of Liège contribution was primarily supported by the Belgian Federal Science Policy Office, Brussels, through the SECPEA, A3C and AGACC-II projects. Emmanuel Mahieu is Research Associate with the F.R.S. – FNRS. We further acknowledge the contributions of the F.R.S. – FNRS and of the Fédération Wallonie-Bruxelles for funding the development of the Jungfraujoch laboratory and for supporting travel costs to the station, respectively. We thank the International Foundation High Altitude Research Stations Jungfraujoch and Gornergrat (HFSJG, Bern) for supporting the facilities needed to perform the observations. We are grateful to the many Belgian colleagues who have performed the FTIR observations used here. Work at the Eindhoven University of Technology was funded by the Netherlands Organisation for Scientific Research, NOW Vidi grant 864.09.001. GOME-2 level-1 data are provided by EUMETSAT. The SLIMCAT modeling was supported by the EU GEOmon project and NERC.

Edited by: T. Wagner

References

Angelbratt, J., Mellqvist, J., Blumenstock, T., Borsdorff, T., Brohede, S., Duchatelet, P., Forster, F., Hase, F., Mahieu, E., Murtagh, D., Petersen, A. K., Schneider, M., Sussmann, R., and Urban, J.: A new method to detect long term trends of methane (CH_4) and nitrous oxide (N_2O) total columns measured within the NDACC ground-based high resolution solar FTIR network, Atmos. Chem. Phys., 11, 6167–6183, doi:10.5194/acp-11-6167-2011, 2011.

Bodeker, G. E., Boyd, I. S., and Matthews, W. A.: Trends and variability in vertical ozone and temperature profiles measured by ozonesondes at Lauder, New Zealand: 1986–1996, J. Geophys. Res., 103, 28661–28681, 1998.

Bodeker, G. E., Shiona, H., and Eskes, H.: Indicators of Antarctic ozone depletion, Atmos. Chem. Phys., 5, 2603–2615, doi:10.5194/acp-5-2603-2005, 2005.

Boersma, K. F., Eskes, H. J., and Brinksma, E. J.: Error analysis for tropospheric NO_2 retrieval from space, J. Geophys. Res., 109, D04311, doi:10.1029/2003JD003962, 2004.

Boersma, K. F., Eskes, H. J., Veefkind, J. P., Brinksma, E. J., van der A, R. J., Sneep, M., van den Oord, G. H. J., Levelt, P. F., Stammes, P., Gleason, J. F., and Bucsela, E. J.: Near-real time retrieval of tropospheric NO_2 from OMI, Atmos. Chem. Phys., 7, 2103–2118, doi:10.5194/acp-7-2103-2007, 2007.

Brohede, S., McLinden, C. A., Urban, J., Haley, C. S., Jonsson, A. I., and Murtagh, D.: Odin stratospheric proxy NO_y measurements and climatology, Atmos. Chem. Phys., 8, 5731–5754, doi:10.5194/acp-8-5731-2008, 2008.

Chang, L., Palo, S., Hagan, M., Richter, J., Garcia, R., Riggin, D., and Frittz, D.: Structure of the migrating diurnal tide in the whole atmosphere community climate model, Adv. Space Res., 41, 1398–1407, 2008.

Chipperfield, M. P.: New version of the TOMCAT/SLIMCAT offline chemical transport model: intercomparison of stratospheric tracer experiments, Q. J. Roy. Meteor. Soc., 132, 1179–1203, doi:10.1256/qj.05.51, 2006.

Cook, P. A. and Roscoe, H. K.: Variability and trends in stratospheric NO_2 in Antarctic summer, and implications for stratospheric NO_y, Atmos. Chem. Phys., 9, 3601–3612, doi:10.5194/acp-9-3601-2009, 2009.

Crutzen, P. J.: The role of NO and NO_2 in the chemistry of the troposphere and stratosphere, Annual Review of Earth and Planetary Sciences, vol. 7 (A79-37176 15-42), Annual Reviews, Inc., Palo Alto, California, USA, 443–472, 1979.

Dirksen, R. J., Boersma, K. F., Eskes, H. J., Ionov, D. V., Bucsela, E. J., Levelt, P. F., and Kelder, H. M.: Evaluation of stratospheric NO_2 retrieved from the ozone monitoring instrument: intercomparison, diurnal cycle, and trending, J. Geophys. Res., 116, D08305, doi:10.129/2010JD014943, 2011.

Fish, D. J., Roscoe, H. K., and Johnston, P. V.: Possible causes of stratospheric NO_2 trend observed at Lauder, New Zealand, Geophys. Res. Lett., 27, 3313–3316, 2000.

Gil, M., Yela, M., Gunn, L. N., Richter, A., Alonso, I., Chipperfield, M. P., Cuevas, E., Iglesias, J., Navarro, M., Puentedura, O., and Rodriguez, S.: NO_2 climatology in the northern subtropical region: diurnal, seasonal and interannual variability, Atmos. Chem. Phys., 8, 1635–1648, doi:10.5194/acp-8-1635-2008, 2008.

Grainger, J. and Ring, J.: Anomalous Fraunhofer line profiles, Nature, 193, p. 762, 1962.

Gruzdev, A. N.: Latitudinal structure of variations and trends in stratospheric NO_2, Int. J. Remote Sens., 30, 4227–4246, 2009.

Hendrick, F., Barret, B., Van Roozendael, M., Boesch, H., Butz, A., De Mazière, M., Goutail, F., Hermans, C., Lambert, J.-C., Pfeilsticker, K., and Pommereau, J.-P.: Retrieval of nitrogen dioxide stratospheric profiles from ground-based zenith-sky UV-visible observations: validation of the technique through correlative comparisons, Atmos. Chem. Phys., 4, 2091–2106, doi:10.5194/acp-4-2091-2004, 2004.

Hendrick, F., Van Roozendael, M., Kylling, A., Petritoli, A., Rozanov, A., Sanghavi, S., Schofield, R., von Friedeburg, C., Wagner, T., Wittrock, F., Fonteyn, D., and De Mazière, M.: Intercomparison exercise between different radiative transfer models used for the interpretation of ground-based zenith-sky and multi-axis DOAS observations, Atmos. Chem. Phys., 6, 93–108, doi:10.5194/acp-6-93-2006, 2006.

Hendrick, F., Johnston, P. V., Kreher, K., Hermans, C., De Mazière, M., and Van Roozendael, M.: One decade trend analysis of stratospheric BrO over Harestua (60° N) and Lauder (45° S) reveals a decline, Geophys. Res. Lett., 35, L14801, doi:10.1029/2008GL034154, 2008.

Kohlhepp, R., Ruhnke, R., Chipperfield, M. P., De Mazière, M., Notholt, J., Barthlott, S., Batchelor, R. L., Blatherwick, R. D., Blumenstock, Th., Coffey, M. T., Demoulin, P., Fast, H., Feng, W., Goldman, A., Griffith, D. W. T., Hamann, K., Hannigan, J. W., Hase, F., Jones, N. B., Kagawa, A., Kaiser, I., Kasai, Y., Kirner, O., Kouker, W., Lindenmaier, R., Mahieu, E., Mittermeier, R. L., Monge-Sanz, B., Morino, I., Murata, I., Nakajima, H., Palm, M., Paton-Walsh, C., Raffalski, U., Reddmann, Th., Rettinger, M., Rinsland, C. P., Rozanov, E., Schneider, M., Senten, C., Servais, C., Sinnhuber, B.-M., Smale, D., Strong, K., Sussmann, R., Taylor, J. R., Vanhaelewyn, G., Warneke, T., Whaley, C., Wiehle, M., and Wood, S. W.: Observed and simulated time evolution of HCl, $ClONO_2$, and HF total column abundances, Atmos. Chem. Phys., 12, 3527–3556, doi:10.5194/acp-12-3527-2012, 2012.

Liley, J. B., Johnston, P. V., McKenzie, R. L., Thomas, A. J., and Boyd, I. S.: Stratospheric NO_2 variations from a long time series at Lauder, New Zealand, J. Geophys. Res., 105, 11633–11640, 2000.

McLinden, C. A., Olsen, S. C., and Prather, M. J.: Understanding trends in stratospheric NO_y and NO_2, J. Geophys. Res., 106, 27787–27793, 2001.

Platt, U. and Stuz, J.: Differential Optical Absorption Spectroscopy (DOAS), Principles and Applications, ISBN 978-3-540-21193-8, Springer, Berlin, Heidelberg, Germany, 2008.

Pommereau, J.-P. and Goutail, F.: O_3 and NO_2 ground-based measurements by visible spectrometry during arctic winter and spring 1988, Geophys. Res. Lett., 15, 891–894, 1988.

Pougatchev, N. S. and Rinsland, C. P.: Spectroscopic study of the seasonal variation of carbon monoxide vertical distribution above Kitt Peak, J. Geophys. Res., 100, 1409–1416, 1995.

Revell, L. E., Bodeker, G. E., Smale, D., Lehmann, R., Huck, P. E., Williamson, B. E., Rozanov, E., and Struthers, H.: The effectiveness of N_2O in depleting stratospheric ozone, Geophys. Res.

Lett., 39, L15806, doi:10.1029/2012GL052143, 2012.

Rinsland, C. P., Weisenstein, D. K., Ko, M. K. W., Scott, C. J., Chiou, L. S., Mahieu, E., Zander, R., and Demoulin, P.: Post Mount Pinatubo eruption ground-based stratospheric column measurements of HNO_3, NO, and NO_2 and their comparison with model calculation, J. Geophys. Res., 108, 4437, doi:10.1029/2002JD002965, 2003a.

Rinsland, C. P., Mahieu, E., Zander, R., Jones, N. B., Chipperfield, M. P., Goldman, A., Anderson, J., Russell III, J. M., Demoulin, P., Notholt, J., Toon, G. C., Blavier, J.-F., Sen, B., Sussmann, R., Wood, S. W., Meier, A., Griffith, D. W. T., Chiou, L. S., Murcray, F. J., Stephen, T. M., Hase, F., Mikuteit, S., Schulz, A., and Blumenstock, T.: Long-term trends of inorganic chlorine from ground-based infrared solar spectra: past increases and evidence for stabilization, J. Geophys. Res., 108, 4252, doi:10.1029/2002JD003001, 2003b.

Rosenfield, J. E. and Douglass, A. R.: Doubled CO_2 effects on NO_y in a coupled 2-D model, Geophys. Res. Lett., 25, 4381–4384, 1998.

Rothman, L. S., Jacquemart, D., Barbe, A., Chris Benner, D. Birk, M., Brown, L. R., Carleer, M. R., Chackerian Jr., C., Chance, K., Coudert, L. H., Dana, V., Devi, V. M., Gamache, R. R., Goldman, A., Jucks, K. W., Maki, A. G., Massie, S. T., Orphal, J., Perrin, A., Rinsland, C. P., Smith, M. A. H., Tennyson, J., Tolchenov, Toth, R. A., Vander Auwera, J., Varanasi, P., and Wagner, G.: The HITRAN 2004 molecular spectroscopic database, J. Quant. Spectrosc. Ra., 96, 139–204, 2005.

Santer, B. D., Wigley, T. M. L., Boyle, J. S., Gaffen, D. J., Hnilo, J. J., Nychka, D., Parker, D. E., and Taylor, K. E.: Statistical significance of trends and trend differences in layer-average atmospheric temperature time series, J. Geophys. Res., 105, 7337–7356, 2000.

Shettle, E. P.: Models of aerosols, clouds, and precipitation for atmospheric propagation studies, in: NATO AGARD Conference Proceedings No. 454: atmospheric propagation in the UV, visible, IR and mm-region and related system aspects, NATO (North Atlantic Treaty Organisation), Neuilly sur Seine, France, 1989.

Solomon, S.: Stratospheric ozone depletion: a review of concepts and history, Rev. Geophys., 37, 275–316, 1999.

Vandaele, A. C., Hermans, C., Simon, P. C., Carleer, M., Colin, R., Fally, S., Mérienne, M.-F., Jenouvrier, A., and Coquart, B.: Measurements of the NO_2 absorption cross section from 42 000 cm^{-1} to 10000 cm^{-1} (238–1000 nm) at 220 K and 294 K, J. Quant. Spectrosc. Ra., 59, 171–184, 1998.

van der A, R. J., Peters, D. H. M. U., Heskes, H., Boersma, K. F., Van Roozendael, M., De Smedt, I., and Kelder, H.: Detection of the trend and seasonal variation in tropospheric NO_2 over China, J. Geophys. Res., 111, D12317, doi:10.1029/2005JD006594, 2006.

Van Roozendael, M., De Mazière, M., and Simon, P. C.: Ground-based visible measurements at the Jungfraujoch station since 1990, J. Quant. Spectrosc. Ra., 52, 231–240, 1994.

Vernier, J.-P., Thomason, L. W., Pommereau, J.-P., Bourassa, A., Pelon, J., Garnier, A., Hauchecorne, A., Blanot, L., Trepte, C., Degenstein, D., and Vargas, F.: Major influence of tropical volcanic eruptions on the stratospheric aerosol layer during the last decade, Geophys. Res. Lett., 38, L12807, doi:10.129/2011GL047563, 2011.

Vigouroux, C., De Mazière, M., Errera, Q., Chabrillat, S., Mahieu, E., Duchatelet, P., Wood, S., Smale, D., Mikuteit, S., Blumenstock, T., Hase, F., and Jones, N.: Comparisons between ground-based FTIR and MIPAS N_2O and HNO_3 profiles before and after assimilation in BASCOE, Atmos. Chem. Phys., 7, 377–396, doi:10.5194/acp-7-377-2007, 2007.

Vigouroux, C., De Mazière, M., Demoulin, P., Servais, C., Hase, F., Blumenstock, T., Kramer, I., Schneider, M., Mellqvist, J., Strandberg, A., Velazco, V., Notholt, J., Sussmann, R., Stremme, W., Rockmann, A., Gardiner, T., Coleman, M., and Woods, P.: Evaluation of tropospheric and stratospheric ozone trends over Western Europe from ground-based FTIR network observations, Atmos. Chem. Phys., 8, 6865–6886, doi:10.5194/acp-8-6865-2008, 2008.

Weatherhead, E. C., Reinsel, G. C., Tiao, G. C., Meng, X., Choi, D., Cheang, W., Keller, T., DeLuisi, J., Wuebbles, D. J., Kerr, J. B., Miller, A. J., Oltmans, S. J., and Frederick, J. E.: Factors affecting the detection of trends: statistical considerations and applications to environmental data, J. Geophys. Res., 103, 17149–17161, 1998.

WMO (World Meteorological Organization): Scientific Assessment of Ozone depletion: 2006 (chapt. 4), Global Ozone Research and Monitoring Project, Report 50, World Meteorological Organization, Geneva, Switzerland, 2007.

WMO (World Meteorological Organization): Scientific Assessment of Ozone depletion: 2010 (chapt. 1), Global Ozone Research and Monitoring Project, Report 52, World Meteorological Organization, Geneva, Switzerland, 2011a.

WMO (World Meteorological Organization): Scientific Assessment of Ozone depletion: 2010 (chapt. 2), Global Ozone Research and Monitoring Project, Report 52, World Meteorological Organization, Geneva, Switzerland, 2011b.

Wolff, M. A., Kerzenmacher, T., Strong, K., Walker, K. A., Toohey, M., Dupuy, E., Bernath, P. F., Boone, C. D., Brohede, S., Catoire, V., von Clarmann, T., Coffey, M., Daffer, W. H., De Mazière, M., Duchatelet, P., Glatthor, N., Griffith, D. W. T., Hannigan, J., Hase, F., Höpfner, M., Huret, N., Jones, N., Jucks, K., Kagawa, A., Kasai, Y., Kramer, I., Küllmann, H., Kuttippurath, J., Mahieu, E., Manney, G., McElroy, C. T., McLinden, C., Mébarki, Y., Mikuteit, S., Murtagh, D., Piccolo, C., Raspollini, P., Ridolfi, M., Ruhnke, R., Santee, M., Senten, C., Smale, D., Tétard, C., Urban, J., and Wood, S.: Validation of HNO_3, $ClONO_2$, and N_2O_5 from the Atmospheric Chemistry Experiment Fourier Transform Spectrometer (ACE-FTS), Atmos. Chem. Phys., 8, 3529–3562, doi:10.5194/acp-8-3529-2008, 2008.

Zander, R., Mahieu, E., Demoulin, P., Duchatelet, P., Roland, G., Servais, C., De Mazière, M., Reimann, S., and Rinsland, C. P.: Our changing atmosphere: evidence based on long-term infrared solar observations at the Jungfraujoch since 1950, Sci. Total Environ., 391, 184–195 doi:10.1016/j.scitotenv.2007.10.018, 2008.

Atmos. Chem. Phys., 14, 765–781, 2014
www.atmos-chem-phys.net/14/765/2014/
doi:10.5194/acp-14-765-2014

Atmospheric Chemistry and Physics Open Access

Four years of ground-based MAX-DOAS observations of HONO and NO_2 in the Beijing area

F. Hendrick[1], J.-F. Müller[1], K. Clémer[1,*], P. Wang[2], M. De Mazière[1], C. Fayt[1], C. Gielen[1], C. Hermans[1], J. Z. Ma[3], G. Pinardi[1], T. Stavrakou[1], T. Vlemmix[1,4], and M. Van Roozendael[1]

[1]Belgian Institute for Space Aeronomy (BIRA-IASB), Brussels, Belgium
[2]Institute of Atmospheric Physics, Chinese Academy of Science, Beijing, China
[3]Chinese Academy of Meteorological Sciences, Beijing, China
[4]Delft University of Technology (TU-Delft), Delft, the Netherlands
[*]now at: Instituut voor Sterrenkunde, Katholieke Universiteit Leuven, Leuven, Belgium

Correspondence to: F. Hendrick (franch@oma.be)

Received: 26 March 2013 – Published in Atmos. Chem. Phys. Discuss.: 22 April 2013
Revised: 12 December 2013 – Accepted: 13 December 2013 – Published: 22 January 2014

Abstract. Ground-based Multi-Axis Differential Optical Absorption Spectroscopy (MAX-DOAS) measurements of nitrous acid (HONO) and its precursor NO_2 (nitrogen dioxide) as well as aerosols have been performed daily in Beijing city centre (39.98° N, 116.38° E) from July 2008 to April 2009 and at the suburban site of Xianghe (39.75° N, 116.96° E) located ∼ 60 km east of Beijing from March 2010 to December 2012. This extensive dataset allowed for the first time the investigation of the seasonal cycle of HONO as well as its diurnal variation in and in the vicinity of a megacity. Our study was focused on the HONO and NO_2 near-surface concentrations (0–200 m layer) and total vertical column densities (VCDs) and also aerosol optical depths (AODs) and extinction coefficients retrieved by applying the Optimal Estimation Method to the MAX-DOAS observations. Monthly averaged HONO near-surface concentrations at local noon display a strong seasonal cycle with a maximum in late fall/winter (∼ 0.8 and 0.7 ppb at Beijing and Xianghe, respectively) and a minimum in summer (∼ 0.1 ppb at Beijing and 0.03 ppb at Xianghe). The seasonal cycles of HONO and NO_2 appear to be highly correlated, with correlation coefficients in the 0.7–0.9 and 0.5–0.8 ranges at Beijing and Xianghe, respectively. The stronger correlation of HONO with NO_2 and also with aerosols observed in Beijing suggests possibly larger role of NO_2 conversion into HONO in the Beijing city center than at Xianghe. The observed diurnal cycle of HONO near-surface concentration shows a maximum in the early morning (about 1 ppb at both sites) likely resulting from night-time accumulation, followed by a decrease to values of about 0.1–0.4 ppb around local noon. The HONO / NO_2 ratio shows a similar pattern with a maximum in the early morning (values up to 0.08) and a decrease to ∼ 0.01–0.02 around local noon. The seasonal and diurnal cycles of the HONO near-surface concentration are found to be similar in shape and in relative amplitude to the corresponding cycles of the HONO total VCD and are therefore likely driven mainly by the balance between HONO sources and the photolytic sink, whereas dilution effects appear to play only a minor role. The estimation of OH radical production from HONO and O_3 photolysis based on retrieved HONO near-surface concentrations and calculated photolysis rates indicate that in the 0–200 m altitude range, HONO is by far the largest source of OH radicals in winter as well as in the early morning at all seasons, while the contribution of O_3 dominates in summer from mid-morning until mid-afternoon.

1 Introduction

Since the late 1970s, nitrous acid (HONO) has been identified as a key chemical species in the troposphere, especially through its photolysis which leads to the formation of the hydroxyl radical OH (Perner and Platt, 1979). OH is known as the major oxidant (“detergent”) of the atmosphere responsible for the degradation of most pollutants. It contributes also to the formation of ozone and PANs (peroxyacyl nitrates)

causing the so-called "photochemical smog" in polluted regions, as well as to the formation of aerosol particles from the oxidation of volatile organic compounds (VOCs). The photochemistry of HONO has been and is still extensively discussed in the literature (see e.g., Sörgel et al., 2011a; Li et al., 2012; Elshorbany et al., 2012). The heterogeneous conversion of nitrogen dioxide (NO_2) on wet organic and inorganic ground surfaces (soil, buildings, vegetation, and aerosols) is believed to be a major source of HONO, and very probably its main source during the night (Wojtal et al., 2011 and references therein):

$$2NO_2 + H_2O + \text{surface} \rightarrow HONO + HNO_3 \quad \text{(R1)}$$

Recent field studies and laboratory measurements have identified other heterogeneous daytime sources like photosensitized reduction of NO_2 on organic surfaces (George et al., 2005; Stemmler et al., 2006) and the photolysis of adsorbed nitric acid/nitrate at UV wavelengths (Zhou et al., 2003). Su et al. (2011) also showed that soil, through nitrite-producing microbes, can release important HONO amounts. Other HONO sources are direct emissions from combustion processes and the following gas-phase reaction:

$$NO + OH + M \rightarrow HONO + M \quad \text{(R2)}$$

Reaction (R2) operates only during daytime, when the OH and NO concentrations are high. HONO sinks include dry deposition during nighttime, and photolysis (Reaction R3) during daytime, at a rate close to $10^{-3}\,s^{-1}$ around noon (see Sect. 3.3):

$$HONO + h\nu(\lambda < 400\,\text{nm}) \rightarrow OH + NO \quad \text{(R3)}$$

$$HONO + OH \rightarrow H_2O + NO_2 \quad \text{(R4)}$$

The reaction of HONO with OH (Reaction R4) is comparatively very slow. The rapid photolysis of HONO accumulated during the night is the main source of OH radicals in early morning when other radical sources, i.e. the photolysis of ozone and carbonyls, are still weak. It should be noted that recent measurements in the Los Angeles Basin have suggested that nitryl chloride ($ClNO_2$) can be, together with HONO, an important source of radicals in the morning in urban environments (Young et al., 2012). This study also showed that vertical gradients of radical precursors should be taken into account in radical budgets, especially in case of HONO.

Despite the numerous field campaigns and laboratory experiments conducted during the last three decades, the main HONO formation mechanisms are still not fully characterised, and their relative contributions to the observed HONO concentrations are not well quantified. Model simulations accounting only for anthropogenic emissions and the known gas phase formation through Reaction (R2) generally largely underestimate the measured daytime HONO levels, with possibly important consequences for the prediction of oxidants (OH, O_3, PANs) (e.g., Kleffmann et al., 2005; Sörgel et al., 2011b). Consequently, the largely unknown HONO daytime source can have a significant impact on air quality and chemistry-climate modeling (Elshorbany et al., 2012 and references therein).

So far, HONO has been measured mainly using the long-path DOAS (Differential Optical Absorption Spectroscopy) and in-situ LOPAP-like (Long-Path Absorption Photometer) techniques. LOPAP is a wet chemical technique based on the dissolution of HONO in the liquid phase as nitrite (NO_2^-) followed by its detection as an azo dye (compound bearing the $R-N=N-R'$ functional group) with a long-path absorption photometer (Heland et al., 2001; Kleffmann et al., 2002). The LOPAP instruments can generally be operated only for a limited period of time, from a few weeks to a couple of months, due to instrumental and logistics issues. Long-path DOAS is an active (i.e. using an artificial light source) DOAS technique consisting of the measurement of the trace gas concentration integrated along a light path of several hundred metres to a few kilometres between the light source and the spectrometer (Hönninger et al., 2004; Platt and Stutz, 2008). The first detection of HONO by long-path DOAS was made over the Los Angeles air basin in the late 1970s (Perner and Platt, 1979). Both long-path DOAS and LOPAP show a high sensitivity to HONO and have the advantage to be independent of daylight, enabling nighttime measurements.

Here we present four years of ground-based Multi-Axis (MAX-) DOAS observations of HONO and its main precursor NO_2 and aerosols in the Beijing area from July 2008 till December 2012. It is the first time that measurements of HONO in or in the vicinity of a megacity are reported over such a long time period, allowing investigation of the seasonal variation of this species in urban conditions. MAX-DOAS is a passive DOAS technique based on measurements of scattered sunlight at zenith and at different elevation angles towards the horizon (the so-called off-axis geometry), increasing therefore the sensitivity to absorbers present close to the ground compared to the zenith scattered sunlight technique (Hönninger et al., 2004; Platt and Stutz, 2008). Due to the use of daylight and the need to minimise the contribution of the stratosphere for absorbers with strong stratospheric concentration like NO_2 here, our MAX-DOAS observations are performed from $\sim 85°$ SZA (solar zenith angle) sunrise to 85° SZA sunset with a time resolution of ~ 15 min (time needed for a complete MAX-DOAS scan). The instrumental set up including data transfer is fully automated, allowing continuous daily operation throughout the year. Moreover, by applying appropriate inversion methods like the Optimal Estimation (OEM; Rodgers, 2000), some information on the vertical distribution of the target trace gases can be retrieved in addition to the vertical column density (e.g., Hendrick et al., 2004; Hönninger et al., 2004; Wittrock et al., 2004; Friess et al., 2006; Clémer et al., 2010; Vlemmix et al., 2011). It should be noted that altitude-resolved measurements of trace gases are also possible with long-path DOAS

or in-situ techniques, generally with a better vertical resolution and signal-to-noise ratio than MAX-DOAS, but these require more sophisticated instrumental set up like, for example, placing retro-reflectors or in-situ instruments on different floors of a building (e.g. Stutz et al., 2002; Wang et al., 2006; Wong et al., 2012; Villena et al., 2011).

In the present study, MAX-DOAS observations of HONO, NO_2, and aerosols have been performed from July 2008 to April 2009 in the Beijing city centre (39.98° N, 116.38° E) and from March 2010 until December 2012 at the suburban site of Xianghe (39.75° N, 116.96° E) located ∼ 60 km east of Beijing. From these datasets, the diurnal and seasonal variations of the HONO and NO_2 vertical column densities (VCDs) and near-surface concentrations and aerosol optical depths (AODs) in the Beijing area are investigated. The OH production from HONO is also estimated based on the retrieved HONO concentrations and calculated photolysis rates. In Sect. 2, the MAX-DOAS measurements of HONO, NO_2, and aerosols are introduced, including a description of the instrumental set up, DOAS analysis settings, and vertical profile retrievals. HONO, NO_2, and AOD retrievals have been also verified through comparisons with correlative data. Section 3 presents the results: the seasonal variation of daytime HONO and NO_2 VCDs and near-surface concentrations and AODs, their diurnal variation and an estimation of the OH production from HONO and ozone. Concluding remarks are given in the last section.

2 MAX-DOAS measurements

2.1 Instrumental set up

The MAX-DOAS instrument used in this study has been extensively described in Clémer et al. (2010). It is a dual-channel system composed of two grating spectrometers covering the UV and visible wavelength ranges (300–390 nm and 400–720 nm, respectively). The output of both spectrometers is connected to cooled CCD detectors. The spectrometers and detectors are mounted inside a thermo-regulated box in order to minimise thermal stress on optical and mechanical parts. The instrument function is close to a Gaussian with a full width at half maximum (FWHM) of 0.4 nm and 0.9 nm for the UV and visible channels, respectively. Scattered light is collected at various elevation and azimuth angles by an optical head mounted on a commercial sun tracker (INTRA, Brusag) and the light is guided to the two spectrometers through optical fibres.

The instrument, which was designed and assembled at BIRA-IASB in Brussels, was installed during the July 2008–April 2009 period on the roof of the Institute of Atmospheric Physics (IAP) of the Chinese Academy of Sciences located in the Beijing city centre (39.98° N, 116.38° E). Then, it was moved to the suburban site of Xianghe (39.75° N, 116.96° E) located about 60 km east of Beijing where it has been operating continuously from March 2010 until now. At both locations, the azimuthal scan option was not activated and the telescope points towards a fixed azimuth direction (north). A full MAX-DOAS scan requires ∼ 15 min and comprises the following 9 elevation angles: 2°, 4°, 6°, 8°, 10°, 12°, 15°, 30°, and 90° (zenith).

2.2 DOAS analysis

The measured scattered light spectra are analysed using the spectral fitting software suite QDOAS developed at BIRA-IASB (http://uv-vis.aeronomie.be/software/QDOAS/). The principle of the DOAS technique is to separate the absorption of molecular species which usually display narrow features from a broadband background resulting mainly from Mie and Rayleigh scattering and instrumental effects (Platt and Stutz, 2008). The direct product of the DOAS spectral fitting method is the differential slant column density (DSCD) which is the concentration of a given absorber integrated along the effective light path relative to the amount of the same absorber in a measured reference spectrum. For profile retrieval in the troposphere, it is a common way to select the zenith measurement of a MAX-DOAS scan as the reference for the off-axis DSCDs of the same scan in order to minimise the stratospheric signal (Clémer et al., 2010; Peters et al., 2012). This is particularly important for NO_2 which displays a significant concentration in the stratosphere.

HONO DSCDs are retrieved in the 337–375 nm wavelength range, taking into account the spectral signature of NO_2 at 220 and 296 K (Vandaele et al., 1998), O_3 at 218 and 243 K (Brion et al., 2004), O_4 (Hermans et al., 2003), BrO at 223 K (Fleischmann et al., 2004), HCHO at 293 K (Meller and Moortgat, 2000), and the filling-in of the solar Fraunhofer bands by the Ring effect (Grainger and Ring, 1962). The HONO absorption cross-sections at 296 K are obtained from Stutz et al. (2000). A fifth-order polynomial is used to fit the low frequency spectral structure due to molecular and Mie scattering. An example of DOAS fit for HONO is presented in Fig. 1.

In the case of NO_2, the 425–490 nm fitting window is used and, in addition to the NO_2 cross-sections at 220 and 296 K (Vandaele et al., 1998), the following trace gas cross-sections are taken into account in the DOAS analysis: O_3 at 241 K (Burrows et al., 1999), O_4 (Hermans et al., 2003), and H_2O (Harder and Brault, 1997). A Ring spectrum and a third-order polynomial closure term are also included. An example of DOAS fit for NO_2 is also shown in Fig. 1.

The O_4 DSCDs needed for the aerosol extinction profile retrieval (see Sect. 2.3) are retrieved in the UV and visible regions (338–370 nm and 425–490 nm, respectively) using the O_4 cross-sections from Hermans et al. (2003). The other DOAS settings are described in Clémer et al. (2010).

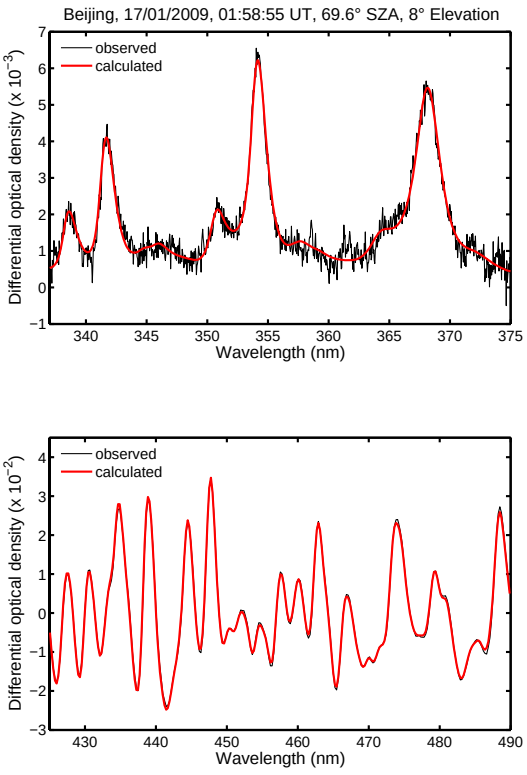

Fig. 1. Example of DOAS fit for HONO (upper plot) and NO_2 (lower plot) at Beijing. Similar DOAS fit results are obtained at Xianghe.

2.3 HONO, NO_2, and aerosol profile retrievals

HONO and NO_2 vertical profiles can be retrieved for each MAX-DOAS scan by applying an inversion algorithm to the corresponding sets of DSCDs measured at the different elevation angles. This profiling technique is based on the fact that the mean scattering height rises into the atmosphere with the increase of the elevation angle and probes the layers where the tropospheric absorber is present. So, each measured DSCD of a MAX-DOAS scan is representative of the absorber concentration in a given altitude range and therefore the observed DSCD variation as a function of the elevation angle depends on the vertical distribution of the absorber. In this study, we used the bePRO inversion algorithm developed at BIRA-IASB (Clémer et al., 2010). It is based on the Optimal Estimation Method (OEM; Rodgers, 2000) and uses a two-step approach. First, the aerosol extinction vertical profiles are retrieved separately at 360 and 477 nm for each MAX-DOAS scan from the corresponding measured O_4 DSCDs. The principle of this retrieval is the following: since the O_4 vertical profile is well-known and nearly constant (it varies with the square of the O_2 monomer concentration), O_4 DSCD measurements can provide information on the vertical distribution of aerosols (Wagner et al., 2004; Friess et al., 2006). This first step is required since the light path length through the atmosphere (and thus the measured HONO or NO_2 DSCD) strongly depends on the aerosols and therefore a good estimate of the vertical distribution of the aerosols is needed to perform accurate HONO and NO_2 profile retrievals. Further details regarding our aerosol retrieval (aerosol optical depth (AOD) and extinction coefficient), including the corresponding bePRO settings, are extensively described in Clémer et al. (2010). The only difference with the latter study is the use of two separate wavelengths (360 nm and 477 nm) instead of four (360, 477, 577, and 630 nm). In the second step, the bePRO algorithm is applied to the measured HONO and NO_2 DSCDs in order to retrieve vertical profiles of these trace gas species. In the OEM, the weighting function matrix ($\mathbf{K}$) and the a priori profile $\boldsymbol{x}_a$ are two important retrieval parameters. $\mathbf{K}$ expresses the sensitivity of the measurements (DSCDs) to changes in the trace gas profile and it is calculated using the linearized discrete ordinate radiative transfer model (LIDORT; Spurr, 2008) as forward model. This code includes an analytical calculation of the weighting functions allowing for near real time automated retrievals without the need of pre-calculated look-up tables. Since the present retrieval problem is ill-conditioned (no unique solution for the trace gas or aerosol extinction vertical profile due to the too small information content of fitted DSCDs from one MAX-DOAS scan), a priori constraints are needed to reject unrealistic solutions and to stabilise the inversion. For HONO and NO_2 vertical profile retrievals, exponentially decreasing a priori profiles have been used with a fixed scaling height of 0.5 km according to the following expression:

$$\boldsymbol{x}_a(z) = \frac{\mathrm{VCD}_a}{\mathrm{SH}} e^{-\frac{z}{\mathrm{SH}}} \quad (1)$$

where $\boldsymbol{x}_a(z)$ is the a priori profile (HONO or NO_2 concentration as a function of the altitude z), SH is the scaling height (fixed to 0.5 km) and VCD_a is the a priori vertical column density of HONO or NO_2. For each scan, VCD_a is derived using the geometrical approximation, i.e. the HONO or NO_2 layer is assumed to be located below the scattering altitude at 30° Elevation, so that tropospheric HONO or NO_2 VCDs can be derived by applying a geometrical AMF to measured DSCDs at 30° Elevation (Hönninger et al., 2004; Brinksma et al., 2008).

The other important retrieval parameter settings, which are the a priori and measurement uncertainty covariance matrices ($\mathbf{S}_a$ and $\mathbf{S}_\varepsilon$, respectively), have been constructed as in Clémer et al. (2010). Profile retrievals have been performed at the following wavelengths: 354 nm for HONO and 460 nm for NO_2. The pressure and temperature profiles were taken from the US Standard Atmosphere and the retrieval grid was chosen as in Clémer et al. (2010): ten layers of 200 m thickness between 0 and 2 km, two layers of 500 m between 2 and 3 km and 1 layer between 3 and 4 km.

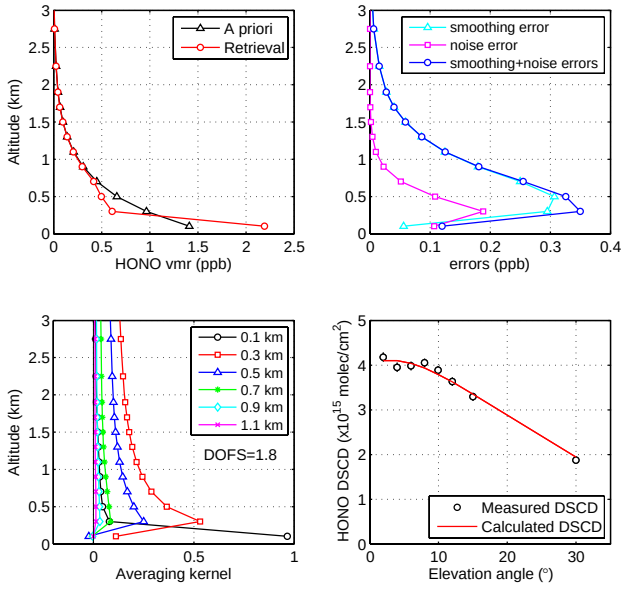

Fig. 2. Example of HONO vertical profile retrieval (Beijing, 21 January 2009, ∼10:15 local time). The upper plots display the a priori and retrieved profiles (left) and the smoothing and noise errors (right). Averaging kernels and fit results (comparison between measured DSCDs and those calculated with the retrieved profile) are shown in the lower plots. Error bars on the measured DSCDs are the DOAS fit errors.

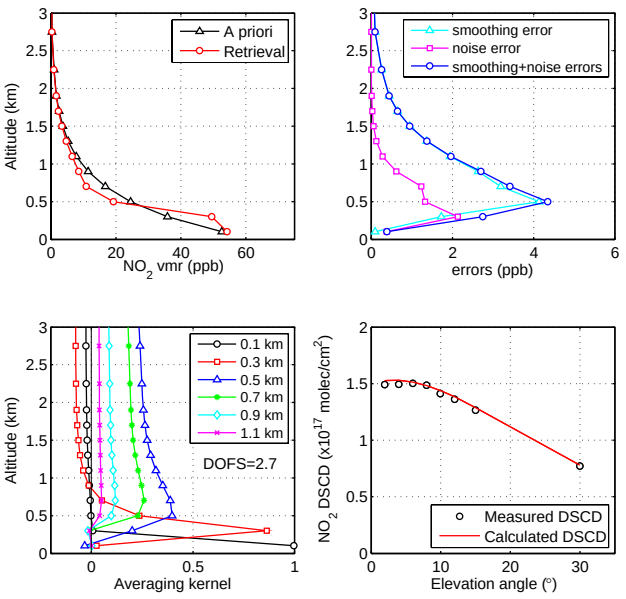

Fig. 3. Same as Fig. 2 but for NO_2.

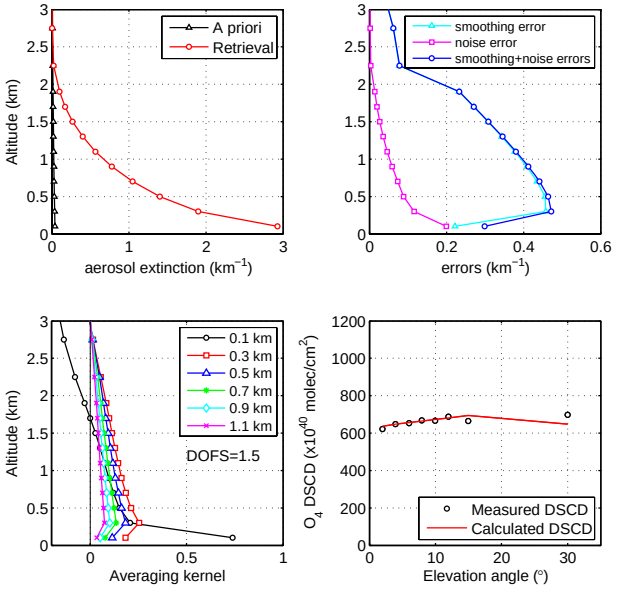

Fig. 4. Same as Figs. 2 and 3 but for aerosol extinction vertical profile retrieved from O_4 DSCDs at 360 nm.

Examples of HONO, NO_2, and aerosol extinction coefficient profile retrievals for winter conditions are presented in Figs. 2, 3, and 4, respectively. The examination of the averaging kernels, which give information on the sensitivity of the retrievals to the vertical distribution, shows that the HONO and aerosols inversions are mostly sensitive close to the surface (0–200 m layer) and to the overhead column above 200 m. In the case of NO_2, three layers can be distinguished: 0–200 m, 200–400 m, and the column above 400 m. It should be noted that a similar vertical sensitivity is obtained for summer conditions. Since our study is mainly focused on HONO, we decided to investigate the HONO and NO_2 concentrations in the 0–200 m layer as well as the vertical column densities of these species. The retrieval of both columns and near-surface concentrations is the main strength of the MAX-DOAS technique: it helps to distinguish between photochemical and vertical transport influences on the diurnal cycle of HONO and NO_2 given that columns are less sensitive than concentrations to the growth of the boundary layer. Regarding the information content, it should be noted that the number of independent pieces of information, also called degrees of freedom for signal (DOFS) and given by the trace of the matrix **A** (Rodgers, 2000), is generally larger for NO_2 than for HONO (2.7 and 1.8 in the examples shown in Figs. 2 and 3). This is due to the fact that the NO_2 absorption strength is larger by more than one order of magnitude than the HONO one, leading to a significantly higher sensitivity of the MAX-DOAS observations to NO_2.

From the error budgets presented in Figs. 2, 3, and 4, the contribution of the smoothing error, which represents the difference between the retrieved profile and the true profile due to vertical smoothing by the retrieval algorithm (Rodgers, 2000), is seen to be significantly larger than the noise (DOAS fit) error, except in the lowest layers. The sum of smoothing and noise errors on the HONO volume mixing ratio (VMR)

Table 1. Error budget of the retrieved HONO and NO_2 near-surface (0–200 m) concentrations and vertical column densities (VCD). The total uncertainty is calculated by adding the different error terms in Gaussian quadrature.

	Beijing				Xianghe			
	0–200 m		VCD		0–200 m		VCD	
	HONO	NO_2	HONO	NO_2	HONO	NO_2	HONO	NO_2
Smoothing + noise errors (%)	19	4	8	3	23	8	10	3
Uncertainty related to the aerosol retrieval (%)	18	21	7	5	21	25	8	6
Uncertainty related to the a priori (%)	7	10	20	10	11	14	23	10
Uncertainty on HONO or NO_2 cross sections (%)	5	3	5	3	5	3	5	3
Total uncertainty (%)	28	24	23	12	33	30	27	12

in the 0–200 m layer and on the HONO vertical columns amount on average to 19 % and 8 %, respectively at Beijing and to 23 % and 10 % at Xianghe. The corresponding values for NO_2 are 4 % and 3 %, respectively at Beijing and 8 % and 3 % at Xianghe. One of the main forward model error sources in HONO and NO_2 profile retrievals is the uncertainty on the retrieved aerosol extinction profiles in step 1. If we combine the smoothing and noise errors on the retrieved aerosol vertical profile (see Fig. 4) to a systematic error of 20 % on O_4 DSCDs (Clémer et al., 2010; Wagner et al., 2009), the corresponding impacts on the HONO and NO_2 retrievals are in the 18–25 % and 5–8 % ranges for surface concentrations and VCDs, respectively. The uncertainty related to the choice of the a priori profile for the HONO and NO_2 retrievals has been estimated by varying the scaling height (SH; see Eq. 1) defining the a priori profile, more precisely, by adopting a value of either 0.5 km (standard retrieval) or 1 km. At Beijing, using a SH value of 1 km instead of 0.5 km leads to the following average changes on the retrieved quantities: -7 and $+10$ % on the HONO and NO_2 near-surface concentrations, respectively, and $+20$ and $+10$ % on the HONO and NO_2 vertical columns, respectively. The corresponding changes for Xianghe are $+11$ and $+14$ % (HONO and NO_2 near-surface concentrations) and $+23$ and $+10$ % (HONO and NO_2 vertical columns). Total uncertainties are estimated by combining the above error sources to the systematic uncertainty on the HONO and NO_2 cross-sections (5 % and 3 %, respectively, according to Stutz et al., 2000 and Vandaele et al., 1998). The error budget on HONO and NO_2 near-surface concentrations and vertical column densities is presented in Table 1.

It is known that clouds and aerosols might bias the MAX-DOAS trace gas retrieval (Wagner et al., 2004; Friess et al., 2006). Instead of explicitly applying a could filtering approach, HONO, NO_2, and aerosol profile retrievals have been quality-checked for each MAX-DOAS scan by comparing the measured DSCDs to those calculated using the retrieved profiles (see examples of retrieval fit results in Figs. 2, 3, and 4 for HONO, NO_2, and aerosols, respectively). In practice, the selection of good profile retrievals is based on the following criteria: (1) residual (RMS) of the retrieval fit smaller than an empirically derived threshold value (3.5×10^{14} molec cm^{-2} for HONO and 2.4×10^{16} molec cm^{-2} for NO_2), (2) DOFS larger than 0.7 meaning that the information comes mainly from the measurements and not from the a priori profile, (3) scans with bad O_4 fit results (RMS of the fit larger than 30 % of the mean O_4 DSCD of the scan), which can be obtained, e.g. for changing aerosol loading or/and cloud conditions during a scan, are rejected, and (4) scans with very large AOD values (> 6) are also rejected given the significantly larger uncertainties on the trace gas retrievals in such conditions. Using these four criteria, about 35 % of the scans are rejected at both stations.

2.4 Verification of the HONO, NO_2 and aerosol retrievals

The NO_2 and aerosol retrievals have been evaluated through comparison with correlative observations. In the case of NO_2, the VCDs retrieved in the Beijing city centre have been compared to MAX-DOAS measurements performed by Ma et al. (2013) at the China Meteorological Administration (39.95° N, 116.32° E) located at about 10 km southwest of the Institute of Atmospheric Physics where our MAX-DOAS spectrometer was installed. It is important to note that both instruments were pointing towards the same direction (North) and that Ma et al. (2013) have used the simple geometrical approximation to derive the NO_2 VCDs (no Optimal Estimation step such as in the present study). Figure 5 shows the comparison of seasonally averaged diurnal variations of the tropospheric NO_2 VCDs for the period August 2008 to April 2009. As can be seen, a very good agreement is obtained, with both MAX-DOAS datasets displaying very similar diurnal variation in both shape and absolute values. In fall and summer, however, our retrieved VCDs are notably noisier than in Ma et al. (2013). It is likely related to the smaller number of available retrievals during these seasons, due to the more strict scan selection criteria imposed in the OEM-based method (see Sect. 2.3) compared to the Ma et al. (2013) approach. Regarding aerosols, AODs at 360 nm retrieved at Beijing and Xianghe have been compared to correlative data from co-located CIMEL sunphotometers of to the AERONET network (http://aeronet.gsfc.nasa.gov). As

Table 2. Compilation of existing daytime (±3 h around local noon) HONO surface concentration measurements performed in or in the vicinity of big cities in East Asia. Beijing and Xianghe values correspond to the present study while other data are taken from Li et al. (2012; see also references therein). PRD is for Pearl River Delta region.

Location	Daytime HONO surface concentration (ppb)
	Spring/summer
Xianghe (China)	0.15
Beijing (China)	0.17
Yufa (China)	0.43
Backgarden (PRD, China)	0.24
Guangzhou (PRD, China)	2.00
Seoul (Korea)	0.36
	Fall/winter
Xianghe (China)	0.40
Beijing (China)	0.55
Shanghai (China)	0.35
Xinken (PRD, China)	0.80
Tokyo (Japan)	0.05

shown in Fig. 6, a good consistency is found between MAX-DOAS and CIMEL instruments at both sites, with correlation coefficients and slopes very close to 1, in agreement with Clémer et al. (2010). These results indicate that the first step of our OEM-based trace gas retrieval, i.e. the aerosol profiling, is robust and reliable.

A thorough validation of HONO retrievals such as those carried out for NO_2 and aerosols is currently not possible due to the lack of correlative datasets at both stations. However, as in Li et al. (2012), MAX-DOAS HONO surface concentrations have been compared to other existing measurements made in or in the vicinity of big cities in East Asia. As can be seen in Table 2, Beijing and Xianghe values are at the low end of existing measurements in spring/summer while they are comprised between the concentrations measured at Shanghai and Xinken (Pearl River Delta region) data in fall/winter. These results show that our MAX-DOAS HONO retrievals at Beijing and Xianghe are reasonably consistent with other existing measurements in East Asia, giving us confidence on the reliability of our HONO datasets. This compilation of HONO measurements also further confirms that the Pearl River Delta region is among the most important HONO hot spots in the world.

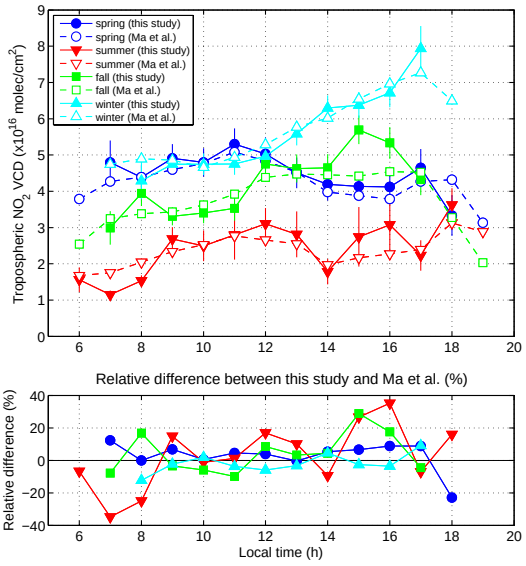

Fig. 5. Comparison of seasonally averaged tropospheric NO_2 VCD diurnal variations from MAX-DOAS measurements performed at the Institute of Atmospheric Physics (present study) and at the China Meteorological Administration (Ma et al., 2013) in the Beijing city centre. The period covered by the observations is August 2008–April 2009. Ma et al. (2013) is taken as reference for the calculation of relative differences. The calculated mean biases are: $+3 \pm 9$ % in spring, $+3 \pm 20$ % in summer, $+4 \pm 12$ % in fall, and -2 ± 6 % in winter.

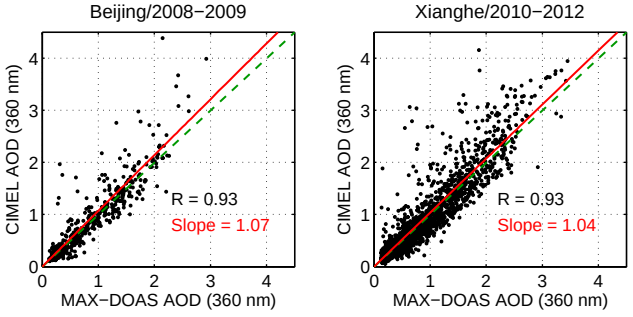

Fig. 6. Scatter plots of the AODs at 360 nm retrieved from MAX-DOAS and sunphotometer measurements at Beijing (left plot, August 2008–April 2009) and Xianghe (right plot, March 2010–December 2012). The linear regressions appear in red and the green dashed lines correspond to the 1 : 1 lines.

3 Results and discussion

3.1 Seasonal variation of daytime HONO, NO_2, and aerosols

Time-series of daytime (local noon) HONO and NO_2 surface concentration and VCD as well as AOD (360 nm) monthly means are presented in Fig. 7. A marked seasonality of the HONO surface concentration and VCD is observed at both stations, with a maximum in late fall/winter and a

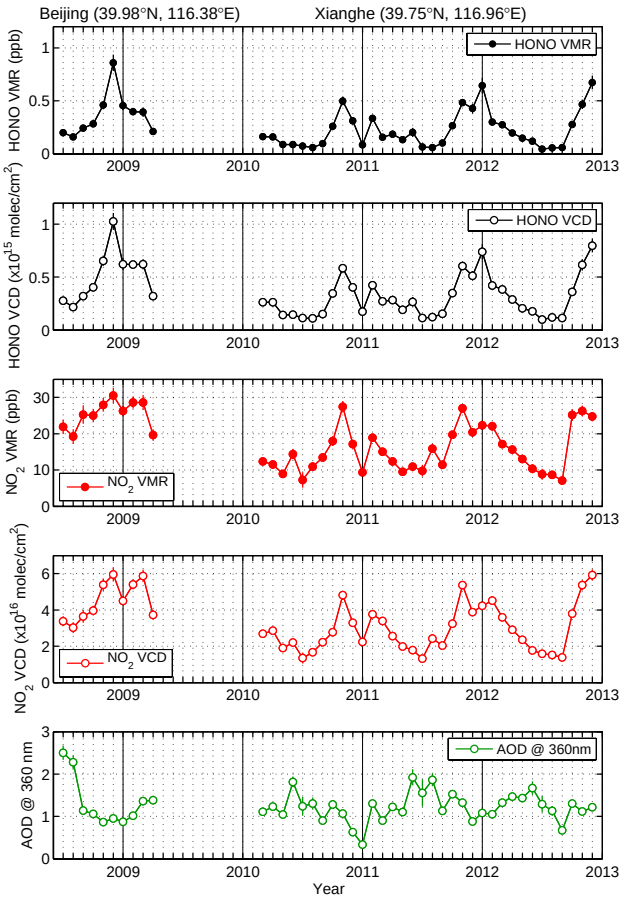

Fig. 7. Time-series of monthly averaged HONO and NO_2 near-surface concentrations (filled circles) and vertical columns (VCD; empty circles) at local noon (±2 h) at Beijing (July 2008–April 2009) and Xianghe (March 2010–December 2012). AODs at 360 nm retrieved from MAX-DOAS measurements appear in the lower plot. The error bars represent the standard deviation of the mean.

minimum in summer. The HONO surface concentration (0–200 m layer) ranges between ∼0.1 and 0.8 ppb in Beijing and between ∼0.03 and 0.7 ppb in Xianghe. These values are consistent with published daytime surface measurements of HONO performed in or in the vicinity of big cities and ranging from 0.05 to 2 ppb (Li et al., 2012), the lowest and highest values having been observed in Tokyo (Kanaya et al., 2007) and in Guangzhou City, South China (Qin et al., 2009), respectively (see also Table 2). From Fig. 7, it is found that the HONO seasonal variation follows well the seasonality of NO_2 which is believed to be its main precursor. The late fall/winter maximum is a well-known feature of NO_2 columns over industrialized areas at mid-latitudes and in particular over Northeastern China (Richter et al., 2005) and is mainly attributed to the longer photochemical lifetimes caused by the winter depletion of OH radical levels (Stavrakou et al., 2013). Domestic heating also contributes to the late fall/winter maximum, but its role is minor due to the dominance of other NO_x sources in Eastern China (Zhang et al., 2007). The HONO seasonality is the result of both enhanced production in winter (due to the NO_2 maximum) and more efficient photolysis in summer. Furthermore, the boundary layer height (BLH) is higher in summer than in winter, about 3 and 1 km in summer and winter, respectively, according to ECMWF ERA-Interim data, leading to a larger dilution of HONO in summer and therefore to lower concentrations close to the surface. This effect seems minor, however, since the seasonal cycle of HONO VCD has an only slightly lower relative amplitude (peak-to-trough ratio between 5 and 10) compared to the near-surface concentration (ratio around 10). Figure 7 also shows that the AOD has a distinct seasonality with a maximum in spring/summer and a minimum in winter. Such a seasonal variation of the AOD over Beijing was also reported by Yu et al. (2009a) using AERONET observations. It can be mainly attributed to particles emitted from massive agricultural fires in the region surrounding Beijing during the May-July period with a peak in June (Xia et al., 2013) as well as to long-range transport of dust particles during spring/summer (Yu et al., 2009a).

Related to Fig. 7, it should be also noted that the corresponding monthly mean DOFS range between 2.0 and 3.0 for NO_2, and 1.8 and 2.2 for aerosols, indicating that the retrieved surface concentration or extinction coefficient is independent from the corresponding VCD or AOD. It is also the case for HONO during the late fall/winter/early spring period with a DOFS around 1.8–2.0. In summer, the DOFS decreases to values around 1.5, suggesting that the surface concentration is to some extent not independent from the retrieved VCD and a priori profile shape. The number of days used for the calculation of monthly means exhibits a similar seasonality with a maximum in fall/winter/early spring (∼25–30 days) and a minimum in summer (∼15 days) due to the low daytime HONO amounts observed during this period making the OEM-based retrieval less stable and leading therefore to a larger number of rejected scans.

The HONO, NO_2, and aerosol seasonal variations at both stations are further illustrated in Fig. 8 where the monthly near-surface concentrations, VCDs, and AODs around local noon have been averaged over the whole measurement period. The HONO concentrations and columns are found to be generally larger at Beijing than at Xianghe, as a result of the larger NO_2 concentrations observed in the Beijing city centre (Figs. 7 and 8). The largest difference between the sites concerns the 90th percentile of HONO surface concentrations (Fig. 8) which can reach up to 2 ppb at Beijing in winter while the corresponding values do not exceed 1.25 ppb for the same period at Xianghe. The heterogeneous conversion of NO_2 into HONO appears to be very probably the dominant source of HONO at both sites and especially in Beijing, given the high correlation coefficient found between HONO and NO_2 near-surface concentrations (R_{HONO/NO_2}) and between HONO concentration and the

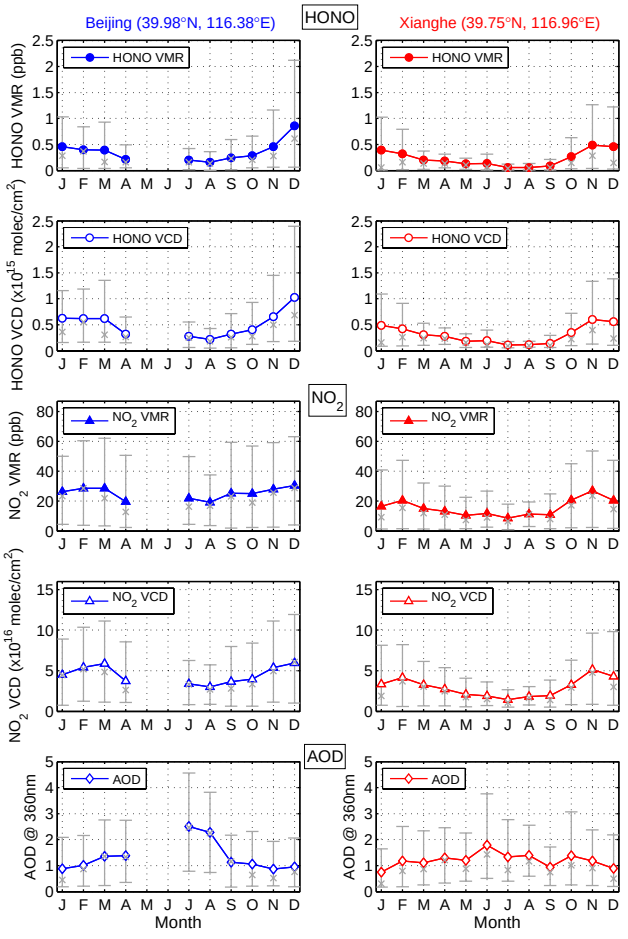

Fig. 8. Seasonal variation of the HONO and NO_2 surface concentration and vertical column density (VCD) and AOD at 360 nm at Beijing (left plots) and Xianghe (right plots). Data correspond to monthly averages over the time interval of ±2 h around local noon. The cross symbol and the lower (upper) error bars represent the median and the 10th (90th) percentiles of the data, respectively.

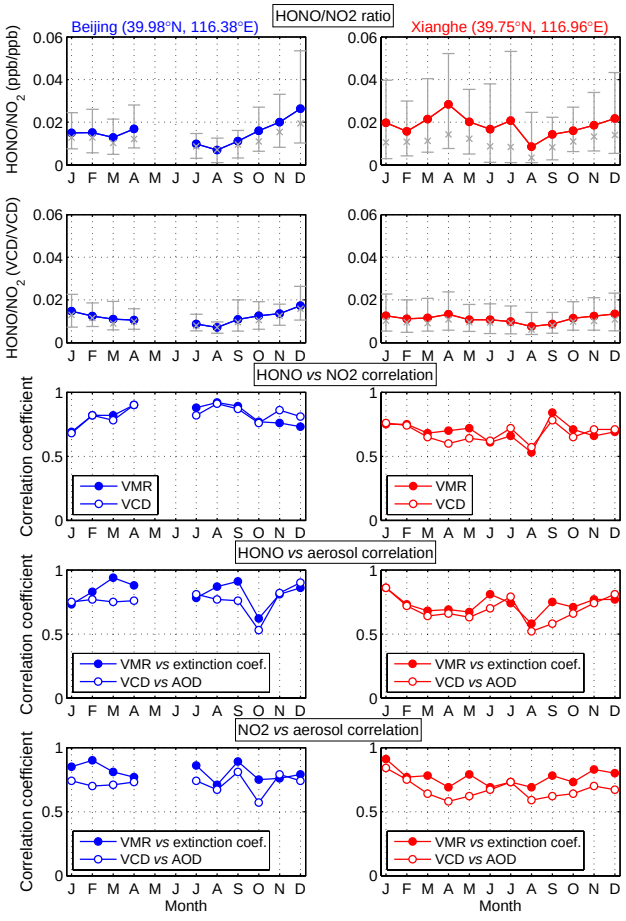

Fig. 9. Seasonal variation of the HONO to NO_2 near-surface concentration ratio, the HONO to NO_2 VCD ratio, and the HONO versus NO_2, HONO versus aerosol, and NO_2 versus aerosol correlation coefficients (0–200 m VMR and vertical column density (VCD)) at local noon at Beijing (left plots) and Xianghe (right plots). In the two upper plots, the cross symbol and the lower (upper) error bars represent the median and the 10th (90th) percentiles of the data, respectively.

aerosol extinction coefficient ($R_{HONO/AERO}$) retrieved in the 0–200 m layer. Figure 9 shows that R_{HONO/NO_2} lies in the range 0.7–0.9 at Beijing and 0.5–0.8 at Xianghe, while the corresponding $R_{HONO/AERO}$ values are comprised between 0.60 and 0.95 and between 0.55 and 0.85, respectively. It should be noted that a strong correlation is also obtained between NO_2 and aerosols in the 0–200 m layer with correlation coefficients ranging between 0.6 and 0.9 at both stations. Similar correlation coefficient values are obtained between integrated concentrations, i.e. between HONO and NO_2 VCDs, between HONO VCD and retrieved AOD, and between NO_2 VCD and retrieved AODs, suggesting that the high correlation obtained for surface concentrations is not due to changes resulting from the variation of the boundary layer height. As can be seen from Fig. 10, the high correlations found between HONO, NO_2, and aerosols are driven at both stations by day-to-day changes: within one month (summer or winter), the short-term variations of the daily means exhibit the same patterns with peaks and troughs on the same days for both trace gases and aerosols. Although a strong correlation is expected between NO_2 and HONO, since NO_2 is recognised as the main precursor of HONO, the same is not true for the correlation between NO_2 and aerosols. Therefore, the high correlation is, more than likely, mainly of meteorological origin, given the relative similarity in the spatial distribution of aerosols and NO_x, which both have a strong anthropogenic component. For HONO and aerosols, the high correlation might be further enhanced by the expected role of aerosols as mediator in the heterogeneous conversion of NO_2 to HONO. Due to the high concentrations of PM_{10} and $PM_{2.5}$ usually observed in the Beijing area, heterogeneous reactions on aerosols have been

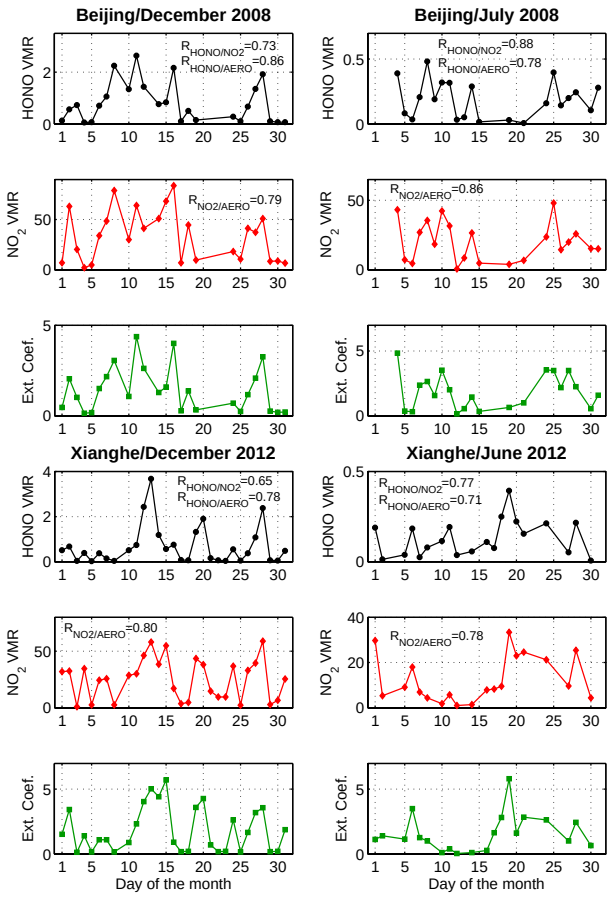

Fig. 10. Day-to-day changes of daytime HONO and NO_2 surface concentrations and aerosol extinction coefficient for one summer and one winter months at both stations. Data correspond to daily averages over the time interval of ± 2 h around local noon. Similar features are obtained for VCDs and AODs. The correlation coefficient values are also given in the figure.

estimated by Li et al. (2011) to contribute as much as $\sim 60\,\%$ to the total HONO production in the Beijing region using a model constrained by observations of HONO, O_3, PM_{10}, and $PM_{2.5}$. A significant role played by PM_{10} is further supported by the high correlation coefficients derived by Qin et al. (2009) from long-path DOAS and particulate monitor measurements in summer in the Guangzhou city, China ($R_{\mathrm{HONO/NO_2}}$ and $R_{\mathrm{HONO/PM_{10}}}$ close or larger than 0.7). In contrast, our $R_{\mathrm{HONO/NO_2}}$ and $R_{\mathrm{HONO/AERO}}$ correlation coefficients are significantly higher than those reported by Li et al. (2012) at a rural site in Southern China in summer ($R_{\mathrm{HONO/NO_2}} \sim 0.4$ and $R_{\mathrm{HONO/AERO}} \sim 0.6$), suggesting that the formation of HONO from NO_2 is more dominant in an urban environment, while other sources (e.g. soil emissions or the photolysis of nitrate and nitric acid deposited on vegetation) appear to play a larger role in rural areas.

The seasonal variation of the ratio of HONO and NO_2 concentrations (HONO / NO_2) at local noon is shown in Fig. 9, and the season-averaged concentrations, vertical columns and ratios are summarised in Tables 3 and 4. The scaling of HONO to NO_2 or NO_x is often used to make the link between HONO and its possible sources, i.e. as an indicator of the efficiency of the conversion of NO_2 into HONO (e.g. Sörgel et al., 2011a; Wojtal et al., 2011; Li et al., 2012). The HONO / NO_2 ratio values are usually sorted into the three following regimes (Wojtal et al., 2011 and references therein): direct emission (HONO / NO_2 less than 0.01) and surface sources in low and high relative humidity environments (HONO / NO_2 in the 0.01–0.03 and 0.03–0.1 ranges, respectively). It should be noted that HONO / NO_2 ratio values up to 0.30 have been derived from nighttime long-path DOAS measurements in Kathmandu, Nepal by Yu et al. (2009b) and were explained by high pollution and relative humidity and low inversion layer. The monthly averaged HONO / NO_2 ratio observed in the 0–200 m layer is comprised on average between 0.007 and 0.028 at both sites (Fig. 9). Although there are significant differences (up to a factor of 2) between the near-surface concentrations ratios observed at Beijing and Xianghe, the VCD ratios are remarkably similar at both sites, and show only little seasonal variations, with values varying between 0.008 in summer and 0.013 in fall and winter (see Table 4 and also Fig. 9). The summertime minimum is consistent with the higher photolytic sink in that season. Higher ratio values are obtained in the 0–200 m layer, by a factor ranging between 1.5 and 2, due to the shorter HONO lifetime and hence the stronger vertical gradients for HONO compared to NO_2 (see e.g. Figs. 2 and 3). Although the photolytic loss of HONO is likely an important driver of these daytime HONO / NO_2 ratios, differences between the seasonal variations of the near-surface concentration ratios at both sites are observed (see Fig. 9), suggesting that other processes can play a significant role. These could be, e.g. differences in vertical mixing or effects of horizontal transport of NO_2, especially during the winter when lifetimes are long. The 90th percentile of the monthly-averaged near-surface HONO / NO_2 ratios indicates that this ratio can reach values of up to about 0.05 at both sites (Fig. 9). The mean and 90th percentile values reported here are consistent with those measured around local noon in big cities and ranging from 0.003 to 0.075 (Li et al., 2012; Elshorbany et al., 2012, and references therein).

3.2 Diurnal variation of HONO and NO_2

Since the MAX-DOAS instrument operates continuously from about 85° SZA sunrise to 85° SZA sunset with a time resolution of ~ 15 min, the diurnal variation of HONO and NO_2 surface concentrations and VCDs can be thoroughly investigated throughout the year at both stations. Figure 11 presents the diurnal variations of HONO and NO_2 surface concentrations and HONO / NO_2 ratios (VMR / VMR) observed at Beijing and Xianghe. Measurements have been averaged per season using 1 h bins.

Table 3. Mean HONO near-surface concentration (VMR in ppb unit) and vertical column density (VCD in 10^{15} molec cm^{-2} units) around local noon (±2 h) at Beijing and Xianghe. The 10th and 90th percentiles of the data are also given.

		Beijing			Xianghe		
		HONO mean	10th perc.	90th perc.	HONO mean	10th perc.	90th perc.
Spring	VMR	0.19	0.04	0.45	0.16	0.03	0.30
	VCD	0.31	0.16	0.58	0.24	0.09	0.41
Summer	VMR	0.18	0.01	0.40	0.09	0.01	0.19
	VCD	0.25	0.05	0.49	0.15	0.06	0.28
Fall	VMR	0.46	0.05	1.14	0.38	0.03	1.01
	VCD	0.60	0.15	1.42	0.48	0.10	1.15
Winter	VMR	0.48	0.04	1.04	0.34	0.02	0.86
	VCD	0.69	0.17	1.33	0.44	0.09	0.96

Table 4. Mean HONO / NO_2 ratio (VMR / VMR and VCD / VCD) around local noon (±2 h) at Beijing and Xianghe. The 10th and 90th percentiles of the data are also given.

		Beijing			Xianghe		
		HONO / NO_2 mean	10th perc.	90th perc.	HONO / NO_2 mean	10th perc.	90th perc.
Spring	VMR	0.015	0.006	0.025	0.024	0.006	0.046
	VCD	0.010	0.006	0.015	0.012	0.006	0.021
Summer	VMR	0.008	0.002	0.013	0.017	0.004	0.035
	VCD	0.008	0.005	0.011	0.009	0.004	0.015
Fall	VMR	0.020	0.007	0.034	0.018	0.006	0.033
	VCD	0.014	0.007	0.023	0.012	0.006	0.021
Winter	VMR	0.015	0.007	0.026	0.020	0.004	0.039
	VCD	0.013	0.007	0.021	0.012	0.005	0.022

The diurnal cycle of NO_2 reflects the balance between anthropogenic emissions and photochemical sinks. In fall/winter, when photochemical activity is weak, accumulation of NO_2 results in a continuous increase of its concentrations during the day, whereas in spring/summer, the diurnal cycle is relatively flat. The diurnal cycle of the HONO concentration in the 0–200 m layer exhibits a maximum in the early morning (1.3–1.6 ppb and 0.7–1.0 ppb at Beijing and Xianghe, respectively) due to the nighttime build-up, followed by a decrease. This decrease continues throughout the day at both stations in fall/winter, while in spring/summer the HONO concentration remains relatively constant from local noon until ∼ 16:00, after which time HONO increases slightly until sunset. This diurnal cycle shape is similar to the cycle observed in several field campaigns (Qin et al., 2009; Li et al., 2012; Elshorbany et al., 2012 and references therein). The morning decrease can be attributed to the increasing HONO photolysis rates and vertical mixing, while the HONO increase in the late afternoon can be caused by the progressive absence of photolytic loss and the decrease of the boundary layer height. However, since the HONO VCD has a very similar diurnal cycle (see Fig. 12), the surface concentration variation during the day is therefore not driven by dilution effects. This is consistent with the study of Qin et al. (2009) which indicated a higher correlation between HONO and NO_2 at Guangzhou than between HONO and CO, the latter being used as a tracer for the transport processes.

As shown in Figs. 11 and 12, the HONO / NO_2 ratio (VMR / VMR and VCD / VCD) has a marked diurnal cycle at both stations with, as for HONO, a maximum in the early morning (ratio values up to ∼ 0.05–0.08 in summer) and a decrease during daytime to values around 0.01–0.02. It should be noted that this diurnal cycle, with the absence of a significant increase of the HONO / NO_2 ratio around local noon, is very similar to the one derived by Qin et al. (2009) from long-path DOAS observations in Guangzhou city.

The corresponding diurnal variations of the AOD are also presented in Fig. 12. There is no marked diurnal cycle, with values around 1–1.5 at both stations, except in Beijing in summer where the AOD increases during the morning, with a maximum value of 3 around 11:00.

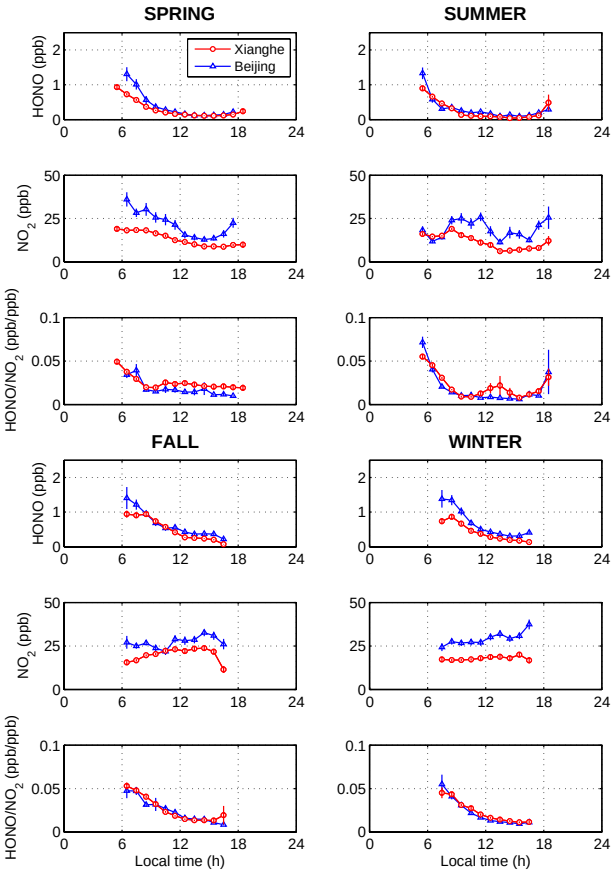

Fig. 11. Diurnal variation of the HONO and NO_2 concentrations (ppb) and their corresponding ratio in the 0–200 m layer at Beijing (blue curves) and Xianghe (red curves). Data have been averaged per season using 1 h bins. The error bars correspond to the standard deviation of the mean.

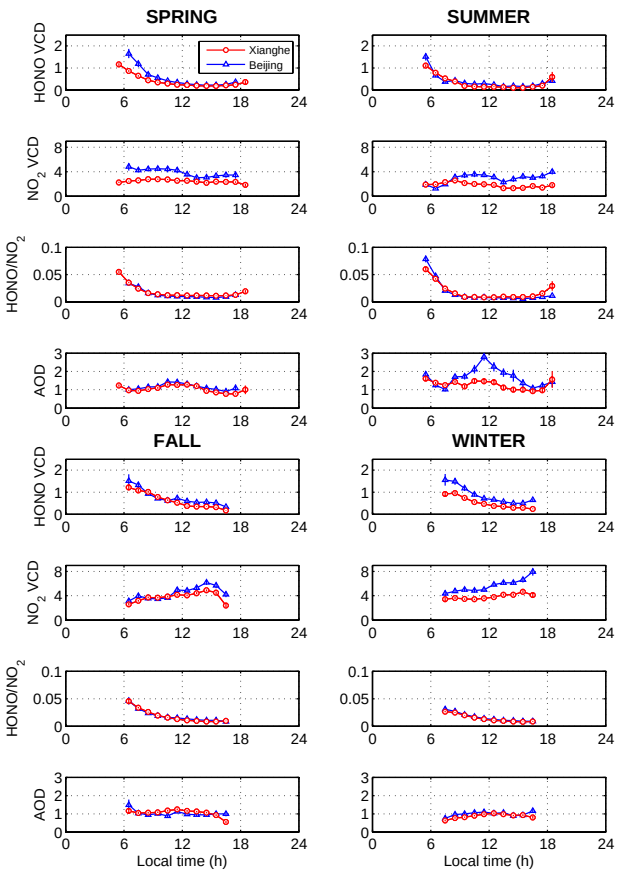

Fig. 12. Same as Fig. 11 but for the vertical column densities (VCDs) and aerosol optical depths (AODs). HONO and NO_2 VCDs are in $\times 10^{15}$ and $\times 10^{16}$ molec cm^{-2} units, respectively. The corresponding diurnal variations of the AOD are also plotted.

3.3 Estimation of OH production from HONO

In order to evaluate the importance of HONO as a source of OH radicals, especially compared to the contribution of O_3 photolysis, the OH production from HONO has been calculated in the 0–200 m layer at both stations from the retrieved HONO concentrations and simulated photolysis rates J (HONO). OH is formed from O_3 through the following reaction sequence:

$$O_3 + h\nu(\lambda < 340\,\text{nm}) \rightarrow O(^1D) + O_2 \quad \text{(R5)}$$

$$O(^1D) + H_2O \rightarrow 2OH \quad \text{(R6)}$$

The corresponding OH production has been estimated from an assumed O_3 concentration fixed to 30 ppb, water vapour concentration from ECMWF (European Centre for Medium-Range Weather Forecasts) ERA-Interim re-analysis fields (http://www.ecmwf.int/research/era/do/get/index), and simulated photolysis rate J ($O_3 \rightarrow O(^1D)$). Since the value of 30 ppb for O_3 is significantly smaller than the afternoon O_3 concentrations (up to 60 ppb) observed in summer (Lu et al., 2013; Wu et al., 2011), we tested the impact of using the diurnal cycle of O_3 measured by Chou et al. (2011) in the Beijing city centre during CAREBeijing-2006. Photolysis rates have been calculated using the TUV package including the SDISORT radiative transfer code (Madronich and Hocke, 1998). The effects of clouds are ignored, whereas attenuation by aerosols is estimated from the aerosol optical depths retrieved by MAX-DOAS at Beijing and Xianghe (see Sect. 2.3), assuming a single scattering albedo equal to 0.9 and an asymmetry parameter equal to 0.7. The albedo is set to 0.05, except over snow (0.5). Snow presence and ozone total columns are obtained from ECMWF ERA-Interim fields.

The calculated photolysis rates are presented in Fig. 13. The J (HONO) values are consistent with those measured by Li et al. (2012) in the Pearl River Delta region in Southern China, and correspond to a noon photolytic lifetime of about 15–20 min, with little differences between the seasons. The diurnal cycles of OH production due to HONO and O_3 are depicted in Fig. 14. At both stations, the OH production from HONO in the 0–200 m layer exhibits a maximum

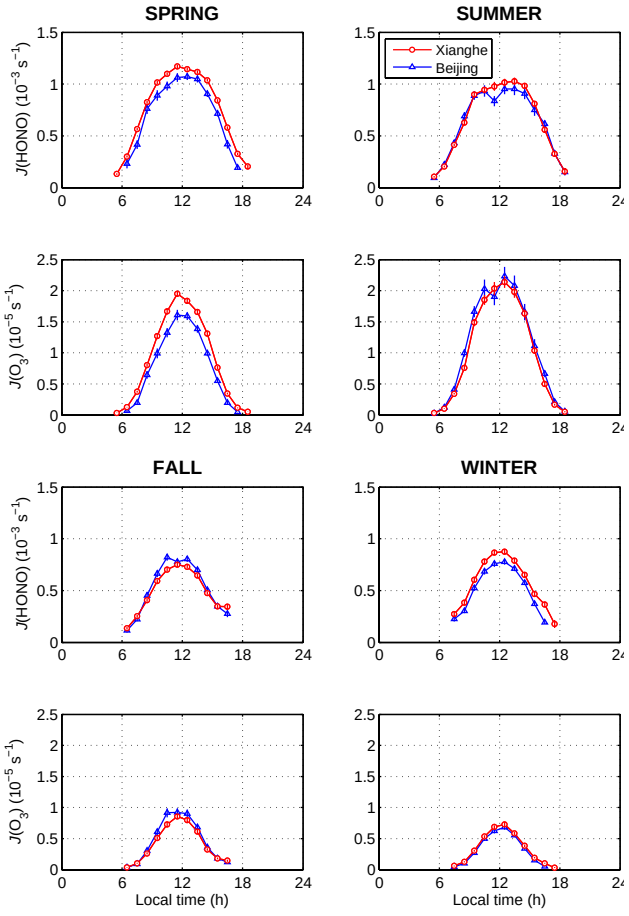

Fig. 13. Photolysis rates J (HONO) and J ($O_3 \rightarrow O(^1D)$) calculated in the 0–200 m layer for Beijing and Xianghe and averaged per season. The error bars correspond to the standard deviation of the mean.

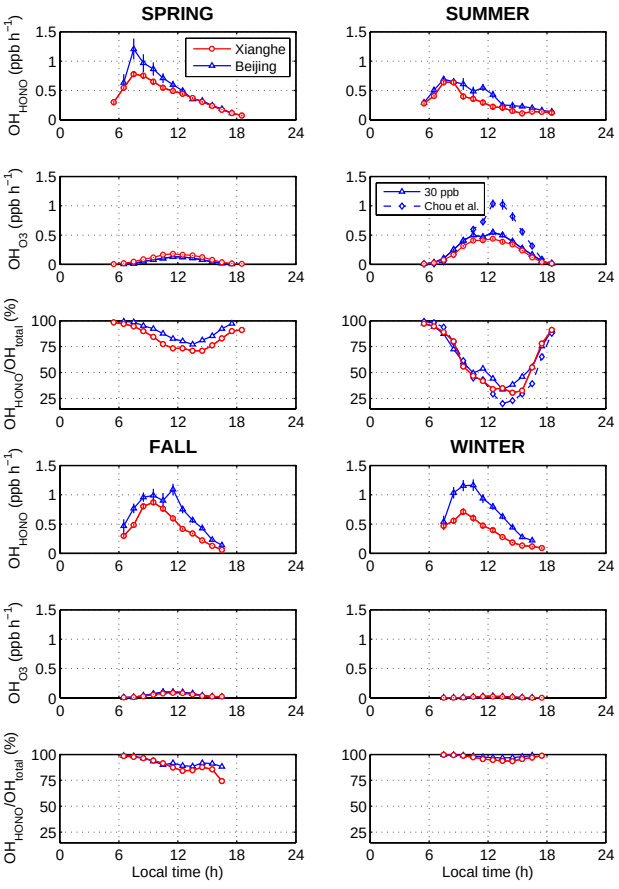

Fig. 14. Diurnal variation of the OH production from HONO (OH_{HONO}) and O_3 (OH_{O_3}) in the 0–200 m layer at Beijing (blue curves) and Xianghe (red curves). Data have been seasonally averaged using 1 h bins. The relative contribution of HONO to the OH production (OH_{HONO}/OH_{total}) is calculated as $OH_{HONO}/(OH_{HONO}+OH_{O_3})$. The error bars correspond to the standard deviation of the mean.

in the morning, between 07:00 and 09:00 in spring/summer and between 08:00 and 11:00 in fall/winter. This maximum is larger at Beijing than at Xianghe, with e.g. winter values reaching 1.2 ppb h^{-1} and 0.7 ppb h^{-1}, respectively, due to the generally larger HONO concentration observed in Beijing (Fig. 11). The shape of this diurnal cycle is similar to the one calculated by Sörgel et al. (2011b) from HONO measurements over a pine forest close to the industrial area of Huelva, southwestern Spain in fall. However, the maximum of OH production from HONO was significantly lower there ($\sim$ 0.2 ppb h^{-1}).

Comparison of the HONO and O_3 contributions to OH production reveals that HONO is the main contributor in all seasons except summer, with relative HONO contributions larger than 70 % (more than 90 % in winter) around 12:00–13:00. In summer, the contribution of O_3 dominates between 09:30 and 16:00 with a maximum of 70 % around 13:00–14:00. At Beijing, this feature is strengthened by considering the diurnal cycle of the ozone concentration measured by Chou et al. (2011) with high afternoon ozone mixing ratios, and very low values in the early morning. In that case, the contribution of O_3 to OH production reaches a maximum of 80 % in the early afternoon.

The seasonal variation of the HONO and O_3 contributions at local noon is displayed in Fig. 15. It is largely explained by the seasonal cycle of ozone photolysis rates (Fig. 13) and H_2O concentrations, which both maximise in summer. These results show that near to the ground surface in urban areas, HONO is the main source of OH radicals in winter as well as in the early morning at all seasons, in agreement with our current knowledge of the HONO photochemistry (see e.g. Li et al., 2012 and references therein).

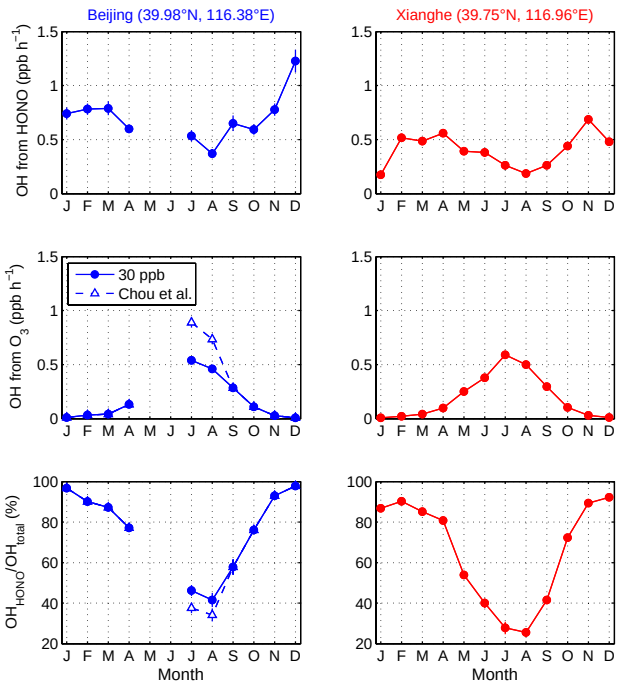

Fig. 15. Seasonal variation of the OH production from HONO (OH_{HONO}) and O_3 (OH_{O_3}) in the 0–200 m layer at Beijing (left/blue curves) and Xianghe (right/red curves) at local noon. Data correspond to monthly averages over the time interval of ±2 h around local noon. OH_{total} is equal to $OH_{HONO} + OH_{O_3}$. The error bars correspond to the standard deviation of the mean.

4 Summary and conclusions

For the first time, the seasonal variation of HONO has been investigated in and in the vicinity of a megacity. This has been achieved using MAX-DOAS observations of HONO and its main precursor NO_2 and aerosols in the Beijing city centre and at the suburban site of Xianghe located ∼ 60 km east of Beijing. The MAX-DOAS spectrometers have the advantage that they can be operated year-round during daytime in a fully automated way. Moreover, independent information on the near-surface concentration and vertical columns of trace gases can be retrieved from multiple elevation angle observations using dedicated inversion methods like the OEM used here. Our instrument was operated in the Beijing city centre from July 2008 until April 2009, and in Xianghe from March 2010 until now. The total error on retrieved near-surface concentrations and vertical columns are comprised between 23 and 33 % for HONO and between 12 and 30 % for NO_2. Retrieved NO_2 VCDs and AODs are also shown to be in good agreement with correlative measurements. In the case of HONO surface concentration, a reasonably good consistency is found between our retrievals and measurements performed in or in the vicinity of big cities in East Asia.

HONO and NO_2 concentrations retrieved at both stations around local noon in the 0–200 m layer exhibit the same marked seasonality, with a maximum in late fall/winter and a minimum in summer. The strong link between HONO and NO_2 is further supported by the high correlation of HONO with NO_2 found throughout the year, with coefficients comprised in the 0.7–0.9 and 0.5–0.8 ranges at Beijing and Xianghe, respectively. Like NO_2, HONO is more abundant at Beijing than at Xianghe, with mean VMR ranging from ∼ 0.1 to 0.8 ppb and from ∼ 0.03 to 0.7 ppb, respectively. These values are found to be consistent with previously reported daytime HONO measurements in urban conditions. A strong role of NO_2 conversion to HONO at Beijing is suggested from the higher correlation coefficients between HONO and aerosol extinctions retrieved in the 0–200 m layer at Beijing (ranging from 0.60 to 0.95 instead of 0.55 to 0.85 at Xianghe).

The diurnal profiles of HONO surface concentration and vertical column show a maximum in the early morning (1.3–1.6 ppb/1.5–1.8 × 10^{15} molec cm^{-2} in Beijing and 0.7–1.0 ppb/0.9–1.1 × 10^{15} molec cm^{-2} in Xianghe) likely explained by the photolysis of the HONO accumulated during the night. The subsequent decrease (to about 0.1–0.4 ppb for the concentration and 0.1–0.6 × 10^{15} molec cm^{-2} for the vertical column around local noon) results mostly from a balance between HONO sources and the photolytic sink. Dilution effects appear to play only a minor role, given the observed very similar diurnal cycle of the HONO vertical column, which is expected to be insensitive to vertical transport variations. The observed HONO / NO_2 ratio diurnal cycle is very similar at both Beijing and Xianghe with a maximum in the early morning (values up to 0.08) and subsequent decreases to values ranging between 0.01 and 0.02 around local noon.

The production of OH radicals from HONO and O_3 has been estimated from observed HONO near-surface concentrations and calculated photolysis rates. At both stations, HONO is found to be the main contributor to OH production in the 0–200 m layer, except in summer around local noon where the contribution of O_3 dominates. The diurnal cycle of the OH production from HONO exhibits a maximum in the morning between 07:00 and 11:00, depending on season, followed by a rapid decrease. This maximum is larger at Beijing than at Xianghe, especially in winter time where the OH production from HONO reaches ∼ 1.2 ppb h^{-1} and ∼ 0.7 ppb h^{-1}, respectively.

To conclude, MAX-DOAS is shown to be a useful technique for long-term monitoring HONO near-surface concentrations and vertical column amounts in polluted areas. Multi-year data sets of HONO observations, such presented in this work, offer a better quantitative characterisation of HONO photochemistry and can provide additional constraints to modelling studies. For example, the diurnal and seasonal profiles of the HONO / NO_2 ratio derived in this study could be used in atmospheric models to constrain the rate of heterogeneous conversion of NO_2 to HONO, in order

to investigate the possible effects of this HONO source on the budget of oxidants.

Acknowledgements. This research was financially supported at IASB-BIRA by the Belgian Federal Science Policy Office, Brussels (PRODEX contract A3C and AGACC-II project), the EU 7th Framework Programme projects NORS (contract 284421) and SHIVA (contract 226224), and the ESA CEOS Intercalibration project (ESA/ESRIN Contract 22202/09/I-EC). We also acknowledge M. Bauwens (BIRA-IASB) for her technical support as well as R. McLaren (York University; Editor of this paper) and two anonymous referees for their helpful comments.

Edited by: R. McLaren

References

Brion, J., Chakir, A., Charbonnier, J., Daumont, D., Parisse, C., and Malicet, J.: Absorption Spectra Measurements for the Ozone Molecule in the 350–830 nm Region, J. Atmos. Chem., 30, 291–299, doi:10.1023/A:1006036924364, 2004.

Brinksma, E. J., Pinardi, G., Volten, H., Braak, R., Richter, A., Schönhardt, A., Van Roozendael, M., Fayt, C., Hermans, C., Dirksen, R. J., Vlemmix, T., Berkhout, A. J. C., Swart, D. P. J., Oetjen, H., Wittrock, F., Wagner, T., Ibrahim, O. W., de Leeuw, G., Moerman, M., Curier, R. L., Celarier, E. A., Cede, A., Knap, W. H., Veefkind, J. P., Eskes, H. J., Allaart, M., Rothe, R., Piters, A. J. M., and Levelt, P. F.: The 2005 and 2006 DANDELIONS NO_2 and aerosol intercomparison campaigns, J. Geophys. Res., 113, D16S46, doi:10.1029/2007JD008808, 2008.

Burrows, J. P., Richter, A., Dehn, A., Deters, B., Himmelmann, S., Voigt, S., and Orphal, J.: Atmospheric Remote-sensing reference data from GOME - 2.Temperature-dependent absorption cross-sections of O_3 in the 231–794 nm range, J. Quant. Spectrosc. Radiat. Transfer, 61, 509–517, 1999.

Chou, C. C.-K., Tsai, C.-Y., Chang, C.-C., Lin, P.-H., Liu, S. C., and Zhu, T.: Photochemical production of ozone in Beijing during the 2008 Olympic Games, Atmos. Chem. Phys., 11, 9825–9837, doi:10.5194/acp-11-9825-2011, 2011.

Clémer, K., Van Roozendael, M., Fayt, C., Hendrick, F., Hermans, C., Pinardi, G., Spurr, R., Wang, P., and De Mazière, M.: Multiple wavelength retrieval of tropospheric aerosol optical properties from MAXDOAS measurements in Beijing, Atmos. Meas. Tech., 3, 863–878, doi:10.5194/amt-3-863-2010, 2010.

Elshorbany, Y. F., Steil, B., Brühl, C., and Lelieveld, J.: Impact of HONO on global atmospheric chemistry calculated with an empirical parameterization in the EMAC model, Atmos. Chem. Phys., 12, 9977–10000, doi:10.5194/acp-12-9977-2012, 2012.

Fleischmann, O. C., Hartmann, M., Burrows J. P., and Orphal, J.: New ultraviolet absorption cross-sections of BrO at atmospheric temperatures measured by time-windowing Fourier transform spectroscopy, J. Photochem. Photobiol. A, 168, 117–132 , 2004.

Friess, U., Monks, P. S., Remedios, J. J., Rozanov, A., Sinreich, R., Wagner, T., and Platt, U.: MAX-DOAS O_4 measurements: A new technique to derive information on atmospheric aerosols: 2. Modeling studies, J. Geophys. Res. 111, D14203, doi:10.1029/2005JD006618, 2006.

George, C., Strekowski, R. S., Kleffmann, J., Stemmler, K., and Ammann, M.: Photoenhanced uptake of gaseous NO_2 on solid organic compounds: a photochemical source of HONO?, Faraday Discuss., 130, 195–210, doi:10.1039/B417888M, 2005.

Grainger, J. and Ring, J.: Anomalous Fraunhofer line profiles, Nature, 193, 762, 1962.

Harder, J. W. and Brault, J. W.: Atmospheric measurements of water vapor in the 442-nm region, J. Geophys. Res., 102, 6245–6252, 1997.

Heland, J., Kleffmann, J., Kurtenbach, R., and Wiesen, P.: A new instrument to measure gaseous nitrous acid (HONO) in the atmosphere, Environ. Sci. Technol., 35, 3207–3212, 2001.

Hendrick, F., Barret, B., Van Roozendael, M., Boesch, H., Butz, A., De Mazière, M., Goutail, F., Hermans, C., Lambert, J.-C., Pfeilsticker, K., and Pommereau, J.-P.: Retrieval of nitrogen dioxide stratospheric profiles from ground-based zenith-sky UV-visible observations: validation of the technique through correlative comparisons, Atmos. Chem. Phys., 4, 2091–2106, doi:10.5194/acp-4-2091-2004, 2004.

Hermans, C., Vandaele, A. C., Fally, S., Carleer, M., Colin, R., Coquart, B., Jenouvrier, A., and Mérienne, M.-F.: Absorption cross-section of the collision-induced bands of oxygen from the UV to the NIR, in: Proceedings of the NATO Advanced Research Workshop, Weakly Interacting Molecular Pairs: Unconventional Absorbers of Radiation in the Atmosphere, Fontevraud, France, 24 April–2 May 2002, edited by: Camy-Peyret, C. and Vigasin, A. A., NATO Science Series IV Earth and Environmental Sciences, vol. 27, Kluwer Academic Publishers, Boston, 193–202, 2003.

Hönninger, G., von Friedeburg, C., and Platt, U.: Multi axis differential optical absorption spectroscopy (MAX-DOAS), Atmos. Chem. Phys., 4, 231–254, doi:10.5194/acp-4-231-2004, 2004.

Kanaya, Y., Cao, R., Akimoto, H., Fukuda, M., Komazaki, Y., Yokouchi, Y., Koike, M., Tanimoto, H., Takegawa, N., and Kondo, Y.: Urban photochemistry in central Tokyo: 1. Observed and modeled OH and HO_2 radical concentrations during the winter and summer of 2004, J. Geophys. Res., 112, D21312, doi:10.1029/2007jd008670, 2007.

Kleffmann, J., Heland, J., Kurtenbach, R., Lörzer, J., and Wiesen, P.: A new instrument (LOPAP) for the detection of nitrous acid (HONO), Environ. Sci. Pollut. R., 4, 48–54, 2002.

Kleffmann, J., Gavriloaiei, T., Hofzumahaus, A., Holland, F., Koppmann, R., Rupp, L., Schlosser, E., Siese, M., and Wahner, A.: Daytime formation of nitrous acid: A major source of OH radicals in a forest, Geophys. Res. Lett., 32, L05818, doi:10.1029/2005GL022524, 2005.

Li, Y., An, J., Min, M., Zhang, W., Wang, F., and Xie, P.: Impacts of HONO sources on the air quality in Beijing, Tianjin, and Hebei Province of China, Atmos. Environ., 45, 4735–4744, 2011.

Li, X., Brauers, T., Häseler, R., Bohn, B., Fuchs, H., Hofzumahaus, A., Holland, F., Lou, S., Lu, K. D., Rohrer, F., Hu, M., Zeng, L. M., Zhang, Y. H., Garland, R. M., Su, H., Nowak, A., Wiedensohler, A., Takegawa, N., Shao, M., and Wahner, A.: Exploring the atmospheric chemistry of nitrous acid (HONO) at a rural site in Southern China, Atmos. Chem. Phys., 12, 1497–1513, doi:10.5194/acp-12-1497-2012, 2012.

Lu, K. D., Hofzumahaus, A., Holland, F., Bohn, B., Brauers, T., Fuchs, H., Hu, M., Häseler, R., Kita, K., Kondo, Y., Li, X., Lou, S. R., Oebel, A., Shao, M., Zeng, L. M., Wahner, A., Zhu, T.,

Zhang, Y. H., and Rohrer, F.: Missing OH source in a suburban environment near Beijing: observed and modelled OH and HO_2 concentrations in summer 2006, Atmos. Chem. Phys., 13, 1057–1080, doi:10.5194/acp-13-1057-2013, 2013.

Ma, J. Z., Beirle, S., Jin, J. L., Shaiganfar, R., Yan, P., and Wagner, T.: Tropospheric NO_2 vertical column densities over Beijing: results of the first three years of ground-based MAX-DOAS measurements (2008–2011) and satellite validation, Atmos. Chem. Phys., 13, 1547–1567, doi:10.5194/acp-13-1547-2013, 2013.

Madronich, S. and Flocke, S.: The role of solar radiation in atmospheric chemistry, in: Handbook of Environmental Chemistry, edited by: Boule, P., Springer-Verlag, Heidelberg, 1–26, 1998.

Meller, R. and Moortgat, G. K.: Temperature dependence of the absorption cross sections of formaldehyde between 223 and 323K in the wavelength range 225–375 nm, J. Geophys. Res., 105, 7089–7101, 2000.

Perner, D. and Platt, U.: Detection of nitrous acid in the atmosphere by differential optical absorption, Geophys. Res. Lett., 6, 917–920, 1979.

Peters, E., Wittrock, F., Großmann, K., Frieß, U., Richter, A., and Burrows, J. P.: Formaldehyde and nitrogen dioxide over the remote western Pacific Ocean: SCIAMACHY and GOME-2 validation using ship-based MAX-DOAS observations, Atmos. Chem. Phys., 12, 11179–11197, doi:10.5194/acp-12-11179-2012, 2012.

Platt, U. and Stuz, J.: Differential Optical Absorption Spectroscopy (DOAS), Principles and Applications, ISBN 978-3-540-21193-8, Springer, Berlin-Heidelberg, 2008.

Qin, M., Xie, P., Su, H., Gu, J., Peng, F., Li, S., Zeng, L., Liu, J., Liu, W., and Zhang, Y.: An observational study of the HONO-NO_2 coupling at an urban site in Guangzhou City, South China, Atmos. Environ., 43, 5731–5742, doi:10.1016/j.atmosenv.2009.08.017, 2009.

Richter, A., Burrows, J. P., Nüss, H., Granier, C., and Niemeier, U.: Increase in tropospheric nitrogen dioxide over China observed from space, Nature, 437, 129–132, doi:10.1038/nature04092, 2005.

Rodgers, C. D.: Inverse Methods for Atmospheric Sounding, Theory and Practice. World Scientific Publishing, Singapore-NewJersey-London-Hong Kong, 2000.

Sörgel, M., Trebs, I., Serafimovich, A., Moravek, A., Held, A., and Zetzsch, C.: Simultaneous HONO measurements in and above a forest canopy: influence of turbulent exchange on mixing ratio differences, Atmos. Chem. Phys., 11, 841–855, doi:10.5194/acp-11-841-2011, 2011a.

Sörgel, M., Regelin, E., Bozem, H., Diesch, J.-M., Drewnick, F., Fischer, H., Harder, H., Held, A., Hosaynali-Beygi, Z., Martinez, M., and Zetzsch, C.: Quantification of the unknown HONO daytime source and its relation to NO_2, Atmos. Chem. Phys., 11, 10433–10447, doi:10.5194/acp-11-10433-2011, 2011b.

Spurr, R., LIDORT and VLIDORT: Linearized pseudo-spherical scalar and vector discrete ordinate radiative transfer models for use in remote sensing retrieval problems, Light Scattering Reviews, Volume 3, edited by: Kokhanovsky, A., Springer, 2008.

Stavrakou, T., Müller, J.-F., Boersma, K. F., van der A, R. J., Kurokawa, J., Ohara, T., and Zhang, Q.: Key chemical NO_x sink uncertainties and how they influence top-down emissions of nitrogen oxides, Atmos. Chem. Phys., 13, 9057–9082, doi:10.5194/acp-13-9057-2013, 2013.

Stemmler, K., Ammann, M., Donders, C., Kleffmann, J., and George, C.: Photosensitized reduction of nitrogen dioxide on humic acid as a source of nitrous acid, Nature, 440, 195–198, doi:10.1038/nature04603, 2006.

Stutz, J., Kim, E. S., Platt, U., Bruno, P., Perrino, C., and Febo, A.: UV-vis Absorption Cross-Section of Nitrous Acid, J. Geophys. Res., 105, 14585–14592, 2000.

Stutz, J., Alicke, B., and Neftel, A.: Nitrous acid formation in the urban atmosphere: Gradient measurements of NO_2 and HONO over grass in Milan, Italy, J. Geophys. Res., 107, 8192, doi:10.1029/2001JD000390, 2002.

Su, H., Cheng, Y., Oswald, R., Behrendt, T., Trebs, I., Meixner, F. X., Andreae, M. O., Cheng, P., Zhang, Y., and Pöschl, U., Soil nitrite as a source of atmospheric HONO and OH radicals, Science, 333, 1616, doi:10.1126/science.1207687, 2011.

Vandaele, A. C., Hermans, C., Simon, P. C., Carleer, M., Colin, R., Fally, S., Mérienne, M.-F., Jenouvrier, A., and Coquart, B.: Measurements of the NO_2 absorption cross section from 42000 cm^{-1} to 10000 cm^{-1} (238–1000 nm) at 220 K and 294 K, J. Quant. Spectrosc. Radiat. Transfer, 59, 171–184, 1998.

Villena, G., Kleffmann, J., Kurtenbach, R., Wiesen, P., Lissi, E., Rubio, M., Croxatto, G., and Rappenglück, B.: Vertical gradients of HONO, NO_x and O_3 in Santiago de Chile, Atmos. Environ., 45, 3867–3873, doi:10.1016/j.atmosenv.2011.01.073, 2011.

Vlemmix, T., Piters, A. J. M., Berkhout, A. J. C., Gast, L. F. L., Wang, P., and Levelt, P. F.: Ability of the MAX-DOAS method to derive profile information for NO_2: can the boundary layer and free troposphere be separated?, Atmos. Meas. Tech., 4, 2659–2684, doi:10.5194/amt-4-2659-2011, 2011.

Wagner T., Dix, B., von Friedeburg, C., Friess, U., Sanghavi, S., Sinreich, R., and Platt, U.: MAX-DOAS O_4 measurements: A new technique to derive information on atmospheric aerosols – Principles and information content, J. Geophys. Res. 109, D22205, doi:10.1029/2004JD004904, 2004.

Wagner, T., Deutschmann, T., and Platt, U.: Determination of aerosol properties from MAX-DOAS observations of the Ring effect, Atmos. Meas. Tech., 2, 495–512, doi:10.5194/amt-2-495-2009, 2009.

Wittrock, F., Oetjen, H., Richter, A., Fietkau, S., Medeke, T., Rozanov, A., and Burrows, J. P.: MAX-DOAS measurements of atmospheric trace gases in Ny-Ålesund – Radiative transfer studies and their application, Atmos. Chem. Phys., 4, 955–966, doi:10.5194/acp-4-955-2004, 2004.

Wang, S., Ackermann, R., and Stutz, J.: Vertical profiles of O_3 and NO_x chemistry in the polluted nocturnal boundary layer in Phoenix, AZ: I. Field observations by long-path DOAS, Atmos. Chem. Phys., 6, 2671–2693, doi:10.5194/acp-6-2671-2006, 2006.

Wong, K. W., Tsai, C., Lefer, B., Haman, C., Grossberg, N., Brune, W. H., Ren, X., Luke, W., and Stutz, J.: Daytime HONO vertical gradients during SHARP 2009 in Houston, TX, Atmos. Chem. Phys., 12, 635–652, doi:10.5194/acp-12-635-2012, 2012.

Wojtal, P., Halla, J. D., and McLaren, R.: Pseudo steady states of HONO measured in the nocturnal marine boundary layer: a conceptual model for HONO formation on aqueous surfaces, Atmos. Chem. Phys., 11, 3243–3261, doi:10.5194/acp-11-3243-2011, 2011.

Wu, Q. Z., Wang, Z. F., Gbaguidi, A., Gao, C., Li, L. N., and Wang, W.: A numerical study of contributions to air pollution in Bei-

jing during CAREBeijing-2006, Atmos. Chem. Phys., 11, 5997–6011, doi:10.5194/acp-11-5997-2011, 2011.

Xia, X., Zong, X., and Sun, Li: Exceptionally active agricultural fire season in mid-eastern China in June 2012 and its impact on atmospheric environment, J. Geophys. Res. Atmos., 118, 9889–9900, doi:10.1002/jgrd.50770, 2013.

Young, C. J., Washenfelder, R. A., Roberts, J. M., Mielke, L. H., Osthoff, H. D., Tsai, C., Pikelnaya, O., Stutz, J., Veres, P. R., Cochran, A. K., VandenBoer, T. C., Flynn, J., Grossberg, N., Haman, C. L., Lefer, B., Stark, H., Graus, M., de Grouw, J., Gilman, J. B., Kuster, W. C., and Brown, S. S.: Vertically resolved measurements of nighttime radical reservoirs in Los Angeles and their contribution to the urban radical budget, Environ. Sci. Technol., 46, 10965–10973, doi:10.1021/es302206a, 2012.

Yu, X., Zhu, B., and Zhang, M.: Seasonal variability of aerosol optical properties over Beijing, Atmos. Environ., 43, 4095–4101, 2009a.

Yu, Y., Galle, B., Panday, A., Hodson, E., Prinn, R., and Wang, S.: Observations of high rates of NO_2-HONO conversion in the nocturnal atmospheric boundary layer in Kathmandu, Nepal, Atmos. Chem. Phys., 9, 6401–6415, doi:10.5194/acp-9-6401-2009, 2009b.

Zhang, Q., Streets, D. G., He, K., Wang, Y., Richter, A., Burrows, J. P., Uno, I., Jang, C. J., Chen, D., Yao, Z., and Lei, Y.: NO_x emission trends for China, 1995-2004: The view from the ground and the view from space, J. Geophys. Res., 112, D22306, doi:10.1029/2007JD008684, 2007.

Zhou, X., Gao, H., He, Y., Huang, G., Bertman, S. B., Civerolo, K., and Schwab, J.: Nitric acid photolysis on surfaces in low-NO_x environments: significant atmospheric implications, Geophys. Res. Lett., 30, 2217, doi:10.1029/2003gl018620, 2003.

Supplement to:

Observed and simulated time evolution of HCl, $ClONO_2$, and HF total column abundances

Atmos. Chem. Phys., 2012

by R. Kohlhepp et al.

15 March 2012

Table 1: Overview of the measurement specifications for HCl.

Measurement site	Spectral resolution [cm^{-1}]	Spectral microwindows [cm^{-1}]	Retrieved interfering species	Source of p/T profiles	Retrieval code	Spectroscopic database	Reference
Eureka DA8 (1997-2006)	0.004	2925.70-2926.10	NO_2	radiosondes, NCEP, US Sub-Arctic Winter Model	SFIT1.09e	HITRAN 1992 plus updates	Fast et al. (2011)
Eureka 125HR (2006-2009)	0.0035	2775.72-2775.80 2821.40-2821.62 2925.75-2926.05	O_3, CH_4, N_2O; HDO, N_2O; CH_4, NO_2, OCS, O_3	radiosondes, NCEP, US St. Atm.	SFIT2 v3.92C	HITRAN 2004 plus updates	Batchelor et al. (2009)
Ny Ålesund	0.005	2925.65-2926.25	CH_4	NCEP	GFIT	updated ATMOS linelist from GFIT package, v2.6.4	Notholt et al. (1995b)
Thule	0.0035	2727.60-2727.95 2775.60-2775.95 2925.70-2926.10	O_3, CH_4, HDO	NCEP	SFIT2 v3.93	HITRAN 2004 plus updates to 2007	Hannigan et al. (2009)
Kiruna	0.005	2727.73-2727.82 2775.73-2775.79 2819.52-2819.61 2821.52-2821.62 2843.60-2843.65 2904.09-2904.14 2923.65-2923.78 2925.80-2926.00 2942.70-2942.75 2961.04-2961.09 2963.25-2963.32 2995.76-2995.79	H_2O, O_3, CH_4	NCEP	PROFFIT	HITRAN 2004	Blumenstock et al. (2006)
Poker Flat	0.0035	2925.80-2926.00	H_2O, CH_4, NO_2, O_3	radiosondes, UKMO, CIRA86	SFIT2 v3.7	HITRAN 2004	Kagawa et al. (2007)
Harestua		2925.60-2926.20 2925.75-2926.00	H_2O, CH_4, NO_2, HCl, O_3	NCEP	SFIT2 v3.81	HITRAN 2004	
Zugspitze	0.005	2925.74-2926.06	CH_4	Munich radiosonde	SFIT1.09e	HITRAN 1996	Sussmann and Schäfer (1997)
Jungfraujoch	0.003	2925.74-2926.06	CH_4, NO_2	NCEP	SFIT1.09c	HITRAN 1992	Rinsland et al. (2003)
Toronto	0.004	2925.80-2926.00	CH_4, NO_2, O_3	NCEP, US St. Atm.	SFIT2 v3.82B3	HITRAN 2004	Wiacek et al. (2007)
Tsukuba	0.0035	2925.69-2926.21	CH_4, H_2O	radiosondes at Tateno	SFIT1.09e	HITRAN 1996	Murata et al. (2005)
Izaña	0.0036	same as Kiruna	H_2O, O_3, CH_4	local radiosondes	PROFFIT	HITRAN 2004	Schneider et al. (2005)
Mauna Loa	0.0035	2925.69-2926.50	CH_4	radiosondes at Hilo	SFIT1	HITRAN 2000	Hannigan et al. (2009)
La Réunion	0.00513 and 0.00893	2925.70-2926.10	CH_4	NCEP	SFIT2 v3.9	HITRAN 2004 plus updates for H_2O, N_2O, HNO_3, C_2H_6	Senten et al. (2008)
Wollongong	0.0035	2925.80-2926.00	CH_4	NCEP	GFIT	HITRAN 2004	Rinsland et al. (2003)
Lauder	0.0035	2925.75-2926.05	CH_4, NO_2, H_2O, O_3	NCEP/ NCAR	SFIT2 v3.82B3	HITRAN 2000	Rinsland et al. (2003)
Arrival Heights	0.0035	2925.75-2926.05	CH_4, NO_2, H_2O, O_3	NCEP/ NCAR	SFIT2 v3.82B3	HITRAN 2000	Mahieu et al. (2008)

Table 2: Overview of the measurement specifications for $ClONO_2$.

Measurement site	Spectral resolution [cm^{-1}]	Spectral microwindows [cm^{-1}]	Retrieved interfering species	Source of p/T profiles	Retrieval code	Spectroscopic database	Reference
Eureka DA8 (1997-2006)	0.004	779.550-781.100	O_3, H_2O, CO_2, C_2H_2	radiosondes, NCEP, US Sub-Arctic Winter Model	SFIT1.09e	HITRAN 1992 plus updates	Fast et al. (2011)
Eureka 125HR (2006-2009)	0.0035	779.850-780.450 782.550-782.870 938.300-939.300	CO_2, O_3, HNO_3; O_3, CO_2, H_2O, HNO_3; CO_2	radiosondes, NCEP, US St. Atm.	SFIT2 v3.92C	HITRAN 2004 plus updates	Batchelor et al. (2009)
Ny Ålesund	0.005	778.640-782.800	O_3, CO_2, H_2O, C_2H_2	NCEP	GFIT	updated ATMOS-linelist from GFIT package, v2.6.4	Notholt et al. (1995b)
Thule	0.01	780.120-780.320 780.700-781.250	O_3, CO_2	NCEP	SFIT2 v3.93	HITRAN 2004 plus updates to 2007	Hannigan et al. (2009)
Kiruna	0.005	779.000-779.800 780.000-780.300 780.300-781.300	H_2O, CO_2, O_3, HNO_3, C_2H_2	NCEP	PROFFIT	HITRAN 2004	Blumenstock et al. (2006)
Harestua		779.500-780.700 779.905-780.340	CO_2, H_2O, O_3, $ClONO_2$, HNO_3	NCEP	SFIT2 v3.81	HITRAN 2004	
Zugspitze	0.0036	779.300-780.600 780.050-780.355	H_2O, O_3, CO_2	Munich radiosonde	SFIT2 v3.8	HITRAN 1996 with Birk parameters for $ClONO_2$	Sussmann and Schäfer (1997)
Jungfraujoch	0.005	779.300-780.600 780.050-780.355	Wide: H_2O, O_3, CO_2; Narrow: O_3, HNO_3, COF_2	NCEP	SFIT2 v3.81	HITRAN 1996 including Birk and Wagner line parameters	Rinsland et al. (2003)
Izaña	0.0036	779.000-779.800 780.000-780.300 780.300-781.300	H_2O, CO_2, O_3, HNO_3, C_2H_2	local radiosondes	PROFFIT	HITRAN 2004	Schneider et al. (2005)
Wollongong	0.0035	779.300-780.600 780.050-780.355	Wide: O_3, H_2O, CO_2, C_2H_2; Narrow: none	NCEP	SFIT2 v3.92	HITRAN 2004	Rinsland et al. (2003)
Lauder	0.0035	779.300-780.600 780.050-780.355	Wide: O_3, H_2O, CO_2, C_2H_2; Narrow: none	NCEP/ NCAR	SFIT2 v3.82B3	HITRAN 2000	Rinsland et al. (2003)
Arrival Heights	0.0035	779.300-780.600 780.050-780.355	Wide: O_3, H_2O, CO_2, C_2H_2; Narrow: none	NCEP/ NCAR	SFIT2 v3.82B3	HITRAN 2000	Rinsland et al. (2003)

Table 3: Overview of the measurement specifications for HF.

Measurement site	Spectral resolution [cm^{-1}]	Spectral microwindows [cm^{-1}]	Retrieved interfering species	Source of p/T profiles	Retrieval code	Spectroscopic database	Reference
Eureka DA8 (1997-2006)	0.004	4038.780-4039.100	H_2O	radiosondes, NCEP, US Sub-Arctic Winter Model	SFIT1.09e	HITRAN 1992 plus updates	Fast et al. (2011)
Eureka 125HR (2006-2009)	0.0035	4038.780-4039.100	H_2O, HDO, CH_4	radiosondes, NCEP, US St. Atm.	SFIT2 v3.92C	HITRAN 2004 plus updates	Batchelor et al. (2009)
Ny Ålesund	0.005	4038.600-4039.240	H_2O	NCEP	GFIT	updated ATMOS-linelist from GFIT package, v2.6.4	Notholt et al. (1995a)
Thule	0.0035	4000.800-4001.200 4038.750-4039.200	H_2O, CH_4, HDO	NCEP	SFIT2 v3.93	HITRAN 2004 plus updates to 2007	Hannigan et al. (2009)
Kiruna	0.0075	4000.900-4001.050 4038.850-4039.080	H_2O	NCEP	PROFFIT	HITRAN 2004	Blumenstock et al. (2006)
Poker Flat	0.0035	4038.804-4039.148	H_2O	radiosondes, UKMO, CIRA86	SFIT2 v3.7	HITRAN 2004	Kagawa et al. (2007)
Harestua		4038.100-4039.500 4038.860-4039.050	H_2O, HDO, CH_4, HF	NCEP	SFIT2 v3.81	HITRAN 2004	
Zugspitze	0.0078	4038.800-4039.100	H_2O column	Munich Radiosonde	SFIT1.09e	HITRAN 1996	Sussmann and Schäfer (1997)
Jungfraujoch	0.004	4038.800-4039.105	CH_4, NO_2	NCEP	SFIT1.09c	HITRAN 1992	Zander et al. (2008)
Toronto	0.004	4038.770-4039.130	H_2O, HDO, CH_4	NCEP, US St. Atm.	SFIT2 v3.82B3	HITRAN 2004	Wiacek et al. (2007)
Tsukuba	0.0035	4038.800-4039.100	H_2O, HDO, CH_4	radiosonde	SFIT1.09e	HITRAN 1996	Murata et al. (2005)
Izaña	0.0036	4000.900-4001.050 4038.850-4039.080	H_2O	local radiosondes	PROFFIT	HITRAN 2004	Schneider et al. (2005)
Mauna Loa	0.0035	4038.850-4039.050	H_2O	radiosondes at Hilo	SFIT1	HITRAN 2000	Hannigan et al. (2009)
La Réunion	0.0072	4038.700-4039.050	H_2O	NCEP	SFIT2 v3.9	HITRAN 2004 updates for H_2O, N_2O, HNO_3, C_2H_6	Senten et al. (2008)
Wollongong	0.0035	4038.810-4039.090	H_2O	NCEP	GFIT	HITRAN 2004	Mahieu et al. (2008)
Lauder	0.0035	4038.780-4039.0995	H_2O, HDO, CH_4	NCEP/ NCAR	SFIT2 v3.82B3	HITRAN 2000	Reisinger et al. (1994)
Arrival Heights	0.0035	4038.780-4039.100	H_2O, HDO, CH_4	NCEP/ NCAR	SFIT2 v3.82B3	HITRAN 2000	Reisinger et al. (1994)